

Electronic Thesis and Dissertation Repository

November 2013

Joint Use of On-board Reconfigurable Antenna Pattern and Adaptive Coding and Modulation in Satellite Communications at High Frequency Bands

Marco Luccini
The University of Western Ontario

Supervisor
Prof. S. Primak
The University of Western Ontario

Graduate Program in Electrical and Computer Engineering
A thesis submitted in partial fulfillment of the requirements for the degree in Doctor of Philosophy
© Marco Luccini 2013

Follow this and additional works at: <https://ir.lib.uwo.ca/etd>



Part of the [Systems and Communications Commons](#), and the [Systems Engineering and Multidisciplinary Design Optimization Commons](#)

Recommended Citation

Luccini, Marco, "Joint Use of On-board Reconfigurable Antenna Pattern and Adaptive Coding and Modulation in Satellite Communications at High Frequency Bands" (2013). *Electronic Thesis and Dissertation Repository*. 1699.
<https://ir.lib.uwo.ca/etd/1699>

This Dissertation/Thesis is brought to you for free and open access by Scholarship@Western. It has been accepted for inclusion in Electronic Thesis and Dissertation Repository by an authorized administrator of Scholarship@Western. For more information, please contact wlsadmin@uwo.ca.

Joint Use of On-board Reconfigurable
Antenna Pattern and Adaptive Coding and
Modulation in Satellite Communications at
High Frequency Bands

(Thesis format: Monograph)

by

Marco Luccini

Graduate Program
in
Engineering
Electrical and Computer Engineering

A thesis submitted in partial fulfillment
of the requirements for the degree of
Doctor of Philosophy

School of Graduate and Postdoctoral Studies
The University of Western Ontario
London, Ontario, Canada

© Luccini 2013

Abstract

The Telecommunication market is driven by the increasing need of the end users for multimedia services which require high data rates. Within the fixed satellite service, frequency bandwidths wide enough to carry such high data rates are to be found in Ka band (26 – 40 GHz), and Q/V bands (40 – 50 GHz). However, at Ka band and above, transmitted signals can be severely affected by tropospheric attenuation for substantial percentages of time, resulting in the degradation of the quality and of the availability of communication services. Fade Mitigation Techniques (FMTs) must be used to counteract these severe propagation impairments.

In this thesis we explore the joint use of two of the most promising techniques, known as Reconfigurable Antenna and Adaptive Coding and Modulation, which up to now has been separately developed. Some of our accomplishments include, but are not limited to: a methodology to describe rain attenuation conditions for multiple users in large geographical areas, a tractable framework for the generation of correlated time series of rain attenuation for multiple receiving stations, the comparison of performance between fixed antenna systems and Reconfigurable Antenna system coupled with Adaptive Coding and Modulation.

Keywords: Satellite Communications, Fade Mitigation Techniques, Reconfigurable Antenna, Adaptive Coding and Modulation, Rain Attenuation Modelling, Attenuation Measurements

Acknowledgements

There have been many many people, both professors and friends, who helped me throughout the journey of my Ph.D. Without them, this thesis would not have been possible and these few lines want to express my gratitude to them.

Firstly, I would like to thank my supervisors Prof. Carlo Capsoni and Prof. Serguei Primak for their guidance during these years. Your advice has always been helpful and inspiring to take a new step ahead. It was a pleasure for me to work with you. I am also grateful to Prof. Aldo Paraboni, who invited me to start the Ph.D. career. His curiosity, kindness and attention were fundamental for my first steps in the world of research.

I would like to thank Prof. Nikolai Nefedov for accepting to be the reviewer of this thesis and for his valuable comments to improve this work.

I am grateful to my colleagues in the Propagation group at PoliMi: Prof. Carlo Riva, Laura, Lorenzo and Roberto. I enjoyed the time spent together and your help in the development of this thesis was fundamental.

During my stay at Western University I met very special people. I thank the folks in TEB 344, especially Elena, Oscar, Dan Dechene and Dan Wallace for their company and friendship. My gratitude goes also to Vittorio and Marta, Elena, Pietro Pirani and his family for their wonderful support.

My largest gratitude goes to my family and friends“Frecce Gialle” for their company to the bigger journey of my life.

I thank the Ph.D. School at Politecnico di Milano and the School of Graduate and Post-doctoral Studies at Western University for their support to the Double-Ph.D. Program. My recognition to Nadia, Sandra and Chris, part of the secretary staff at PoliMi and Western. I thank the italian Ministry of Education, University and Research (MIUR), Fondazione Cariplo, Politecnico di Milano and the Natural Sciences and Engineering Research Council of Canada (NSERC) for their financial support.

Table of Contents

Abstract	i
Acknowledgements	ii
Table of Contents	iii
List of Tables	vi
List of Figures	vii
List of Acronyms	xiv
1 Introduction	1
1.1 Motivations	1
1.2 Outline	5
1.3 Contributions	6
1.3.1 Contributions of Chapter 2	6
1.3.2 Contributions of Chapter 3	6
1.3.3 Contributions of Chapter 4	7
1.3.4 Contributions of Chapter 5	7
2 Atmospheric attenuation: propagation effects and attenuation modelling	9
2.1 Introduction	9
2.2 Structure of the atmosphere	10
2.3 Atmospheric attenuation components	13
2.3.1 Gaseous Absorption	13
2.3.2 Absorption and scattering by hydrometeors	17
2.3.3 Atmospheric Scintillation	23
2.4 Statistical description of attenuation	24
2.4.1 Gaseous attenuation	25
2.4.2 Cloud attenuation	26
2.4.3 Rain attenuation	28
2.4.4 Comparison of rain attenuation models	33
2.4.5 Combination of propagation effects	38
2.5 Conclusions	40

3	Generating correlated time series of rain attenuation for multiple sites	43
3.1	Introduction	43
3.2	The TS model: map	45
3.3	Overview of recent developments in the research topic	46
3.4	The proposed approach to multisite modelling	50
3.5	Database of data	52
3.6	Model and Algorithm description	53
3.6.1	Rain parameters definition	55
3.6.2	Rain state variable assigning process (conditioning process)	57
3.6.3	Rain time series assigning process (conditioned process)	67
3.7	Numerical simulations	70
3.7.1	Rain attenuation statistics: adaptability to different geographical sites	71
3.7.2	Site Diversity results	74
3.7.3	Rain decorrelation: Statistical Dependence Index χ	78
3.7.4	Fade duration statistics	83
3.8	Conclusions	87
4	Fade Mitigation Techniques	90
4.1	Introduction to Fade Mitigation Techniques for satellite transmissions	90
4.2	Review of most important Fade Mitigation Techniques	91
4.2.1	Site Diversity	92
4.2.2	Power Control	94
4.2.3	Other FMTs	95
4.3	The On-Board Dynamic Power Allocation System (Reconfigurable Antenna)	96
4.3.1	The service area model	98
4.3.2	Antenna design	99
4.3.3	Antenna Optimization	103
4.4	Adaptive Coding and Modulation for Multibeam satellite systems	112
4.4.1	Adaptive Physical layer model	114
4.5	Conclusions	118

5	Joint use of On-board Dynamic Power Allocation and ACM . . .	119
5.1	Introduction	119
5.2	TLC antenna system and optimization algorithm	120
5.2.1	Antenna optimization	124
5.3	Free-space considerations	124
5.4	Simulation setup	128
5.4.1	User's rain conditions simulation	132
5.5	Simulation methodology	134
5.6	Simulation results	136
5.6.1	Test case 1: Wide stratiform rain	136
5.6.2	Test case 2: Multiple convective cells	152
5.7	Conclusions	162
6	Conclusions	167
	References	172
	Appendices	
A	On the Correlation Characteristics of Binary Random Processes .	180
A.1	Introduction	180
A.2	Second-moment function of a clipped process and the Normal Surface	183
A.3	Orthogonal expansion of probability densities: the Edgeworth series .	186
A.3.1	The Edgeworth Series	186
A.3.2	Rodrigues formula and Hermite polynomials	187
A.4	Hard thresholding problem	188
A.5	Numerical Simulations	190
A.6	Application to the rain model problem - Pre-filtering example	198
A.7	Other Interesting Applications	200
A.8	Conclusions	201
	Curriculum Vitae	203

List of Tables

3.1	Estimated β values from different experiments in North-western Europe [1]	65
3.2	Estimated β values from Spino d'Adda beacon measurements	66
3.3	List of the DBSG3 considered experiments	86
3.4	Fade Durations Test Results	87
4.1	FMTs applicable to the forward-link of Multimedia Fixed SatCom scenario	96
4.2	Table of ModCod, Spectral Efficiency (SE) and SNIR threshold according to the DVB-S2 standard. The SNIR thresholds are defined targeting a system packet error rate equal to 10^{-7}	117
5.1	OBDPA system and simulation parameters	125
5.2	ModCod, SE and required SNIR according to the DVB-S2 standard. Required SNIR is targeting a quasi-error free transmission goal of 10^{-7} packet error rate	137

List of Figures

2.1	<i>K</i> , α coefficients as function of frequency [GHz]. Comparison among current Recommendation ITU-R P.838-3 and other distributions Joss (Thunder, green line crossed) and Gamma (μ parameter ± 3).	22
2.2	Principal planes in a medium composed by anisotropic particles . . .	23
2.3	CCDFs of slant path gaseous (oxygen and water vapour) attenuation at 20 (black), 40 (blue), 50 (light blue), 70 (green), 80 (red) and 90 (magenta) GHz for the site of Spino d’Adda, Italy (lat. 45.4° N, lon. 9.5° E, alt. 84 m a.s.l.) along a 37.7° slant path. Prediction according to ITU-R Rec. P.676-9	26
2.4	CCDFs of slant path clouds attenuation at 20 (black), 40 (blue), 50 (light blue), 70 (green), 80 (red) and 90 (magenta) GHz for the site of Spino d’Adda, Italy (lat. 45.4° N, lon. 9.5° E, alt. 84 m a.s.l.) along a 37.7° slant path. Prediction according to ITU-R Rec. P.840-5 . . .	27
2.5	Specific rain attenuation (dB/km) at 20 GHz (horizontal polarization) as function of rain rate (mm/h) for several DSD models	29
2.6	RMSE of SC-ExCell and SST models compared with reference model ITU-R P.618-10 and the average RMSE of the considered statistical models.	35
2.7	ME of SC-ExCell and SST models compared with reference model ITU-R P.618-10.	36
2.8	RMSE of SC-ExCell and SST models compared with reference model ITU-R P.618-10. Attenuation predicted from measured rain and compared with measured attenuation in DBSG3 database.	37
2.9	ME of SC-ExCell and SST models compared with reference model ITU-R P.618-10. Attenuation predicted from measured rain and compared with measured attenuation in DBSG3 database.	38
2.10	CCDFs of slant path rain attenuation at 20 (black curve), 40 (blue curve), 50 (light blue curve), 70 (green curve), 80 (red curve) and 90 (magenta curve) GHz for the site of Spino d’Adda, Italy (lat. 45.4° N, long. 9.5° E, alt. 84 m a.s.l.) along a 37.7° slant path (according to the SC-ExCell model)	39

3.1	Complementary Cumulative Distribution Function (CCDF) of rain attenuation for a satellite link at 39.6 GHz, elevation 37.7° at Spino d’Adda (Italy) as derived from the reference model SC-ExCell (blue solid line) and the Log-Normal approximation (green dashed line). The agreement of the Log-Normal model is high almost down to a probability of $2 \cdot 10^{-3}\%$, roughly equivalent to 10 minutes/year.	53
3.2	Spatial correlation of rain events obtained by the conditioning process compared with the desired reference correlation.	61
3.3	Representation of stations in the geographical area of interest. 500 stations are randomly placed in the area $250 \text{ km} \times 250 \text{ km}$ centred at Spino d’Adda. Red circles show the rainy stations at a single “epoch” as obtained by the rain assigning process (conditioning process). Note the well defined rainy area consequence of the spatial correlation imposed in the assigning process.	62
3.4	Spatial correlation of rain attenuation compared with the desired reference correlation. Example of 6 stations at different distances, 10 realizations.	70
3.5	Spatial correlation of rain attenuation: result of the Cholesky decomposition and Maximum Likelihood (ML) selection of series. Uncorrelated series (blue crosses) and correlated series after ML selection (green triangles).	71
3.6	Complementary Cumulative Distribution Function (CCDF) of rain attenuation at Spino d’Adda (Lat. 45.4 N , Lon. 9.5 E), Italy. Link at 20 GHz. Reference attenuation from physical model SC-ExCell (solid line) compared with time series of a single year realization and the average of multiple years. Higher stability at low probability values is achieved by averaging multiple years. A good stability down to probability of $10^{-2}\%$ is already obtained averaging 3 years, stability at $10^{-3}\%$ (6 min/year) is gained by averaging 5 to 10 single years. . . .	73
3.7	Complementary Cumulative Distribution Function (CCDF) of rain attenuation at Prague (Lat. 50.1 N , Lon. 14.3 E), Czech Republic. Link at 20 GHz. Reference attenuation from physical model SC-ExCell (solid line) compared with a single year realization and the average of multiple years time series. The selected series well reproduce the attenuation statistic also in this case by averaging a small number of year realizations. A good stability down to probability of $10^{-3}\%$ (6 min/year) is already obtained averaging 3 simulated years.	74

3.8	Complementary Cumulative Distribution Function (CCDF) of rain attenuation at Madrid (Lat. 40.4 N, Lon. 3.7 W), Spain. Link at 20 GHz. Reference attenuation from physical model SC-ExCell (solid line) compared with single year time series realization and the average of multiple years time series. In this case the station exhibits lower attenuation values in the statistical distribution. Also in this case, the curve is well represented by the selected “epochs” statistic. A good stability down to the probability of $10^{-3}\%$ (6 min/year) is obtained averaging 5 simulated years.	75
3.9	Dual-diversity results in Chibolton, U. K. Distance 6 km	76
3.10	Dual-diversity results in Toulouse, France. Distance 19 km	77
3.11	Dual-diversity results in Spino d’Adda, Italy. Distance 22 km	78
3.12	Dual-diversity results in Prague, Czech Republic. Distance 40 km	79
3.13	χ index obtained from the proposed model compared to the average χ index obtained by the NIMROD network. Simulation of 1 year (17520 epochs of 30 minutes, 910 rainy epochs), average of 10 different realizations. Two stations (circles and crosses) are selected as primary for the evaluation of the χ index to show the correct mutual correlation of rain events.	82
3.14	χ index obtained from the proposed model compared to the average χ index obtained by the NIMROD network. The χ index obtained from the conditioning process (red dots) is compared with the χ index resulting from the complete model (circles). The effect of the conditioned process, which imposes rain attenuation correlation, is evident for small distances (up to 50 km) where the impact of rain attenuation correlation is higher. It is also interesting the more accurate decorrelation achieved for large distances: the result of the two processes of the model better represent the expected rain decorrelation than the single conditioning process.	84
4.1	Coverage area over Europe: reference grid points and multibeam antenna scheme [2]	101
4.2	MPA general scheme	102
4.3	Antenna scheme. 1 feed per beam, MPA scheme 4×4 . The 4 feeds relative to red beams 32,34,7,9 in the service area are shown.	109
4.4	Representation of the dynamic optimization process	110
4.5	Climatological attenuation exceeded for 0.1% of annual time. Service area, model ITU-R P.618-10	111
4.6	Climatological attenuation exceeded for 0.2% of annual time. Service area, model ITU-R P.618-10	111
5.1	Service area Grid G6, satellite position $33^{\circ}E$. Pixels distribution (a) and beam division with frequency reuse scheme 4 (b) [2]	122

5.2	Power flux distribution in free-space conditions $\frac{\text{dBW}}{\text{m}^2}$ assuming uniform excitation coefficients.	126
5.3	Spatial SIR distribution in free-space conditions assuming uniform excitation coefficients.	127
5.4	Spatial SNR distribution in free-space conditions assuming uniform excitation coefficients.	128
5.5	Spatial SNIR distribution in free-space conditions assuming uniform excitation coefficients.	129
5.6	Snapshot 001228ss01: processed cumulated rain amount over the service area. Large stratiform rain area	130
5.7	Snapshot 000715ss01: processed cumulated rain amount over the service area. Multiple convective rain cells	131
5.8	Rain attenuation $P(A)$ relative to different snapshot of meteorological prediction information. The attenuation distribution gives the spatiotemporal information (coverage area) relative to the selected spot. Two different rainy conditions are described: wide stratiform rain (green curve), wide convective rain (red curve). For each $P(A)$, the circle-lines represent the approximation by the Log-normal distribution of rain attenuation needed for the TS model.	132
5.9	Grid of 500 users distributed in the spot n.32 region. Red users corresponds to the pixel grid of the Reconfigurable Antenna (RA) system .	133
5.10	Test case I: snapshot 001228ss01. Spatio/temporal evolution of the number of rainy stations during the 6-hours period. Blue crosses represents the simulated users in the area, red circles the fraction of users under rain at each hour. It is clearly visible the spatial feature of rainy states and its temporal evolution.	138
5.11	Test case I: snapshot 001228ss01. Rain attenuation distribution in space/time. Green line is the target distribution as derived from meteorological information for the 6 hour period, the red line is the simulated rain arranged in time series of 1 hour for all the rainy users. The starting point of the curve is the total fraction of users which experience rain attenuation	139
5.12	Average user SNIR values obtained for Fixed and OBDPA system . .	140
5.13	Average user SNIR gain of the OBDPA system. The OBDPA provides an average higher SNIR to almost all the simulated users	140
5.14	Test case I: snapshot 001228ss01. CDF of average SNIR users values in the simulated spot. The average SNIR per user is obtained over the 6-hours period. Fixed front end antenna (red) compared with OBPDA system (blue)	141

5.15	Test case I: snapshot 001228ss01. Scatter plot of channel capacity (right) and spectral efficiency (left). Fixed antenna (red) and OBDPA (blue). The blue crosses above the line defined by the red dots represent a gain in terms of channel capacity or SE.	143
5.16	Test case I: snapshot 001228ss01. Time evolution of SE for two selected users in the spot, subject to two separate rain fades. The extra margin provided by the OBDPA system results in a less severe degradation of users SE due to rain fades	144
5.17	Test case I: snapshot 001228ss01. Minimum value of SE for each users for fixed and OBDPA system (Left). Reduction of SE worst degradation:($SE_{OBDPA} - SE_{fixed}$) (right). Average $\Delta SE = 0.4$. . .	145
5.18	Test case I: snapshot 001228ss01. Average user throughput for CCM and ACM, with OBDPA (right) and fixed antenna (left)	146
5.19	Test case I: snapshot 001228ss01. User outage for high CCM, fixed fron-end compared to OBDPA antenna.	149
5.20	Test case I: snapshot 001228ss01. CCDF of user outage for high CCM and ACM, fixed antenna compared to OBDPA antenna.	149
5.21	Test case I: snapshot 001228ss01. Availability of modcod (percentage of time evaluated for all the users). Comparison between fixed antenna (red) and OBDPA antenna (blue)	150
5.22	Test case I: snapshot 001228ss01. Modcod histogram of overall usage (time evaluated for all the users). Comparison between fixed front end (red) and OBDPA antenna (blue)	151
5.23	Test case I: snapshot 001228ss01. Average user throughput gain using ACM coupled with OBDPA	151
5.24	Test case II: snapshot 000715ss01. Spatiotemporal evolution of the number of rainy stations during the 6-hours period	156
5.25	Test case I: snapshot 000715ss01. Rain attenuation distribution in space/time. Green line is the target distribution as derived from meteorological information for the 6 hour period, the red line is the simulated rain arranged in time series of 1 hour for all the rainy users. The starting point of the curve is the total fraction of users which experience rain attenuation	157
5.26	Test case II: snapshot 000715ss01. CCDF of average user SNIR for fixed antenna (red) and OBDPA system (blue). The average value is evaluated over the 6-hours time period	157
5.27	Test case II: snapshot 000715ss01. Scatter plot of user average channel capacity (right) and average SE (left) for fixed antenna (red dots) and OBDPA (blue crosses). The blue crosses above the line defined by the red dots represent a gain in terms of channel capacity or SE.	158

5.28	Test case II: snapshot 000715ss01. On the left: minimum value of user SE for the considered 6 hours period. Fixed antenna (red) compared with OBDPA system (blue). On the right, the SE gain $SE_{OBDPA} - SE_{fixed}$ in terms of minimum value. Average increase $\Delta SE = 0.35$. . .	159
5.29	Test case II: snapshot 000715ss01. Values of OBDPA antenna excitation coefficients across the whole service area	159
5.30	Test case II: snapshot 000715ss01. Average user throughput for CCM and ACM, with OBDPA (right) and with fixed antenna (right)	160
5.31	Test case II: snapshot 000715ss01. Distribution of user outage for CCM (blue) and ACM schemes (green). The effect of OBDPA is shown by the dotted lines	160
5.32	Test case II: snapshot 000715ss01. Histogram of modcod overall usage for fixed (red) and OBDPA system (blue)	161
5.33	Test case II: snapshot 000715ss01. Average user throughput gain using ACM coupled with OBDPA	162
A.1	Correlation of the random noise sequences and resulting correlation after clipping	182
A.2	Approximation of clipped process correlation (output) by Hermitian series expansion of order $N = 6$. Note the slow convergence at correlation values close to 1	192
A.3	Estimated Correlation at threshold 0	193
A.4	Output correlation of clipped process for three different thresholds: $0, \sigma, 2\sigma$	194
A.5	Convergence for different expansion order: $N = 6, 10, 20$	195
A.6	Percentage error of convergence for different expansion order: $N = 6, 10, 20$	196
A.7	Pre-filtering: solution obtained by inverting the Hermitian expansion of order $N = 20$ compared with analytical solution for the special case of $t_s = 0$	197
A.8	Pre-filtering: solution obtained by inverting the Hermitian expansion of order $N = 20$ for different clipping thresholds	198
A.9	Relationship between the desired correlation to be shown by the output binary sequences and the required correlation to be imposed to the input Gaussian random processes	199
A.10	Test case of rain model: resulting output correlation of binary sequences after hard thresholding	200

List of Acronyms

ACM	Adaptive Coding and Modulation
APL	Adaptive Physical Layer
BER	Bit Error Rate
BFN	Beam Forming Network
BSS	Broadcasting Satellite Service
CCDF	Complementary Cumulative Distribution Function
CDF	Cumulative Distribution Function
CCM	Constant Coding and Modulation
DRA	Data Rate Adaptation
DSD	Drop Size Distribution
ECMWF	European Centre of Medium-Range Weather Forecast
FER	Frame Error Rate
FMT	Fade Mitigation Technique
GEO	Geostationary Earth Orbit
GW	GateWay station
HDTV	High Definition Television
IMMBS	Interactive Multi Media Broadband Service
ITU	International Telecommunication Union
LEO	Low Earth Orbit

MPA	Multi Port Amplifier
ModCod	Modulation and Coding
OBDPA	On-Board Dynamic Power Allocation
OBRA	On-Board Reconfigurable Antenna
PBL	Planetary Boundary Layer
PDF	Probability Distribution Function
QoS	Quality of Service
RA	Reconfigurable Antenna
RRM	Radio Resource Management
RMSE	Root Mean Square Error
Rx	Receiving
SatCom	Satellite Communications
SE	Spectral Efficiency
SHF	Super High Frequency
SIR	Signal to Interference Ratio
SNIR	Signal to Noise plus Interference Ratio
SNR	Signal to Noise Ratio
TDM	Time Division Multiplexing
TDMA	Time Division Multiple Access
TLC	Telecommunication
TS	Time Series
Tx	Transmitting
UT	User Terminal

Chapter 1

Introduction

1.1 Motivations

Satellite and Terrestrial Telecommunication systems greatly benefit from the use of high frequencies (Super High Frequency (SHF) band and above in this thesis). The main advantage is the availability of larger bandwidths, required for the increasing demand of multimedia services. In addition, higher frequency bands require smaller antenna size for a fixed gain, or conversely, the higher antenna gain for a fixed size, which certainly represent concrete benefits. Moreover, the possibility of using on-board antennas with reconfigurable directivity is attractive for satellite systems whose coverage area is subdivided in spot beams for frequency reuse or regional services.

Frequencies up to the W band are envisaged for the future Earth to satellite links [3]. A clear statement of the interest in using the W band is the decision of the Federal Communications Commission of the U.S.A. “to promote non-Federal Government development and use of the ‘millimeter wave’ spectrum in the 71-76 GHz, 81-86 GHz and 92-95 GHz bands on a shared basis with Federal Government operations. These bands are available for use in a broad range of new products and services, including high-speed, point-to-point wireless local area networks and broadband Internet access. Highly directional, ‘pencil-beam’ transmissions can be engineered in close proximity to one another without causing interference”.

The drawback of radiowaves at frequencies above the Ka band (Q/V and W bands) is the consistent increase of the impairments caused by the lower part of the

atmosphere (troposphere). Consequently, research activities on tropospheric propagation up to 50 GHz were carried with many experimental and theoretical studies. Currently the research focus is moving above 50 GHz: some preliminary experiments have been carried out in the past few years [4, 5].

Due to the strong propagation impairments, the design of Telecommunication (TLC) systems at Ka band and above, particularly the satellite based systems, must rely on advanced techniques to counteract atmospheric fades. The classical approach of a fixed system margin would lead to unrealistic over-dimensioning on-board power level and receiving ground terminal front ends. It is therefore necessary to implement specific techniques to counteract these degrading effects. The extensive use of Fade Mitigation Techniques (FMTs), such as site diversity or on board adaptive power allocation, from the propagation point of view, Adaptive Coding and Modulation (ACM) and Data Rate Adaptation (DRA), from the information-theoretical point of view, is mandatory [2]. Some reduction in terms of Quality of Service (QoS) should also be accepted.

Two different classes of FMTs that can complement each other are envisaged in this thesis. On one side those techniques which take into account the spatial and temporal de-correlation of the atmospheric attenuation caused by meteorological phenomena, from the other side those based on the dynamic selection of the transmission modulation/coding pair ACM and/or on the data rate. The choice of the most appropriate technique and its implementation is based on the intensive use of propagation models, able to mimic the quality of the radio channel with sufficient accuracy.

In this respect, the models able to represent the spatial distribution of atmospheric attenuation over large (continental) areas and derived from the simple knowledge of basic meteorological information are of specific interest for both Broadcasting Satellite Service (BSS) and Interactive Multi Media Broadband Service (IMMBS)

scenarios. For these application scenarios, important models are those which are able to provide the attenuation time series experienced by different end-users spread over the service area. Useful models should simulate high resolution data in space and time based on available low resolution meteorological data. In addition, they should be able to reproduce with good accuracy first order and second order statistics (such as fade slope and fade duration) for multiple locations, including the correct spatial correlation of atmospheric attenuation.

This thesis addresses the problem of the joint use of two FMTs for fixed satellite communications: the on board reconfigurable antenna pattern coupled with ACM. The problem is analyzed in its entirety: we consider the use of reconfigurable antenna and ACM in conjunction of a developed model to simulate the propagation environment based on meteorological data.¹ To the best of our knowledge, this is the first attempt to take into account all these techniques together.

A complex satellite system, characterized by a reconfigurable antenna front-end, able to spatially arrange power distribution according to the actual time-variant propagation needs will be referred to On-Board Dynamic Power Allocation (OBDPA) system. In such system the power is allocated only in the amount that is needed to support required QoS, thereby allowing management of the limited on-board available resources. The antenna adaptation procedure relies on updated meteorological information, provided to the reconfiguration algorithm on a regular basis. On the other side, ACM is a sophisticated form of information rate control in which single user information rate is adapted by changing modulation type and coding rate, while maintaining a constant symbol rate. The aim of this technique is to dynamically select, based on the current channel quality, the transmission Modulation and Cod-

1. The focus here is on the rain effects which are the biggest contributors to signal attenuation.

ing (ModCod) pair which maximizes spectral efficiency satisfying the required Bit Error Rate (BER)/Frame Error Rate (FER) performance.

In order to test the joint use of the above techniques there is the need of a model which provides attenuation information at single user level with high resolution in time and space. The model should be able to reproduce correct statistics on the short and long-term basis. On the short basis, the simulated attenuation evolution should reproduce with the highest accuracy single rain events evolution (within 6-hours time interval), which is comparable to a communication session duration. Long term statistics represent sites specific meteorological conditions over time period of a few years. Moreover, the need of considering multiple users not co-located and subject to spatially correlated attenuation conditions appeared evident. In this thesis we developed a novel model for the generation of correlated time series of rain attenuation for multiple users in a large geographical area. As input information, this model uses a large database of rain attenuation measurements available [6]. The focus on rain attenuation is motivated by the consideration that it represents the most significant source of signal degradation of medium/high availability TLC systems above 10 GHz (Chapter 2). Furthermore, the model is trimmed and refined to reproduce the spatial rain attenuation information which are provided to the OBDPA system. Finally, the model is used in a case study evaluation of the performance of the OBDPA system with and without ACM. In this framework, the main objective of the study is to develop, validate and apply the channel model while evaluating overall system performance. The outcome of this study could potentially be applied to the following scenarios (among others):

- the design and analysis of the Satellite Communication System before its deployment, which requires the use of channel models and input data whose com-

putational complexity must be traded off with the accuracy they provide;

- the system operational stage, during which the model may be used to activate specific mitigation technique. In this case, requirements are in terms of real time or about real time application, of ability to identify the actual state of the radio channel and of the confidence interval of the performances.

1.2 Outline

This thesis is divided into the following Chapters.

Chapter 2 presents the atmospheric attenuation effects which have to be dealt with in radiowave propagation for and Earth-to-satellite communication links. The specific attenuation of the different atmospheric components is discussed, among with current statistical models to evaluate the attenuation contribution. Special attention is dedicated to rain attenuation modelling and accuracy of selected prediction models is evaluated.

In Chapter 3 we propose a novel methodology to obtain correlated time series of rain attenuation for multiple users, starting from a database of real measurements. Climatological parameters define the rain attenuation distribution, while a correlation model based on the user distances is included in assigning rain events occurrence and rain average attenuation. The model is tested both for single sites and joint sites statistical results, as well as on the first order and second order attenuation statistics.

Chapter 4 discusses the possible FMTs available for a Multimedia Fixed Satellite Communications (SatCom) scenario. Special attention is focused on the description of two techniques: the reconfigurable antenna system OBDPA and Adaptive Coding and Modulation ACM in satellite transmissions.

In Chapter 5, the application of the rain time series model to the OBDPA system is presented. Time series of rain attenuation are generated to evaluate, jointly with the OBDPA system simulation results, the Signal to Noise plus Interference Ratio (SNIR) evolution for each user in the coverage area. Once the SNIR time series are obtained, final results in terms of spectral efficiency and throughput are derived considering both the use of constant rate transmission (no feedback channel) and ACM transmissions.

Chapter 6 outlines the conclusions of the thesis work.

1.3 Contributions

The contributions of the thesis are as follows.

1.3.1 Contributions of Chapter 2

- (1) A complete survey presenting the modelling of atmospheric attenuation is thoroughly discussed;
- (2) Specifically concerning rain attenuation, the most accurate models to predict rain attenuation distribution are discussed and their accuracy assessed by comparison with reference statistical model ITU-R P.618-10 against a comprehensive database of measurements.

1.3.2 Contributions of Chapter 3

- (1) The overview of the most recent models to obtain time series of rain attenuation samples for multiple sites is presented;

- (2) The model proposed by the author is introduced and comprehensively discussed, with special attention to the methodology to impose the correct spatial correlation and temporal evolution of the time series for a large number of sites;
- (3) The model performances are assessed. Single site I order and II order attenuation statistics are presented against reference models, in terms of joint statistics of multiple sites the rain decorrelation index is presented.

1.3.3 Contributions of Chapter 4

- (1) The overview of the possible Fade Mitigation Techniques applicable to the Multimedia Fixed SatCom scenario is presented;
- (2) The OBDPA system and ACM for multibeam satellite systems are introduced and detailed;
- (3) The joint deployment of the two techniques is motivated to possibly improve the overall system performance

1.3.4 Contributions of Chapter 5

- (1) The proposed model of rain attenuation time series is applied to the simulation of two “on-demand” rain conditions according to the meteorological information used in the optimization of the OBDPA system;
- (2) Attenuation time series are simulated for a large number of users into one spot of the OBDPA system

-
- (3) The user SNIR and Spectral Efficiency (SE) are defined as proper figure of merit to assess the effects of OBDPA coupled with constant transmission schemes (CCM) and adaptive schemes ACM.
 - (4) Results in terms of users SNIR distribution, SE distribution, throughput and availability are generated for different transmission schemes. The advantage of the OBDPA coupled with ACM is investigated.

Chapter 2

Atmospheric attenuation: propagation effects and attenuation modelling

2.1 Introduction

Radiowave propagation plays an important part in the design and performance of space communications systems. The degrading effect of precipitation in the transmission path is a major concern associated with space communication systems, particularly for those operating above 10 GHz. At these frequencies, absorption and scattering caused by rain, hail, ice crystals, or wet snow can cause a reduction in transmitted signal amplitude (attenuation) which reduces the reliability and performance of the space communication link. Other effects can be generated by precipitation on the earth-space path. They include depolarization, rapid amplitude and phase fluctuations (scintillations), antenna gain degradation, and bandwidth coherence reduction.

Even apparent “clear sky” conditions can produce propagation effects which can degrade or change the transmitted radio wave. Constituent gases in the earth’s atmosphere, particularly oxygen and water vapor, interact with the radio wave and reduce the signal amplitude by an absorption process. Turbulence or rapid temperature variations in the transmission path can cause amplitude and phase scintillations or depolarize the wave. Clouds, fog, dirt, sand, and even severe air pollution can cause

observable propagation effects. Finally, background sky noise is always present and contributes directly to the noise performance of the communications receiver system.

The relative importance of the radio-wave propagation factors discussed above depends to a large extent on the frequency of operation of the earthspace link and the required system availability, as well as on the local climatology, local geography, type of transmission, and elevation angle to the satellite. Generally, the effects become more significant as the frequency increases and as the elevation angle decreases. The randomness and general unpredictability of the phenomena which produce the propagation effects adds a further dimension of complexity and uncertainty in the elevation of radio-wave propagation in space communications, and statistical approaches have been found to be most useful to evaluate many of the problem areas [7].

The next paragraphs focus on the description of the main propagation impairments for fixed satellite links and the current models to predict their impact in terms of signal attenuation. Sec. 2.2 describes the atmospheric medium, Sec. 2.3 presents the main atmospheric sources of propagation impairments: gaseous absorption, hydrometeors absorption and scattering and tropospheric scintillation are described. Sec. 2.4 presents a survey of the statistical models currently in use to predict the attenuation distribution of the different atmospheric components. In Sec. 2.5 the conclusions of this Chapter are reported.

2.2 Structure of the atmosphere

The atmosphere propagation medium can be modeled as a three-dimensional half space bounded by the Earth's surface, with pressure and density decreasing exponentially with altitude forced by gravity. The variation of atmospheric temperature with height, instead, exhibits a cycling pattern, caused by solar and Earth's radiation, and

the atmosphere is commonly divided into layers according to their thermal state. The vertical changes in temperature are important in constraining weather events to the lowermost region of the atmosphere.

The troposphere, from the Earth's surface to 11-12 km above, is characterized by decreasing temperature with respect to height, which is mainly a consequence of heating from the surface, so the closer the air is to the ground, the warmer it becomes. The rate of change of air temperature with height (lapse rate) is generally about 6.5° C per kilometer, but the actual lapse rate varies with location, season, time of day, weather conditions. The upper boundary of the troposphere is called tropopause. The height of the tropopause is very dependent on geographical latitude and season, being around 16 km height at the equator, and as low as 8 km at the poles. In the lowest 1-2.5 km of the troposphere, the Planetary Boundary Layer (PBL), the atmosphere is directly influenced by the Earth's surface and responds to surface influences with a timescale of an hour or less [8], causing heavy variances of meteorological parameters like temperature, wind and humidity.

The troposphere is followed by the stratosphere (from about 11-12 km to 50 km), where temperature increases due to strong absorption of solar ultraviolet radiation by the ozone layer, located near 25 km above the earth's surface. Because warmer air lies above cooler air in this region, there are few overturning air currents and, thus, the stratosphere is a region of little mixing. Together with the troposphere, they account for 99.9% of the Earth's atmosphere.

Between around 50 – 90 km altitude, in the so-called mesosphere, temperature decreases again, and this is the coldest region of the atmosphere. Finally, in the thermosphere, above 80- 90 km, temperature ranges up to 2000 K caused by absorption of energetic ultraviolet and X- ray radiation. The assumption of local thermodynamic equilibrium is not valid in the thermosphere. The ionosphere is the lower part of

the thermosphere, and extends from about 80 to 400 km in height. It is electrically charged as short wave solar radiation ionizes the gas molecules. The electrical structure of the ionosphere is not uniform, the thickness changing from night (weaken) to the day depending on solar radiation, and it is generally divided in a number of layers. A generalized model of the vertical structure of the atmosphere is given by the 1976 U. S. Standard Atmosphere [9]. It provides temperature, pressure and density profiles that represent average conditions in mid latitudes for altitudes between 5 km below sea level and 1000 km above sea level. Annual, seasonal and monthly averages of temperature, pressure and water-vapour pressure as a function of altitude are provided by ITU-R [10].

For the purposes of this study, the region of interest is the lower part of the atmosphere, because it contains the bulk of the total atmospheric mass and the meteorological phenomena, and therefore exercises the greatest influence, with the exception of the radio signal effects introduced by the ionosphere. Hence for computational purposes, only the lowermost 60 km of the atmosphere needs to be considered. Also, when horizontal variations are evaluated to occur on larger spatial scales than the considered geographical area, the atmosphere is customarily taken to be a horizontally homogeneous, slab medium.

Air is a mixture of several gaseous species. The standard mixture contains nitrogen (78%), oxygen (21%) and argon (1%), together accounting for about 99,96% of the dry air's volume. These gases are permanent, well-mixed species in the lowest 80 km, such that partial density and pressure of each species obey the exponential decrease with height that follows from the hydrostatic balance and the gas law (scale height typically of 6-9 km). This also applies to long-lived minor species like carbon dioxide, methane, nitrous oxide, and a number of inert gases. Concentrations of other species are variable in space and time, depending on their generation mechanisms.

The most important is water vapour. Water vapour is primarily found in the troposphere. In fact, nearly one half of total water vapour in the atmosphere is found between sea level and 1.5 km. Less than 5 – 6% of water vapour is found above 5 km and less than 1% is found in the stratosphere. Water vapour influences weather and climate in two ways: (1) it plays a fundamental role in Earth’s hydrological cycle, since the formation of clouds, fog, and precipitation depends on its condensation, and (2) it is the dominant greenhouse gas in the atmosphere. Water vapour has a large latent heat associated with its change of phase and represents a major source of energy for circulation systems associated with the weather and climate.

The influence of the atmosphere on electromagnetic waves in the microwave band is generally divided in the clear-air effects of atmospheric gases and their associated refractive index changes, like signal delay, ray bending, absorption, reflection and tropospheric scattering, and in the effects produced by liquid and solid particles (clouds, precipitation, aerosols), like attenuation, cross polarization and scattering. Modeling of these effects is the topic of the next sections.

2.3 Atmospheric attenuation components

2.3.1 Gaseous Absorption

Absorption of electromagnetic energy by the gases in the atmosphere results from the quantum physical behavior of atmospheric constituent molecules. The energy of a molecule is determined by the sum of its translational, rotational, vibrational and electric energy: $E = E_t + E_r + E_v + E_e$, with $E_r < E_t < E_v < E_e$. Except for translational energy, these energies are quantized and can only assume discrete

values. Allowed energy states are well defined and depend on the structure of the specific molecule.

At microwave frequencies, absorption by atmospheric gases is dominated by oxygen and water vapour. The absorption spectrum of water vapour at these frequencies is caused by rotational transitions induced by the interaction of the external field with the molecule's permanent electric dipole moment, with resonance lines at 22.235 GHz, 83.310 GHz, and several frequencies above 300 GHz. Oxygen produces a family of rotational lines due to transitions in the magnetic dipole spin-rotation around 60 GHz and an isolated line at 118.75 GHz. However, emission and absorption due to a single change of energy state is practically never monochromatic, but a spectral line is broadened over a certain frequency. This line broadening is caused by the finite natural lifetime of the energy state (natural broadening), collision between molecules (pressure or collision broadening), and the Doppler effect due to thermal motion of molecules in space (Doppler broadening). Natural broadening is negligible compared to the other broadening mechanisms, collision broadening is dominant below 20 km in altitude, while in the upper atmosphere Doppler broadening is dominant. The frequency dependence of the absorption has been found to depend on an empirical line width constant which is a function of temperature, pressure and the humidity of the atmosphere [11]. All of these parameters are highly variable with altitude, location, season of the year, and time of day.

Attenuation due to oxygen and water vapour in atmosphere is generally described by the specific attenuation in dB/km, which is calculated by the sum of contributions of each energy transitions of the two molecules. The total gaseous

attenuation A_a dB in atmosphere along the path r_0 km is given by:

$$A_a = \int_0^{r_0} \{\gamma_o(r) + \gamma_v(r)\} dr, \quad \text{dB} \quad (2.1)$$

where γ_o and γ_v are the specific attenuation of oxygen and water vapour in dB/km, respectively.

Zenith attenuation is evaluated by considering, in first approximation, an exponential decay of oxygen and water vapour concentration with altitude. An equivalent height in atmosphere is introduced to describe the path length of the radiowave in atmosphere. Consequently, Eq. 2.1 is simplified into:

$$A_a = \gamma_o h_o + \gamma_v h_v, \quad \text{dB} \quad (2.2)$$

The definition of h_o, h_v , out of the absorption band around 60 GHz, depends on the frequency and ground temperature.

For slant paths through the atmosphere, the attenuation is given by the cosecant of the elevation angle, down to about 6° of elevation angle, where the cosecant law breaks down because of earth curvature and refraction effects. Below 6° , the attenuation is obtained by ray tracing the path through the atmosphere starting at the surface height and obtaining the line integral of attenuation along the ray path. Above 6° of elevation, the equivalent path length can be derived by:

$$L = \frac{2h}{\sqrt{\sin^2(\theta) + 2h/R} + \sin(\theta)} \quad (2.3)$$

where θ represents the elevation angle and h the equivalent height of oxygen or water vapour.

The correct procedure for obtaining the gas attenuation consists in calculating the gaseous specific attenuation for each point of the path, for example by using the Microwave Propagation Model [12], which allows to evaluate with high accuracy the above attenuation contributions from vertical profiles of pressure, temperature and relative humidity.

In addition to physical models, which rely on the complete knowledge of the vertical profiles of the atmospheric parameters, other models have been developed [13, 14]. Such models are generally characterized by a simplified formulation and are based on surface or integrated meteorological parameter, much more readily available with respect to the vertical profiles. Those simplified methods are valid only in defined frequency intervals, such as the spectral transmission windows of the atmosphere, and are based on a-priori assumptions of the vertical profiles of the meteorological parameters (standard or typical atmospheres). The International Telecommunication Union (ITU) defined a statistical procedure to evaluate the attenuation due to oxygen and water vapour with sufficient accuracy in the most of the satellite transmission cases [13]. The yearly averaged gaseous attenuation at the zenith can be calculated, according to ITU-R Recommendation [13], by multiplying the approximated gaseous specific attenuation at ground level, which is a function of ground water vapour density, temperature and pressure, by its effective height, which depends only on frequency and pressure. The climatic input parameters of the models (the surface air temperature, the water vapour density and the total water vapour content), are now available in global maps from ITU-R (on a yearly basis) [15]

2.3.2 Absorption and scattering by hydrometeors

Hydrometeor is the general term referring to the products of condensed water vapour in the atmosphere, observed as rain, hail, ice, cloud, fog or snow. The presence of hydrometeors in the radio wave path, particularly rain, can produce major impairments to space communications, especially for frequencies higher than 10 GHz. Rain drops both absorb (attenuate) and scatter radio wave energy. Together with clouds and fog they have a significant impact in the design of terrestrial and space communication systems. Main effects account attenuation and depolarization of the received signal, their contribution is considerably higher than snow and hail.

2.3.2.1 Clouds and Fog

Although rain is the most significant hydrometeor affecting radiowave propagation, the influence of clouds, fog, hail, and snow can also be present on an earth-space path. Clouds and fog generally consist of water droplets of less than 0.1 mm in diameter, and this allows the Rayleigh approximation to be used in the calculation of the specific attenuation of clouds and fog up to about 100 GHz. With this approximation, cloud attenuation is found to be proportional to the liquid water content rather than the drop size distribution [7].

Clouds attenuation is highly variable, depending on their liquid water content. In the ITU-R model [16], the dependence of clouds specific attenuation on droplets temperature is taken into account by defining the liquid water content reduced to 0°C, that, integrated as a function of height, results in the reduced total liquid water content measured in ($\frac{\text{kg}}{\text{m}^2}$ or mm). Global statistics of this parameter have been calculated by using global data from European Centre of Medium-Range Weather Forecast (ECMWF) numerical analysis and are provided through global maps [16].

Cloud attenuation is then obtained as a function of the reduced liquid water content, the frequency, the elevation angle and the dielectric constant of the water. There is no particular frequency limitation up to 100 GHz as for specific attenuation due to liquid water.

From theoretical calculation and experimental measurements, it appears that cloud attenuation is equivalent to very light rainfall attenuation and, during rain which exceeds 10 mm/h, the rain attenuation will be the dominant factor in the total attenuation experienced on the path [7].

Concerning fog, it results from the condensation of atmospheric water vapour into suspended water droplets, with a typical density of $0.4 \frac{\text{g}}{\text{m}^3}$ with peaks at $1 \frac{\text{g}}{\text{m}^3}$. Fog layers seldom exceed 50 - 100 m in thickness, hence fog attenuation can usually be considered negligible for radio-wave communications on a slant path [7].

2.3.2.2 Rain Attenuation

The classic theory for rain attenuation assumes that the energy of the radio wave is subject to an exponential decay due to the rain fields. Rain droplets result in absorption and diffusion of the incident radio wave energy, with independent contributions which may be integrated [17].

The attenuation due to a rain volume L can be expressed by:

$$A = \int_0^L \gamma dx \quad [dB] \quad (2.4)$$

where γ is the specific attenuation of the rain volume, expressed in dB/km . Considering a plane wave with transmitted power density P_t , incident on a volume of uniformly distributed spherical water drops of radius a , extending over a length L ,

the received power P_r is given by:

$$P_r = P_t e^{-kL} \quad (2.5)$$

where k is the attenuation coefficient for the rain volume, expressed in km^{-1} . The attenuation will be:

$$A = 10 \log \frac{P_t}{P_r} = 4.343kL \quad \text{dB} \quad (2.6)$$

The attenuation coefficient k can be obtained as the product between the water droplets density per unit volume, ρ , and the attenuation cross-section of drops Q_t , equal to the ratio between the lost power density and the total incident power density:

$$k = \rho Q_t \quad (2.7)$$

Q_t is the sum of the cross-sections for absorption and diffusion, it is function of the drop radius r , the wavelength of the radio wave λ and the complex refractive index of the water drop m . Assuming $n(r)$ the probability density function of drops with radius r , k can be expressed as:

$$k = \int Q_t(r, \lambda, m) n(r) dr \quad (2.8)$$

$n(r)dr$ can be interpreted as the number of drops per unit volume with radii between r and $r + dr$. The specific attenuation γ is then derived from Eq. 2.6, with $L = 1$:

$$\gamma = 4.343 \int Q_t(r, \lambda, m) n(r) dr \quad \text{dB/km} \quad (2.9)$$

The above result emphasizes the dependence of rain attenuation on drop sizes, drop size distribution, rain rate and attenuation cross-section. The first three pa-

rameters are characteristics of the rain structure only, the attenuation cross-section introduces the dependence on the frequency and temperature. All the parameters exhibit time and spatial variability which are not deterministic, or directly predictable. Hence, most analyses of rain attenuation must resort to statistical means to evaluate the impact of rain on communication systems.

Q_t can be obtained by referring to the classical scattering theory of Mie for a plane wave radiation upon an absorbing sphere [18]: if the wavelength is considerably larger than the dimension of the drop ($2\pi r \ll \lambda$) the Rayleigh cross-section is

$$Q_t = \frac{8\pi^2}{\lambda} r^3 \text{Im} \left[\frac{m^2 - 1}{m^2 + 2} \right] \quad (2.10)$$

The drop size distribution, $n(r)$, depends on the rain rate and type of storm activity, it has been found to be well represented by an exponential function:

$$n(r) = N_0 e^{-\Lambda r} = N_0 e^{-[cR^{-d}]r} \quad (2.11)$$

where R is the rain rate in mm/h and r the drop radius in mm. N_0 , c , d are constants to be determined from measured distribution and describe different kinds of rain. The rain drop diameter is typically between 0.1 and 10 mm. Values of Λ and N_0 are reported in [19] for the model by Marshall-Palmer and in [20] for the Joss-Waldvogel model.

Given the distribution of drop diameters and the rain cross section description, the specific attenuation of rain is derived:

$$\gamma = 4.343 N_0 \int Q_t(r, \lambda, m) e^{-\Lambda r} dr \quad \text{dB/km} \quad (2.12)$$

obtaining the total rain attenuation for the path L by integration of Eq. 2.12 over

the extent of the rain volume. This integration procedure is not a straight task since Q_t and r distribution generally vary along L and these variabilities must be included in the calculation.

For this reason, the rain attenuation is predicted with a more direct relationship with the rain rate (also referred as rain intensity) at the earth surface. The rain specific attenuation is well approximated by the relation:

$$\gamma = aR^b \quad \text{dB/km} \quad (2.13)$$

where a and b are frequency and temperature dependent constants which approximate the complex behaviour of the complete representation given by Eq. 2.12, from which Eq. 2.13 can be directly inferred.

The use of Eq. 2.13 is applied in most of the present models to predict rain attenuation from rain rate, several sources of tabulation for the a and b parameters as function of frequency and temperature are available. Figure 2.1 shows the coefficients as function of frequency as derived from different models: Joss, Gamma distribution and Recommendation ITU-R P.838.3 [21].

2.3.2.3 Depolarization by rain and ice

If the use of dual polarization is foreseen, the depolarization (XPD) introduced by the non-spherical particles (drops and ice crystals) must be taken into account. In particular, the physical parameters that cause XPD are the anisotropy (i.e. the polarization-dependent forward scattering of the particles) and the angle of the symmetry axes of the particles with respect to the polarization plane (canting angle). In [22], it is shown that depolarization at a given frequency can be scaled to a different one by scaling the corresponding anisotropies. The hydrometeor axes however are

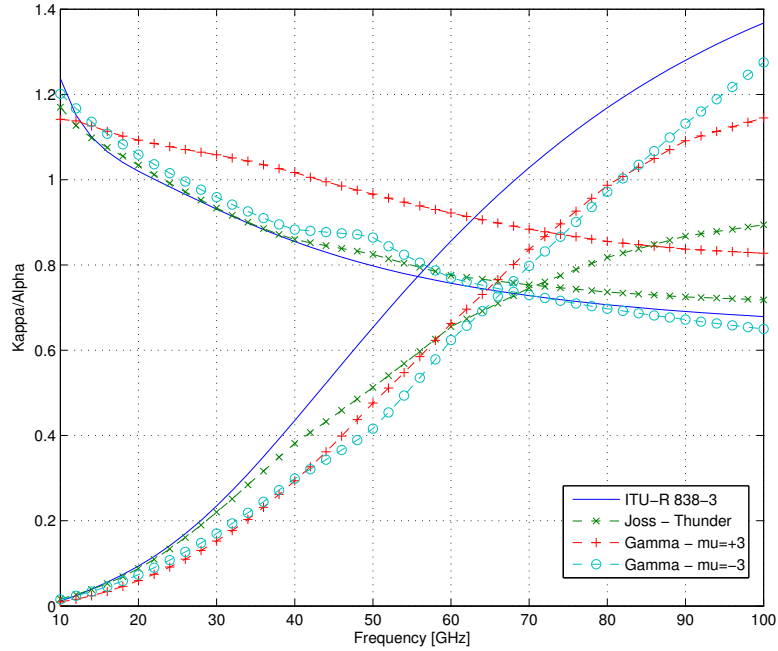


Figure 2.1: K, α coefficients as function of frequency [GHz]. Comparison among current Recommendation ITU-R P.838-3 and other distributions Joss (Thunder, green line crossed) and Gamma (μ parameter ± 3).

not equi-aligned and the dispersion of these orientations is, generally, beneficial (reduce) to XPD, although the phenomenon becomes much more complex and difficult to describe. A further difficulty is due to the co-presence of water and ice-particles along the path.

To a first approximation, we can simplify the formulation of the problem by assuming that all the hydrometeors have rotational symmetry and are equi-oriented. Two particular planes, named “principal planes” are then identified: the one determined by the common orientation of the hydrometeor axes and the propagation direction and the perpendicular one containing also the propagation direction (as shown in Fig. 2.2). When the electric field strength is parallel to one of these two planes, the wave propagates through the medium without being depolarized.

The dependence of the measured XPD in circular polarization on copolar attenuation (CPA) has been found experimentally at 50 GHz (Italsat experiment) to follow the linear relationship [23]:

$$\text{XPD} = 0.5 \cdot \text{CPA} - 33; \quad (2.14)$$

This simple model takes into account both rain and ice effects but it should be validated at higher frequencies. In fact, similarly to attenuation, also XPD worsens dramatically with the increase in frequency.

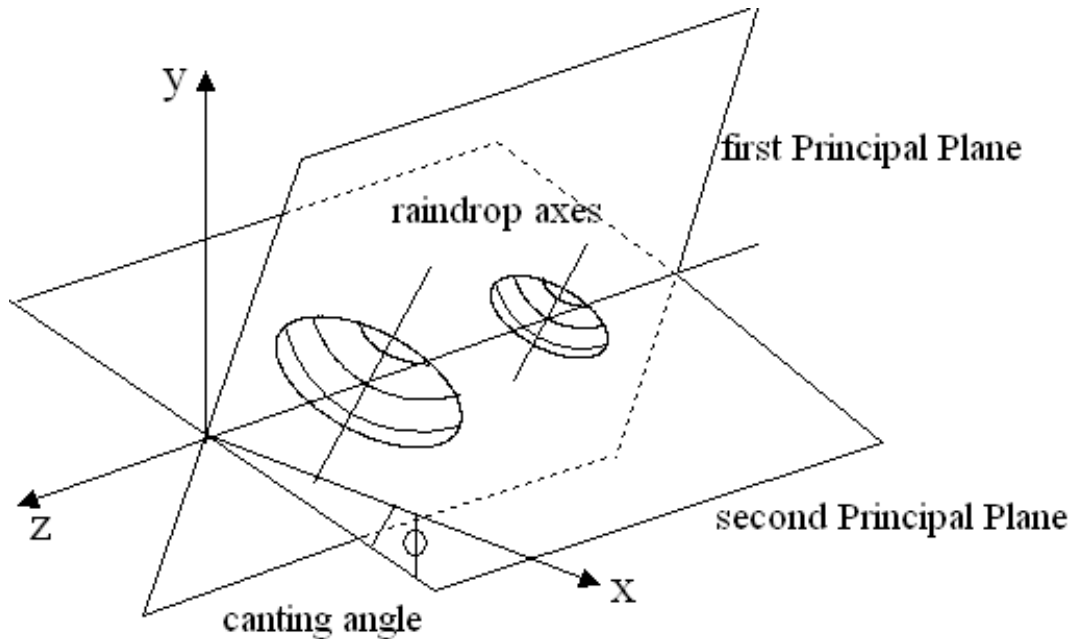


Figure 2.2: Principal planes in a medium composed by anisotropic particles

2.3.3 Atmospheric Scintillation

Tropospheric scintillation is due to small-scale refractive index non-homogeneities induced by atmospheric turbulence along the propagation path. As a result, rapid

fluctuations of the received signal amplitude affect satellite links above about 10 GHz.

The intensity of tropospheric scintillation is usually quantified in terms of the signal standard deviation calculated during a stationary period of few minutes, which depends on the turbulence structure index, increases with the frequency and with the path length and decreases when the antenna size increases because of aperture averaging. Scintillation can be due also to the variation of the arrival angle of the main ray which increases when the beam width decreases due to the effect of the antenna radiation pattern. The present model recommended by ITU-R [24] is applicable up to a frequency of at least 20 GHz but it has been noticed [25] that it is not in very good agreement with measurements at various sites at Ka and Q/V bands (up to 50 GHz), possibly due to the variation of the angle of arrival of the main signal which likely play a role for highly directive antennas (as in the case of very high frequencies). The relative impact of angle-of-arrival fluctuations on measured scintillations requires further study.

Scintillation can also occur inside rain and, in this case they are mixed with the fast fluctuations induced by rain itself. A model based on a theoretical approach, using Tatarskii's theory [26] of scintillation in clear sky, has been proposed and tested for different sites and frequency up to V band [27]. Scintillation, apart from their impact on the performance of communications systems (especially those with low-margin) [28], may interfere with tracking systems or Fade Mitigation Techniques.

2.4 Statistical description of attenuation

Statistical models for attenuation components are required because of the complexity of physical models, which often are related to local observation and, for example,

require radiosonde observations (RAOBS) to obtain vertical profiles of atmospheric constituents.

In this Section, the current statistical models for predicting the total atmospheric attenuation are introduced. Examples of attenuation distribution for the different components are presented for a test Earth-satellite link, for a range of frequencies between 20 and 90 GHz. A very simple evaluation of the required system margin to achieve a certain system availability is obtained.

Due to the importance of rain attenuation in the total attenuation definition, a deeper analysis about rain attenuation models is presented. The analysis presents the most important aspects of rain attenuation modelling and includes the assessment of the attenuation prediction error of selected models.

2.4.1 Gaseous attenuation

An effective alternative to the calculation of the path attenuation due to gases is offered by models currently adopted in the ITU-R Recommendation P.676-9 [13]. Such model introduce simplified (yet accurate) formulations relying on effective parameters which embed information on the vertical profiles of water vapour and oxygen concentrations. Specifically, the mean yearly distribution of total zenith attenuation due to oxygen can be calculated by multiplying the oxygen specific attenuation at ground level by an effective height, which, in turn, is a function of frequency and pressure. As for water vapour, recommendation ITU-R P.676-9 includes the calculation of the total zenith attenuation in reference conditions at 20.6 GHz as a function of the water vapour total content (global maps of this parameter are available in [29], to be afterwards multiplied by a frequency scaling factor. As a final step, the slant path attenuation due to oxygen or water vapour, is obtained by scaling the zenith attenu-

ation through the cosecant law, under the plausible assumption of local homogeneity of the atmosphere.

Fig. 2.3 shows the ITU-R predicted Complementary Cumulative Distribution Functions (CCDFs) of gaseous (oxygen and water vapour) attenuation in Ka band (20 GHz), Q/V band (40 and 50 GHz) and W band (70, 80 and 90 GHz) for Spino d'Adda, along a 37.7° slant path (to a GEO satellite at 13°E). At 1% of the yearly time (system availability of 99%) the fade margin is about 1 dB in Ka and Q bands and between 2.5 and 4 dB in the V and W bands.

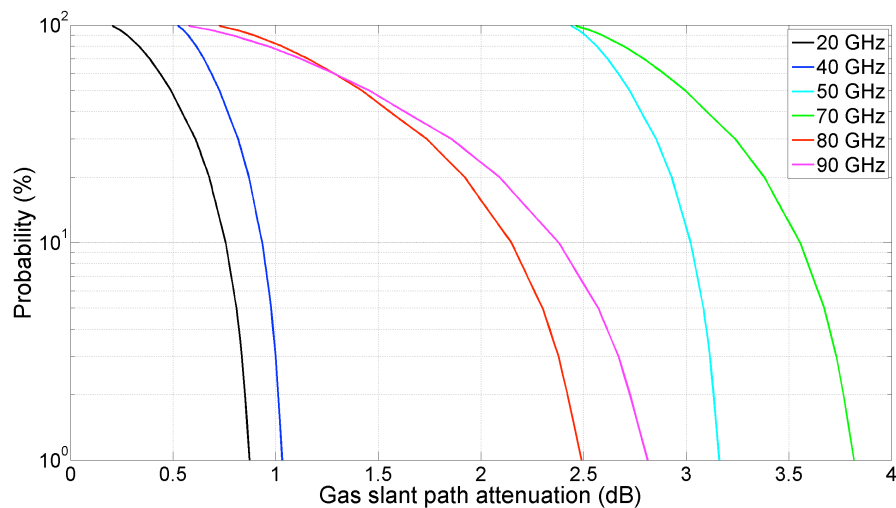


Figure 2.3: CCDFs of slant path gaseous (oxygen and water vapour) attenuation at 20 (black), 40 (blue), 50 (light blue), 70 (green), 80 (red) and 90 (magenta) GHz for the site of Spino d'Adda, Italy (lat. 45.4° N, lon. 9.5° E, alt. 84 m a.s.l.) along a 37.7° slant path. Prediction according to ITU-R Rec. P.676-9

2.4.2 Cloud attenuation

As for gases, simplified models have been proposed by the ITU-R to estimate on a global basis the CCDFs of the attenuation due to clouds. Specifically, in Recommendation P.840-5 [16], the dependence of cloud specific attenuation on droplets

temperature is taken into account by defining the liquid water content reduced to 0°C . This latter parameter depends on the frequency and its statistics are calculated by ITU-R in the 20-50 GHz frequency band (but can be recalculated in different frequency bands) and distributed through global maps. The cloud attenuation is then obtained as a function of the reduced liquid water total content, the water permittivity, the frequency and the elevation angle. Fig. 2.4 depicts the ITU-R predicted CCDFs of cloud attenuation in the Ka band (20 GHz), the Q/V band (40 and 50 GHz) and the W band (70, 80 and 90 GHz) for the site of Spino d'Adda along a 37.7° slant path. At 1% of the time (system availability of 99%), the fade margin is about 0.4 dB in Ka band, rising in the range between 4 and 6 dB for frequencies in W band.

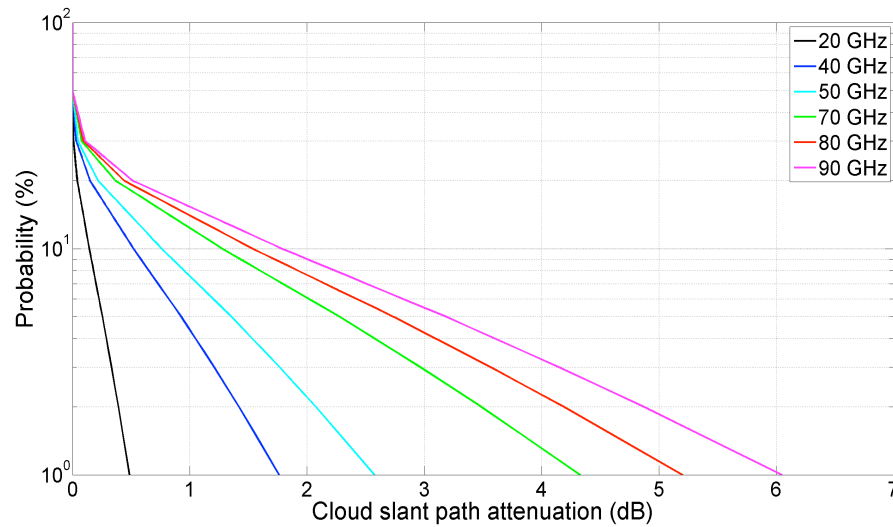


Figure 2.4: CCDFs of slant path clouds attenuation at 20 (black), 40 (blue), 50 (light blue), 70 (green), 80 (red) and 90 (magenta) GHz for the site of Spino d'Adda, Italy (lat. 45.4° N, lon. 9.5° E, alt. 84 m a.s.l.) along a 37.7° slant path. Prediction according to ITU-R Rec. P.840-5

2.4.3 Rain attenuation

Attenuation due to rain is the most relevant propagation effect relevant to the design of satellite telecommunication systems. All available methods of attenuation prediction attempt to relate the Cumulative Distribution Function (CDF) of attenuation along a slant path to the cdf of ground rainfall intensity. To this purpose a set of assumptions are however necessary; among them, those with stronger impact are:

- the relationship between specific attenuation and rainfall intensity;
- the model describing the rainfall rate CDF;
- the vertical and horizontal profiles of rainfall intensity.

The several methods available today in the literature [30] substantially differ from one to another mainly for the different hypotheses made about the above assumptions. These issues become more and more important increasing the frequency, owing to the magnifying effect of these parameters on all the phenomena related to rain.

2.4.3.1 Relationship between specific attenuation and rainfall intensity

As described in Sec. 2.3.2.2, most of the models refers to the relation in Eq. 2.13 to derive the specific rain attenuation from the value of rain intensity R in mm/h.

In 2.13, k and α are coefficients which depend on the frequency, elevation angle, drop temperature and drop size distribution Drop Size Distribution (DSD). Indeed, non marginal differences in the specific rain attenuation may come from the variation of the DSD that occurs from event to event and, sometimes, also during the same event. As an example, Fig. 2.5 shows the relationship between rain intensity and specific attenuation at 20 GHz: each curve in the figure represents a different DSD

model. The current ITU-R Recommendation [21] is compared to other distributions in order to show the DSD effect on rain specific attenuation. At 20 GHz there is a weak dependence on the rain intensity, which is instead more pronounced at higher frequency bands [3]. There is instead a significant difference among the considered models: at 10 mm/h the peak to peak relative variation in the specific attenuation is about 40%.

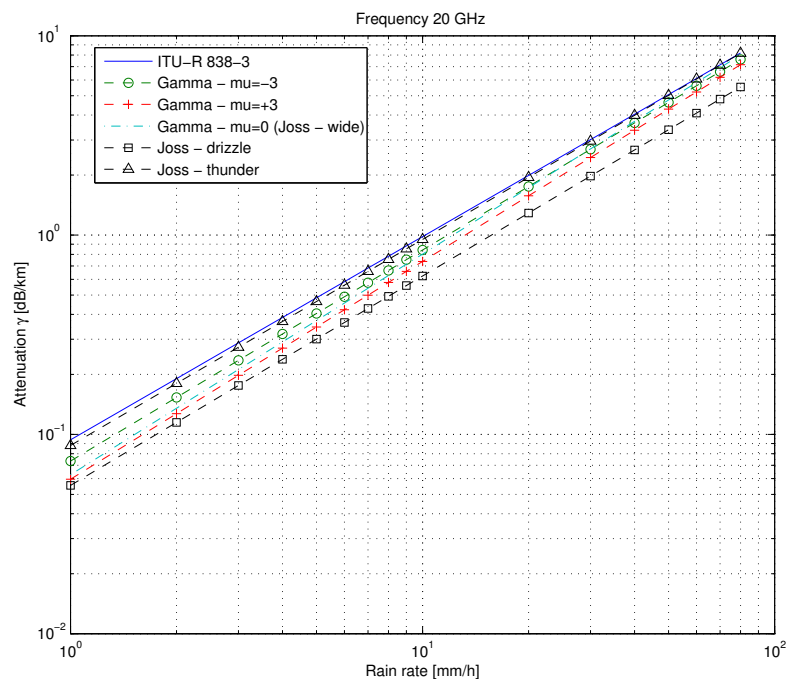


Figure 2.5: Specific rain attenuation (dB/km) at 20 GHz (horizontal polarization) as function of rain rate (mm/h) for several DSD models

2.4.3.2 Rainfall rate prediction models

The main input of rain attenuation prediction models is the rainfall CDF, whose values, tightly linked to the local climatology, have a directly impact on the predicted attenuation statistics. The International Telecommunication Union ITU recommends

the use of rainfall rate CDFs with 1-minute integration time in order to properly estimate also extreme fade values. The 1-minute integration time is not the standard time interval used in meteorological applications, for which there is no interest in rapid changes of rain intensity, but rather in reliable average quantities (half-hourly, hourly, daily, monthly or yearly cumulated rain). Therefore, rain gauge data routinely collected for meteorological purposes and covering long observation periods are easily available worldwide, whilst specialized measurements for propagation applications are carried out on spot basis at specific sites (usually associated to other experimental activities on electromagnetic propagation).

This fact has driven research efforts towards the development of procedures aimed at deriving rain rate CDFs with 1-minute time resolution from the knowledge of rain rate CDFs with much longer integration time or from the knowledge of general meteorological conditions.

The rainfall rate prediction model currently recommended by the ITU-R [31] is a meteorology based method and relies on global long-term meteorological maps. Specifically, the method estimates the 1-minute integrated rainfall rate CDF worldwide from the simple knowledge of the site's geographical coordinates and receives as input the mean yearly local amounts of the convective and stratiform rain (M_c and M_s , respectively), together with the 6-hour rainy probability ($Pr6$). All this information is extracted from the ERA-40 database, provided by the ECMWF.

In general, the CCDF of rain attenuation is directly related to the local rain rate CCDF, which is highly variable from site to site.

2.4.3.3 Vertical and horizontal profiles of rainfall intensity

As far as the rain profile is concerned, the issue covers two different, but related, aspects: the vertical and the horizontal profile. The first one is peculiar of the slant-

path links and is related to the estimation of the rain height, of the bright-band effects and, to a minor extent, of the polarisation mismatching induced by the ice-clouds, particularly important at low elevation angle.

The attempts to solve the problem of rain profile have often led to the definition of ‘effective’ rain heights. A significant refinement of the rain height modelling for the estimation of the rain induced attenuation has been afterwards introduced in [32], in which the authors have proposed a method to derive two different stratiform and convective rain heights by properly taking into account the monthly mean values of the 0°C isotherm heights (conditioned to the presence of rain) and the associated monthly mean values of the convective-over-total rain amount ratio. In fact, stratiform events are typically associated with a lower vertical extent with respect to convective ones, in which rain drops are pushed well beyond the 0°C isotherm height by the strong updrafts and downdrafts. In addition, stratiform precipitations are usually coupled with a definite melting layer (the layer just below the 0°C isotherm height where the falling snowflakes and ice particles melt into water drops), whose effect, in terms of signal attenuation, can be taken in due account through the introduction of an “equivalent rain height” to be added to the stratiform rain height.

Also the modelling of the horizontal profile has originated a lot of different proposals during the past decades. Several analytical profile have been proposed in order to adequately model the rainfall spatial distribution within a single cell, among which the exponential [32] (SC-ExCell model) and the hybrid Gaussian-exponential [33] (HYCELL) ones are worth being cited. Among the various proposals, the ExCell and the HYCELL models also include methodologies that allow to derive of the correct rain cells’ probability of occurrence from the knowledge of the local rainfall rate CDF and, as a result, they permit the statistical estimation of the attenuation induced on a radio link by the synthetic rain cells.

2.4.3.4 Rain attenuation models

The prediction of rain attenuation CDF starting from the rainfall intensity CDF has been the subject of a big effort carried out by many researchers in the last three decades. Several methods have been developed and their performance evaluated using statistics from propagation experiments at frequencies up to 50 GHz. The difference between the performances of the various methods is often negligible and their errors are of the order of the year-to-year variability of precipitation (around 20 – 30%).

SC-ExCell [32], ITU-R Rec. P.618-10 [24], SST [34] are methods that appear to be the best according to the most recent testing activity [35]. The above mentioned models, especially the physically based ones, can be probably applied up to 90 GHz without significant performance degradation even if the accuracy assessment is not possible due to lack of data above 50 GHz. The tested frequency range extends from 1 to 50 GHz. Their application to links with elevation angle down to 5 degrees should not present any problem, since the spatial structure of precipitation is taken into account in the models; a comparison with low elevation beacon measurements would assess possible performance degradation.

Among the effects to be specifically taken into account in the design of medium/low availability systems, the melting layer, typically present during stratiform events (low rain fades), is of key importance at frequencies above 50 GHz. The melting layer can be modeled as a slab, with typical thickness around 600 m, around the altitude of the 0° C isotherm curve. This layer shows peculiar attenuation characteristic due to the transition of water molecules from ice to rain. The melting layer contribution to rain attenuation can be described as a function of the rain intensity underneath and of the transmission frequency, for this reason its contribution is normally included in rain attenuation models. The calculations for the attenuation contribution could be car-

ried out with an anisotropic model of the transition layer, which considers a medium consisting of absorbing and scattering hydrometeors like ice, melting ice and rain drops [36]. The model requires as input the initial density of the melting particles, the frequency, the DSD and the rain intensity below the melting layer.

2.4.4 Comparison of rain attenuation models

Attenuation due to rain is the main drawback to the propagation at frequencies above 10 GHz because the hydrometeor dimensions become comparable with the wavelength of the incident wave.

In order to address the rain attenuation modelling for in the present study, the performances of selected models are assessed against a reference database of measurements. The model performances are described by the following figure of merit:

$$\varepsilon(p) = \frac{A_p(p) - A_m(p)}{A_m(p)} \cdot 100 \quad (2.15)$$

where $A_p(p)$ is the predicted attenuation at probability p , $A_m(p)$ the measured (or reference) attenuation at the same probability. The mean percentage error and Root Mean Square Error (RMSE) were evaluated for the selected models. Special emphasis is given to the SC-ExCell prediction method [32] and the two layer SST [34] because of their very good overall performance. The first method describes the meteorological environment as an ensemble of synthetic isolated rain cells with the inner spatial distribution of rain intensity that follows an exponential behaviour and takes separately into account the contribution to attenuation due to stratiform and to convective rain. Moreover, the contribution due to the melting layer is added only to stratiform rain as an equivalent rain slab whose height depends markedly of frequency. The model has been successfully tested in [35] up to the frequency of 50 GHz. In the two layer

SST method, rain is modelled as two layers of precipitation of different depth: the layer closer to ground whose height is latitude dependent according to ITU-R rules is filled by rain, while the second one, 400 m in depth, is filled by melting hydrometeors and equivalently represented by a rain rate value 3.134 times higher than the rain intensity below. More details can be found in [34].

The two above mentioned models were tested against other statistical models, among which the Recommendation [24]. The database DBSG3 [37] provides the reference measured attenuation statistics: the part of the database relative to experiments at frequencies above 17 GHz was considered for this activity.

The attenuation prediction accuracy of the SC-ExCell happened to be improved in the framework of this activity when applying the ITU-R P.838-3 Recommendation [21] $\gamma - R$ relationship. It was found in fact that the above relation enhances the attenuation values at low intensity level and it is relatively close to the one proposed as Joss- thunderstorm and to the Gamma DSD with $\mu = -2$. This last DSD was found to be the most suitable one to account for the instantaneous frequency scaling at the Italsat frequencies [Private communication]. Accordingly, this made possible to modify the prediction model, by eliminating the awkward rain plateau. Final results in terms of attenuation prediction error show a good agreement with the reference results. The model accuracy has been verified according in the probability range from 0.01% to 5% (typical probability of rain attenuation in mid-latitude regions). Special attention was dedicated to the model accuracy at high probability values, corresponding to low rain rates.

In a first test, the rain rate distribution $P(R)$ is derived from the Recommendation ITU-R P.837-5 [31]. As it can be appreciated from Fig. 2.6, where the normalized RMSE is plotted as a function of the probability value in the range 0.01%~5%, the chosen models present similar performance with the ITU-R P.618-10 being this one

a bit better on the overall and in particular in the probability range 0.1% – 5%, that represents the most critical range correspondent to low rain rates and close to the probability of rain. However, it must be noticed that the ITU-R model has been validated and optimized on the attenuation measurements of the DBSG3 database. The comparison was made on the available experiments at frequencies between 17 and 50 GHz, considering all the possible elevation angles between 5° and 90° degrees and latitudes.

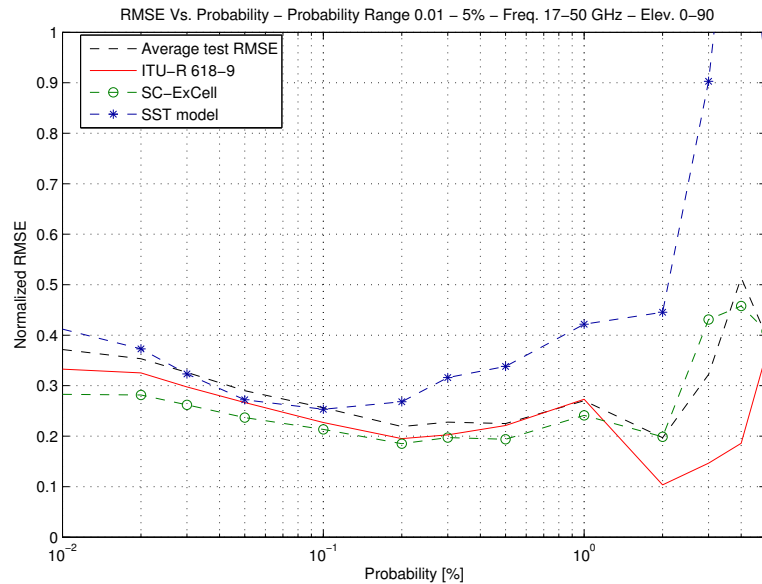


Figure 2.6: RMSE of SC-ExCell and SST models compared with reference model ITU-R P.618-10 and the average RMSE of the considered statistical models.

Both the SC-ExCell and SST performs with reasonable RMSE up to a probability of 1%, being the SC-ExCell slightly better. Above 1%, in the critical range for rain attenuation, both the models show a larger error compared to the reference ITU-R Recommendation. The mean value of the prediction error is shown in Fig. 2.7. It is clear that, especially for high probability values, i.e. low rain rates, both SST and SC-ExCell models underestimate the rain attenuation. The agreement between

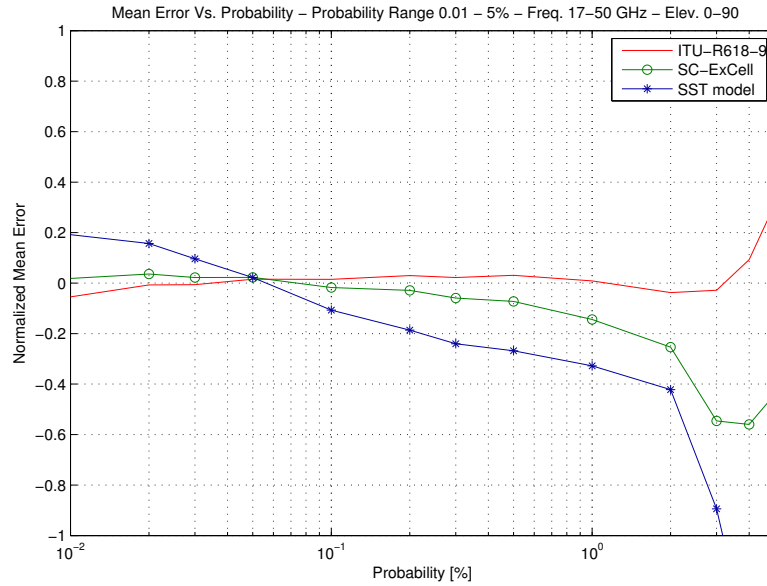


Figure 2.7: ME of SC-ExCell and SST models compared with reference model ITU-R P.618-10.

the models and the reference error is very high up to a probability of 2%, which is very close to the probability of rain, P_0 , value of the sites considered. It is worth to note that at high probability the underestimation of a prediction model is much more realistic than an overestimation. In fact, the reference measured CDF are more likely to be biased for an excess attenuation because of the not adequate identification of the 0 dB level.

The two models were also tested in predicting rain attenuation from measured rain rate $P(R)$ in the reference database DBSG3. Results in this case are almost equivalent for the SC-ExCell and SST model: Fig. 2.8 shows the RMSE and Fig. 2.9 shows the average error against the measured attenuation values. With respect to the SC-ExCell model, the SST suffers from a more significant underestimation but it has the advantage to be very efficient as for the computation time.

In conclusion, concerning rain attenuation prediction models, both the SC-

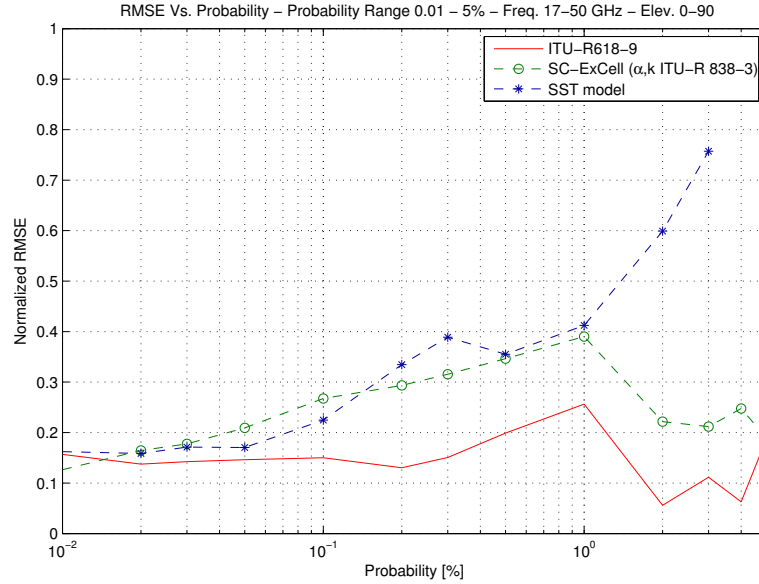


Figure 2.8: RMSE of SC-ExCell and SST models compared with reference model ITU-R P.618-10. Attenuation predicted from measured rain and compared with measured attenuation in DBSG3 database.

ExCell and SST offer a good accuracy in the evaluation of rain attenuation distribution compared to the statistical prediction model ITU-R P.618-10, up to the frequency of 50 GHz and for a wide range of elevation angles ($5^\circ - 90^\circ$). Performances are similar both considering statistical input rain distribution $P(R)$ from ITU-R map [31] compared and measured $P(R)$ available in the database DBSG3. The SC-ExCell exhibits a better RMSE especially at higher probabilities (low rain rates) but requires a longer computational time.

An example of application of SC-ExCell is provided in Fig. 2.10, which depicts the CCDFs of rain attenuation for a slant path at 37.7° at Spino d'Adda, Italy, for different frequencies.

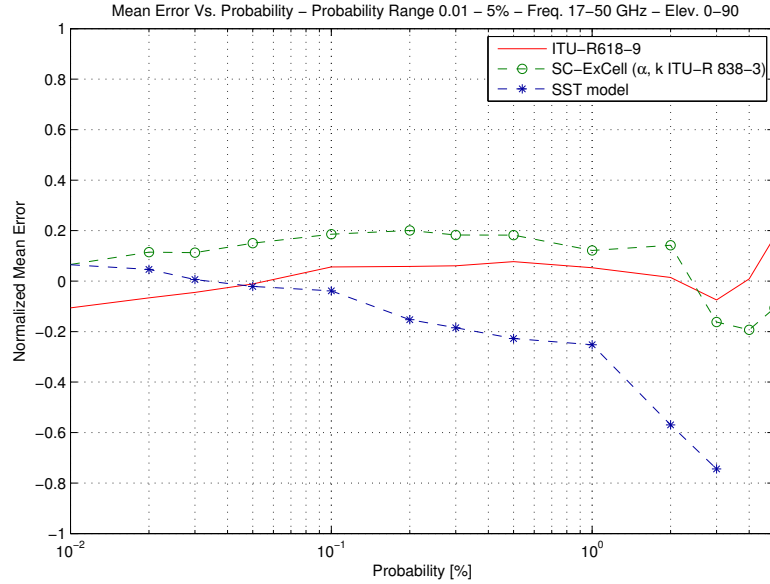


Figure 2.9: ME of SC-ExCell and SST models compared with reference model ITU-R P.618-10. Attenuation predicted from measured rain and compared with measured attenuation in DBSG3 database.

2.4.5 Combination of propagation effects

In system design, the combination of the multiple sources of simultaneously occurring atmospheric attenuation must be considered, especially for those systems operating with low margins. Total attenuation (dB) represents the combined effect of gas, clouds, rain and scintillation. According to Recommendation ITU-R P.618-10 [24], it requires one or more of the following parameters.

- $A_G(p)$: gaseous attenuation due to water vapour and oxygen for a fixed probability (dB), as estimated by Recommendation ITU-R P.676-9 [13];
- $A_C(p)$: attenuation due to clouds for a fixed probability (dB), as estimated by Recommendation ITU-R P.840-4 [16];

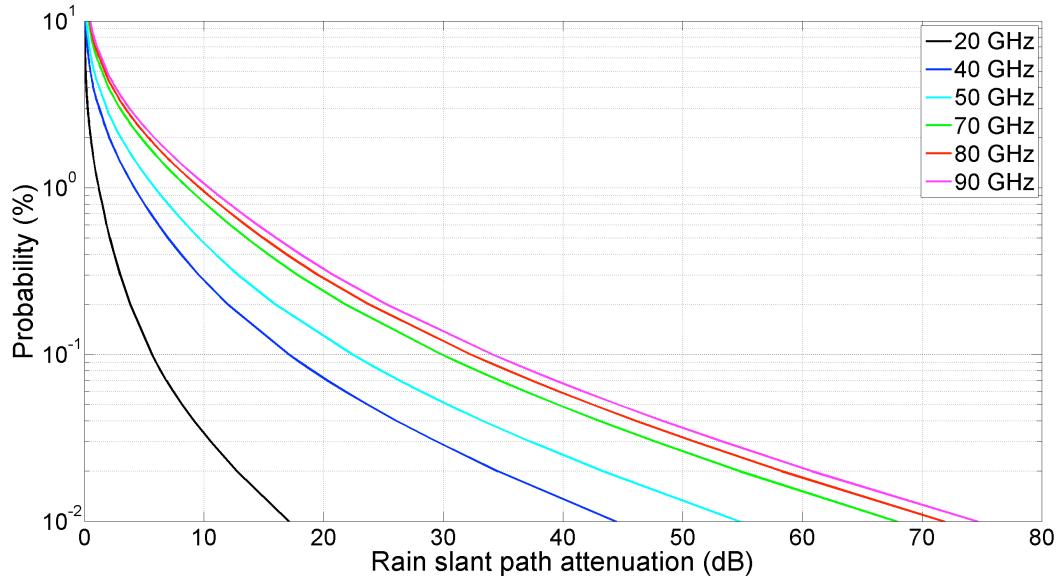


Figure 2.10: CCDFs of slant path rain attenuation at 20 (black curve), 40 (blue curve), 50 (light blue curve), 70 (green curve), 80 (red curve) and 90 (magenta curve) GHz for the site of Spino d’Adda, Italy (lat. 45.4° N, long. 9.5° E, alt. 84 m a.s.l.) along a 37.7° slant path (according to the SC-ExCell model)

- $A_R(p)$: attenuation due to rain for a fixed probability (dB), for example estimated from SC ExCell model [38];
- $A_S(p)$: attenuation due to tropospheric scintillation for a fixed probability (dB), as estimated by Recommendation ITU-R P.618-10 [24];

where p is the probability of attenuation being exceeded, in the range between 50% and 0.001%.

According to [24], a general method for calculating total attenuation for a given probability, $A_T(p)$, is given by:

$$A_T(p) = A_G(p) + \sqrt{(A_R(p) + A_C(p))^2 + A_S(p)^2} \quad (2.16)$$

where

$$A_G(p) = A_G(1\%) \quad \text{for } p < 1\% \quad (2.17)$$

$$A_C(p) = A_C(1\%) \quad \text{for } p < 1\% \quad (2.18)$$

$$(2.19)$$

The two previous equations take account of the fact that a large part of the cloud attenuation and gaseous attenuation is already included in the rain attenuation prediction for time percentages below 1%. In terms of the overall accuracy of the total attenuation estimation by Eq. 2.16, it is function of the accuracy over the single components and cannot be easily calculated. Difficult is also to measure the total attenuation of a beacon link (single carrier frequency) and to derive the single attenuation components. A common procedure is to evaluate the accuracy of the attenuation estimation for the single components. This work has been carried for the most recent rain attenuation models, which are of significant to the development of this thesis work.

2.5 Conclusions

This chapter presents a comprehensive overview of the effects of the atmosphere on radiowaves with operational frequency from 20 (Ka) to 90 GHz (W band). Specifically, the attenuation due to gases, clouds and rain have been separately illustrated, briefly the impact of depolarization and scintillations has been also introduced.

As for propagation under non-rainy conditions, state-of-the-art models, which rely on solid physical bases, show satisfactory prediction accuracy in the frequency range up W band. While models are well tested up to 50 GHz, a further increase in

frequency requires more work in terms of validation of rain attenuation, depolarization and scintillation models.

Considering rain attenuation, models which exhibit overall good performances compared to the reference prediction model ITU-R P. 618-10 [24] have been described and their accuracy has been assessed. The described models have been tested up to a frequency of 50 GHz, due to their strong physical basis their use above 50 GHz is definitely possible, but is not a topic of interest for this work. The SC-ExCell model [32] is selected as the one that gives better performance in predicting the rain attenuation distribution for a specific link.

The attenuation statistics (especially the attenuation CCDF) can be directly translated in system margin requirements to guarantee a maximum target outage probability. Considering an outage probability of 1%, where usually also a rain contribution has to be added being the probability of rain typically in the range 5–10%, the fade margin associated to non-precipitating atmosphere for the site of Spino d’Adda along a 37.7° slant path is approximately 1.5 dB in the Ka band (similar values are expected for other European sites with continental climate), rising up to 8-9 dB in the W band. Such attenuation levels are calculated by simply adding the attenuation values reported in Fig. 2.3 and 2.4, as recommended by ITU-R with the procedure described in Sec. 2.4.5.

For lower outage probabilities 0.1% – 0.001%, corresponding to a system availability of 99.9% – 99.999%, significant margins have to be accounted due to the heavy fades imposed by rain events. The modelling of these events appear, consequently, very important.

Results show that the attenuation levels for high availability systems (but in some cases also for low availability systems) become critical: the classical approach

for system design based on fixed power margin is no longer effective and adequate FMTs are required to achieve the desired QoS.

Fortunately, rain events are characterized by a limited spatial extension, especially considering large geographical areas. As well, the events duration is limited according to their temporal evolution. From this point of view, joint statistics of rain attenuation and, especially, time series of rain attenuation values appear of great interest.

Chapter 3

Generating correlated time series of rain attenuation for multiple sites

3.1 Introduction

In satellite communications, the utilization of high frequencies, such as the Ka band and beyond, is becoming necessary to avoid highly congested lower frequency bands and to achieve larger bandwidth availability. This solution is being considered for many developing High Throughput Satellite (HTS) systems. It is already in use for example in the KA-SAT launched by EutelSat [39] and Hylas-2, recently launched by Avanti Communications [40].

An immediate drawback at those frequencies is that the transmission link suffers from many limitations imposed by the propagation in atmosphere. Satellite low margin systems need to be designed accounting FMT to counteract difficult propagation conditions in the atmosphere. Among those, rain attenuation represents the most severe and critical aspect especially if high availability is requested.

For this reason, considering the service area of a satellite system for Multimedia Telecommunication or Broadcasting, joint statistics of rain attenuation in multiple locations are of great importance in the study of satellite networks which foresee the use of high frequency bands and FMTs. Looking at those applications, the possibility of generating long time series of rain attenuation, with the succession of rain and no

rain periods constrained to climatological information, appears of particular interest for statistical purposes.

In this Chapter a model to describe concurrent rain conditions at many stations in a large geographical area is presented. The model aims at preserving the spatial correlation of rain attenuation and its dynamic.

The model allows to obtain time series of rain attenuation for simulation purposes, properly arranged in rainy and not-rainy times in order to resemble the joint rain conditions for a large number of users in the geographical area of interest. In this work, the attention was focused on rain attenuation only, which represents the worst contribution to total attenuation for high availability satellite transmissions.

The obtained time series are of practical interest for the design of advanced TLC systems and communications link assessment: for example to describe the use of different modulation and codes for Adaptive Coding and Modulation (ACM) systems according to attenuation conditions.

The Chapter is organized as follows. Sec. 3.2 provides the main issues addressed in the model definition. Sec. 3.3 introduces recent works on the research topic, Sec. 3.4 introduces the proposed approach to the problem of modelling multisite rainy conditions. Sec. 3.5 presents the database of measurements which has been used as reference for the time series generation, Sec. 3.6 and relative subsections present the algorithm and the processes involved to generate correlated rain attenuation time series for multiple sites. Sec. 3.7 is devoted to assess the performance of the proposed methodology in terms of long-term statistics of rain attenuation, adaptability to different sites in Europe, the spatial distribution of rain and fade duration statistics. Sec. 3.8 presents this Chapter conclusions.

3.2 The TS model: map

The purpose of this work was to develop an advanced rain attenuation time series simulator for multiple sites. The proposed model has the particular feature of referring to a large database of acquired measurements, which are properly processed and arranged to reproduce different sites attenuation characteristics. The main characteristic is that attenuation values are not artificially reproduces but belong to real measured rain events. A mathematical model is required to assign measured time series to the different sites and to preserve: a) the spatial correlation among sites b) the rain events time evolution.

For this reason, the following processes are defined:

- *Rain state assigning process*: it is a multidimensional random process which assigns rain states to the considered sites with a temporal step of 1 hour. Rainy states depend on some climatological information related to the sites of interest. The most important characteristic developed at this stage are: a method to impose the correct spatial correlation of rainy states; a model for the temporal correlation of rainy states.
- *Rain time series assigning process*: it is a method to arrange and distribute the attenuation measurements present in the reference database to the rainy states identified by the previous process. The method purpose is twofold: on one side, attenuation time series must reproduce the attenuation statistical distribution of the considered sites; on the other side attenuation time series should be spatially correlated according to the rainy sites distance. Given the time evolution of the conditioning process, resulting time series are composed of rainy events with duration multiple of the basic time period (1 hour).

The two independent processes allow to obtain correlated time series of rain attenuation for each considered sites, imposing the correct spatial correlation of rain events occurrence and attenuation. Time series are generated for each site for a specific simulation duration (1 year for example), aiming to reproduce the long-term statistics of attenuation specific for each site. The time resolution is the same of the original measurements and equal to 1 sample/sec.

The proposed model is deeply discussed in the following, along with its performance assessment against reference statistical models available to public domain. A direct comparison with time series generators developed by other authors has not been possible in terms of final results.

3.3 Overview of recent developments in the research topic

In this section, recent models devoted to the modelling of multisite rain attenuation conditions are reported. Only the models able to generate time series for multiple sites (space-time channel simulators) has been considered.

The modelling of rainfall events with their physical characteristics is not a new research topic but still receives significant interest [41]: it is a cross-disciplinary research area which finds applications not only in communications [42, 43]. Purely mathematical models present the main difficulties in the need to take into consideration the complete statistical and dynamic information of the rain process. Among these, Markov models for similar applications are discussed in [44].

Very recently new models to describe multisite rain attenuation conditions has been developed, marking the importance of this research topic for propagation studies.

Those models require a parameterization reflecting the rain rate or rain attenuation distribution for the considered link as well as parameters describing the spatial and temporal correlation of the rain and rain attenuation fields. These models are of great importance to provide reliable inputs for FMTs and Radio Resource Management (RRM) design and optimization. Below, the most recent models are listed and briefly presented.

Authors of [45] proposed a model to generate spatially and temporally correlated rain attenuation fields for propagation studies. It lies on a non-linear transformation of random Gaussian fields constructed in the Fourier plane. A methodology is proposed to derive spatio-temporal correlation parameters from radar data and the applicability of the mathematical framework for a large geographical area is discussed. The model is based on a combination of random fields and reanalysis data to generate rain field with a resolution of 1 km in space and 6 min in time. Those rain attenuation fields are afterwards converted into rain attenuation fields and interpolated at high resolution using the methodology of [46]. This approach has been extended to the simulation of total attenuation fields.

Authors of [47] use a single fractal representation of the rain fields to obtain time series of rain attenuation. The temporal evolution is obtained by advection of the rain field whose parameterization has been derived from a set of weather radar data in the UK. Another approach based on radar data is presented in [48]. In that work, authors make use of operational weather radar data to downscale time series of rain attenuation on various types of link. The downscaling technique relies on multiplicative cascades and enables to get time series of rain attenuation at one second of resolution.

In [49] a continuous multidimensional stochastic model simulating rain attenuation in multiple links is introduced. The model aims to generate time series of

rain attenuation by generalizing the Maseng-Bakken model [50] to multiple radio links, modelling their spatial behaviour. The model reproduces quite encouraging results concerning the long-term properties of rain attenuation (outage probabilities), however further testing in relation to second-order properties of rain attenuation at different sites is being carried by authors. The limitation of the model's applicability in Earth-space diversity systems is 10–30 GHz for the frequency, 5–60° for the elevation angle, 0.001%–5% for the exceedance probability, and for rain attenuation values greater than 1 dB. Concerning the spatial dimension, 1.7–200 km is the range stated for the site separation distance. Authors referred also to the simulation of the orbital diversity systems, with angular separation up to 50°.

In [51], the rain attenuation dynamics in time and space are discussed starting from a set of diversity measurements obtained by a star-like network at 42 GHz. By combining the spatial and temporal correlation properties of rain attenuation, a simulation model to generate multiple rain attenuation time series based on the Maseng-Bakken model is developed. The model is validated by comparing the statistical and angular diversity properties of the model with those of measurements and theoretical diversity gain for small distances (few km), with a target application of generating time series of rain attenuation for cellular wireless access systems.

These very recent works prove the importance of accurately describing concurrent rain attenuation conditions on multiple radio links. The reported works aim at generating time series at 1 sec time resolution, either by direct mathematical modelling or by over sampling procedures of larger scale rain fields information.

As described above, many of the proposed models lies on the mathematical framework developed by T. Maseng and P. M. Bakken and described in [50]. The M-B dynamic single-site model is based on the Log-Normal distribution of rain attenuation. A non linear transformation allows to describe rain attenuation or intensity as a one-

dimensional Gaussian stationary Markov process. The Markovian assumption is the simplest probabilistic concept that takes into account the dependency on the last observation solely. The phenomenological description that is obtained by a first-order Stochastic Differential Equation (SDE) has proved to be consistent with experimental results [52]. However, the M–B model refers to a specific single link and does not incorporate the spatial variability of rain attenuation. The M–B model has been adopted by the ITU-R as Recommendation ITU-R P.1853 [53].

The model allows the stationary distribution function of rain attenuation to be described by two parameters, average attenuation μ_α and standard deviation σ_α of $\log \alpha$. The time dependence is described by a single parameter β .

The stationary distribution of the rain attenuation of the model is lognormal, therefore is characterized by two parameters which can be determined from long-term attenuation statistics. The additional parameter β allows to model the rate of change of attenuation in time. When β is known, the model can be used to calculate dynamic properties of rain attenuation such as fade duration statistics and typical profiles of rain attenuation as function of time.

The analytical expression

$$R_\alpha(\tau) = \mu_\alpha^2 \exp(\sigma_\alpha^2(1 + \rho(\tau))) \quad (3.1)$$

gives the correlation in time of the rain attenuation obtained by the model, given that the Gaussian variable $x(t)$ input to the model exhibits the exponential correlation:

$$\rho(\tau) = \exp(-\beta|\tau|). \quad (3.2)$$

The M-B [50] represents a stochastic dynamic description of rain attenuation for a

single site. The model is applicable only during rainy periods because no dynamic transition mechanism between rainy weather and clear sky conditions has been incorporated. An advantage of the model is its simplicity in the rain attenuation distribution and the time-evolution dynamic.

3.4 The proposed approach to multisite modelling

An alternative solution to obtain time series of rain attenuation is the use of real data collected from propagation experiments. The idea of referring to real acquired measurements has the attractive advantage that all the features of the simulated process (i.e. the rain event) are real and are not artificially reproduced. Even though the series are truly measured, their practical use requires a statistical description of the rain attenuation based on a mathematical model. The use of a large dataset of rain attenuation measurements for simulation purposes is suggested in [6]. Authors provide an extensive assessment of the possibility to reproduce first order and second order attenuation statistics for a generic radio link starting from the desired long-term CDF of rain attenuation. The model proposed in [6] select a set of rain events from the database of measurements, which represent the correct rain attenuation statistics for the single site. Series are composed only by rain attenuation values. The model assumes that the complete dataset of rain attenuation events measured at a specific site contains the rain attenuation events potentially measured at a different site, even if at the two sites their occurrence can be different.

Authors of [54, 55] proposed the use of time series extracted from the same database of measurements as in [6], but aiming to describe rain attenuation conditions in multiple sites. The study proposed in [55] lies on the two-processes description in [54]: one describing the rain event occurrence and the second the rain event atten-

uation. The straight mathematical methodology presents some limitations especially in terms of the convergence time to reach the long-term desired rain attenuation CDF, which makes the model not applicable for the purpose of generating time series of duration equal or longer than one year. Moreover, while the long-term convergence was discussed, some issues concerning time dynamics and spatial correlation of rain events remained unsolved.

The work developed targets a methodology to generate time series of rain and no rain attenuation for multiple sites and should be considered as an extension of the framework proposed in [55]. To a difference with respect to that work, a time evolution among rainy states is introduced, and a new methodology to impose the correct spatial correlation of rain occurrence among the sites is developed. As a consequence, a better accuracy in reproducing the correct CCDF of rain attenuation is achieved by generating time series of duration equal or longer than one year. Moreover, the correct spatial correlation among rainy times and their average attenuation is obtained. Finally, a temporal evolution model based on the correlation time interval is introduced.

Similarly to [49], the proposed methodology assumes time stationarity and spatial isotropy of the driving random processes which model the advent and duration of a rain event. The instantaneous attenuation evolution within the event duration is instead described by actual measured series, preserving the correct attenuation dynamic within the time frame duration. The use of measured time series of rain events and their correlation are specific characteristics of the proposed model compared to those introduced in 3.3. Moreover, the developed efficient methodology allows to generate and allocate time series for a large number of users, with high flexibility in terms of geographical distances (small and large scale simulations).

3.5 Database of data

The rain attenuation measurements which compose the reference dataset were collected in the station at Spino d’Adda, Italy, during the ITALSAT experiment in the period 1994 – 2000. The characteristics of Spino d’Adda station can be found in [56].

The reference dataset contains only rain attenuation values (1 sample/sec), collected at a frequency of 18.7, 39.6, 49.5 GHz with elevation 37.7° . Measurements were processed to identify the rain events, gas and clouds components have been separated. The database contains more than $9 \cdot 10^6$ samples of rain attenuation events, roughly equivalent to 2547 “rainy” hours. Zeros, corresponding to not rainy times, are not present in the database. In order to separate rain attenuation from scintillation, a low-pass filter (cut-off frequency 0.025 Hz) has been used [6]. A scaling procedure was introduced to adapt the values to the desired frequency to be simulated. More detailed information about the measurements database are reported in [55].

A widely assumed model to describe the rain attenuation cumulative distribution function is the Log-Normal distribution [55]. The Gaussian description has the desirable property that the statistical distribution of rain attenuation is simply described by the first two moments (mean value and variance) of the distribution. The Log-Normal approximation well describes rain attenuation up to moderate values, Fig. 3.1 shows the CCDF of rain attenuation at Spino d’Adda, Italy, for a link at 39 GHz, elevation 37.7° . The long-term rain attenuation curve is obtained by the SC-ExCell model [32], the Log-Normal distribution exhibits a high accuracy down to a probability value of almost $10^{-3}\%$, which is equivalent to a time of 6 minutes per year. This level of probability is considered satisfactory for most of the applications and the purpose here discussed. For each site of interest, the Log-Normal curve, obtained by a fitting of the attenuation distribution provided by the SC-ExCell model,

represents the reference distribution of attenuation to be satisfied by the time series generated by the proposed model.

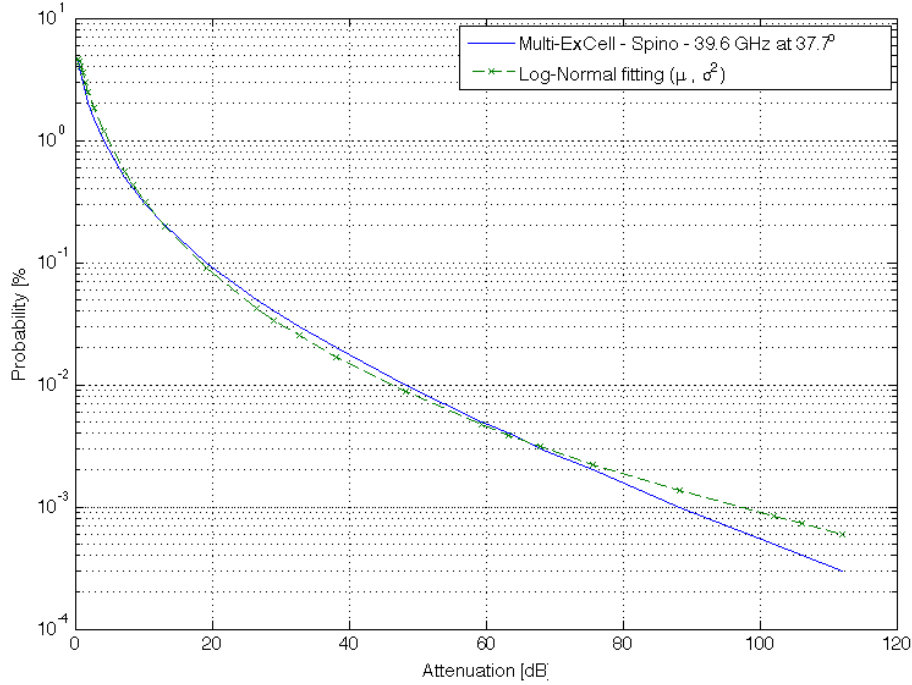


Figure 3.1: Complementary Cumulative Distribution Function (CCDF) of rain attenuation for a satellite link at 39.6 GHz, elevation 37.7° at Spino d'Adda (Italy) as derived from the reference model SC-ExCell (blue solid line) and the Log-Normal approximation (green dashed line). The agreement of the Log-Normal model is high almost down to a probability of $2 \cdot 10^{-3}\%$, roughly equivalent to 10 minutes/year.

3.6 Model and Algorithm description

In this section, we describe the algorithm which allows to obtain a set of correlated rain attenuation time series for satellite links over a large geographical area. The aim of the developed model is to generate time series of concurrent rain events to simulate the conditions of rainy/not rainy times for a set of stations over a general reference area of $250 \text{ km} \times 250 \text{ km}$.

Three issues are newly addressed here which extend and refine the framework proposed in [55], in order to generate correlated time series which include not rainy periods. Firstly, a multidimensional random Gaussian process is used to generate rainy times with time step 1 hour, a temporal and spatial correlation is imposed to the rainy events. Secondly, for the purpose of generating concurrent time series for many stations, an efficient approach in generating the joint statistics among sites is developed, based on the mutual attenuation correlation to be imposed among the subset of rainy stations. Thirdly, the statistics (single and mutual) should be reasonably accurate even for a single simulated year, which accounts a limited number of rainy time according to each single site rain probability. For this reason, the choice of the series is optimized to reproduce the desired CDF with a maximum number of series.

The proposed model consists of two independent mathematical processes, which are detailed in the following sections. The first conditioning process assigns rain/no rain time over the possible stations, correlating the rainy times according to a specific spatial distribution and imposing a correlation interval for rain events. The second conditioned process generates the correlated time series of rain attenuation from available data, only for the links in rainy conditions. The independence of the two processes was already addressed and discussed in [54]. The spatial correlation of rain events and rain attenuation is imposed in the two processes separately according to [24, 54].

The model generates time series of rainy and non rainy times for multiple sites at the same time, the time evolution is arranged in basic periods of 1 hour duration called “epoch”, similarly to [55]. Rainy events are characterized by a random number of “epochs” according to the rain process time correlation interval. Each rainy “epoch” is filled with a time series of rain attenuation extracted by the database of

measurements. The choice of 1 hour for the “epoch” duration is supported by statistics of the rainy events recorded in the database, which exhibit a correlation interval slightly above 30 min [57]. The choice of a larger time period allows enough dynamic of rain attenuation within the “epoch” duration, which is discussed later in terms of fade duration statistics.

The series of measurements are arranged to reproduce the attenuation characteristics of the desired links. The main variable involved in the series selection is the average rain attenuation over the epoch duration \bar{a}_e . The model inputs are the following: the geographical information of the stations (latitude, longitude, height above sea level), the link parameters (frequency, polarization, elevation angle), the probability of rain and the rain rate exceeded cumulative distribution function [31] and the spatial rain correlation, both in terms of rain probability and attenuation probability [24]. Those statistical information allow to reproduce the rain attenuation complementary cumulative distribution function (from now on referred as $P(A)$) of each station by a proper selection of measured “epochs”. The model carefully reproduces the correct single site and joint statistics of attenuation over the selected area for a specific simulated time (1 year or more).

3.6.1 Rain parameters definition

The first step of the algorithm is to define the characteristics of rain attenuation for the set of stations of interest and identify a proper set of measurement series to reproduce the desired statistics, in order to suitably exploit the rain attenuation database. Given a set of N stations in the geographical area of interest, their geographical coordinates and height above sea level are defined. The spatial rain correlation characteristics are derived according to the models in [54] and the ITU Recommendation P.618-10 [24],

based on the geographical distances among the stations (a matrix of mutual distances \mathbf{D}_M is defined).

Rain attenuation for the satellite link depends on frequency, polarization, link geometry (elevation and equivalent length) and rain intensity [38]. Those information, together with the rain rate complementary cumulative distribution function [31], are used in the SC-ExCell model [32] to obtain the rain attenuation $P(A)$ for each the desired link.

The Log-Normal assumption for rain attenuation allows to refer to the properties of Gaussian processes, which are of particular interest in evaluating the probability of rain attenuation values and in directly imposing the correlation of rain distribution.

For each station, the rain attenuation $P(A)$ derived from SC-ExCell, conditioned to the rainy time, is fitted to a Log-Normal distribution, deriving the mean value μ_a and variance σ_a^2 for each of the N links. The objective is now to select a set of series to reproduce the desired attenuation statistics. The parameter of interest is the average rain attenuation over the “epoch” duration, defined as:

$$\bar{a}_{e,i} = \frac{\int_{t_0}^{t_0+T} a(t) dt}{T}, \quad (3.3)$$

where $\bar{a}_{e,i}$ is the average attenuation over the “epoch” for the i -th station, $T = 30$ min represents the “epoch” time duration, $a(t)$ is the instantaneous rain attenuation as provided in the database of measurements. The same definition holds for different “epoch” durations. The distribution of the time-averaged values is still Gaussian and differs from the instantaneous distribution only in its variance σ_a^2 [55]. In order to well reproduce the attenuation distribution, the Log-Normal $P(A) N(\mu_{\bar{a}}, \sigma_{\bar{a}}^2)$ is divided in K intervals (classes) of equal size over the attenuation dimension. A number of classes $K = 15$ was chosen by numerical simulation to cover the attenuation range,

the dimension of each class is fixed and related to the attenuation distribution to be represented. A minimum and maximum values of attenuation A_{min} and A_{max} are defined to limit the tails of the probability distribution, they depend on the target $P(A)$ to be represented. In order to correctly reproduce the desired $P(A)$, the area of each interval is translated into a discrete number of occurrence, which corresponds to a number of series to be extracted from the database, with average attenuation value belonging to the specific class. Given a maximum number of series S_{max} for each station, the number of occurrence S_k for each attenuation class is properly scaled to satisfy:

$$S_{max} = \sum_{k=1}^K S_k, \quad (3.4)$$

where S_{max} corresponds to the rain probability over the simulation time, i.e. the climatological probability of rain attenuation P_0 obtained by [31]. This first selection process results in a set of S_{max} time series (Auxiliary Dataset, AD) for each station, which are selected from the database of measurements according to their average value $\bar{a}_{e,i}$ and reproduce the target long-term attenuation distribution $P(A)$ of each station.

At this stage, no spatial correlation among the selected series is imposed. The AD contains a set of series which reproduce the desired statistics of attenuation for each site of interest. The spatial and temporal correlation among the stations are imposed by the procedure proposed in the next subsections.

3.6.2 Rain state variable assigning process (conditioning process)

Considering N stations randomly placed in the reference geographical area, the state of all the stations at each epoch is described a N -dimensional binary variable which

defines the condition “rainy” or “not rainy”, depending whether a threshold value at each site is exceeded or not exceeded.

The “rainy” or “not rainy” state is assigned by means of the probability density function of an N -dimensional continuous variable r_i , with $i = 1, \dots, N$, and by an N dimensional thresholds t_i , chosen according to the probability of rain for each location and according to the correlation information. The continuous “rain state variable” r_i for the i^{th} location can be selected with a high degree of freedom. The assumption here is a Gaussian multi-variate variable normalized to zero mean and unit variance, with covariance matrix imposed to represent the desired joint statistics presented. For the purposes of the proposed model, the conditioning process reproduces the link attenuation probability P_0 of each single station and the rainy time space correlation among the N stations set for a typical time series duration of 1 simulated year. The threshold t_i , which defines whether the station condition is “rainy” or “not rainy” is chosen to fulfil:

$$P(t_i) = \int_{-\infty}^{t_i} p(r_i) dr_i = 1 - P_{0,i}, \quad (3.5)$$

where $P_{0,i}$ is the probability of having rain in the i^{th} station.

According to the variable r_i and the set threshold t_i , a binary process z_i is obtained to describe rainy conditions at each “epoch”:

$$z_i = T_z(r_i) = \begin{cases} 1 & : r_i > t_i \\ 0 & : r_i < t_i \end{cases} \quad (3.6)$$

The hard threshold imposed to the continuous variable r_i is actually a non-linear transformation T_z , which results in a binary process in which 1 corresponds to a rainy “epoch”, 0 to a non-rainy “epoch”. The imposed threshold has a significant effect on

the correlation characteristics of the resulting process z_i [58]. For this reason, defining the output process the one after the non-linear transformation, the correlation of the input process r_i was analytically derived from the knowledge of the desired correlation of the output process z_i , which describes the rain events.

This issue was solved by referring to the general theory of noise clipping [58, 59]. Particularly, the correlation of a random Gaussian process after the non-linear transformation can be rewritten as:

$$M_z(d) = \frac{1}{\sigma^2} \sum_{n=1}^{\infty} \left\{ \int_{-\infty}^{\infty} T_z(r) \Phi^{n+1} \left(\frac{r}{\sigma} \right) dr \right\}^2 \frac{R_r(d)^n}{n!}, \quad (3.7)$$

where $R_r(d)$ is the correlation of the input process and Φ^{n+1} is the n^{th} derivative of the standard Gaussian density function:

$$p(\xi) = \frac{1}{\sqrt{2\pi}} \exp \left\{ -\frac{\xi^2}{2} \right\}. \quad (3.8)$$

The Rodrigues formula [60] allows to rewrite the n^{th} derivative by using the Hermite polynomials. In this way, the series in Eq. 3.7 becomes a polynomial of order n in which, at any given d , the unknown is the input correlation $R_r(d)$. The convergence of the series is guaranteed by an infinite number of Hermite polynomials in the expansion in Eq. 3.7. Simulations considering different clipping threshold shown that the correlation function converges very fast with a small number of expansion terms, except from the samples close to $d = 0$. This is expected from theory, according to which the convergence at unity is guaranteed by the infinite number of terms in Eq. 3.7. A study of the error of the correlation function as function of the distance d was carried, allowing to choose the most convenient number of terms in the series to be $n_{exp} = 20$. The polynomial resulting from Eq. 3.7 is consequently solved to obtain

the input process correlation, which is then imposed in the N -dimensional continuous variable r :

Fig. 3.2 shows the result of the pre-filtering process described above. It was applied to the simulation of rainy conditions over 500 stations randomly placed in a geographical area of 250 km \times 250 km around Spino d'Adda station, Italy, as shown in Fig. 3.3. The simulated time is 1 year, equivalent to 17520 “epochs” of 30 minutes each. The desired correlation among rainy times is given by the following expression [24, 54]:

$$\rho_s(d) = 0.7 \exp\left(-\frac{d}{86}\right) + 0.3 \exp\left(-\frac{d}{700}\right)^2. \quad (3.9)$$

It is clear from the figure that the correlation evaluated from the generated binary sequences well follow the reference curve of Eq. 3.9, also for critical high correlation values (distances smaller than 50 km). According to the proposed reference model, the de-correlation distance for rain events can be considered to be around 250 km.

The time dynamics of the rain attenuation for the link i is modeled by a first order lowpass filter $H_i(z)$, with impulse response [50]:

$$H_i(z) = \frac{\sqrt{1 - \rho_i^2}}{1 - \rho_i z^{-1}}, \quad (3.10)$$

where ρ_i is the temporal rain attenuation for link i :

$$\rho_i(\tau) = \exp(-\beta_i |\tau|), \quad (3.11)$$

in which τ is the time interval between two samples and β_i is the dynamic parameter for the link i . The calculation of the dynamic parameter from experimental data

is discussed in [1]. The effect of β is directly related to the duration of the rainy states, time correlation within the rainy states is already present in the measured time series. For this reason, we assumed the dynamic parameter $\beta = 2 \cdot 10^{-4}$, value that is generally applicable to describe the correlation interval of stratiform rain events.

By the same pre-filtering procedure explained before, the correlation of Eq. 3.11 is correctly imposed to the binary conditioning process. The complete study of the pre-filtering method here summarized is reported in Appendix A. The conditioning process allows to generate spatially correlated rainy time among the N stations considered, with temporal evolution controlled for each link by the β parameter.

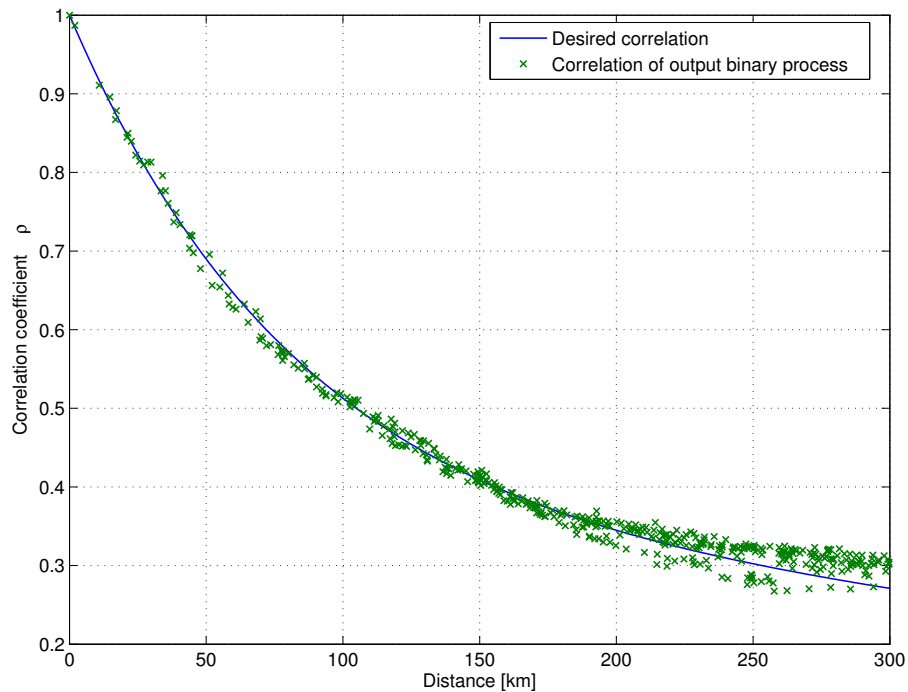


Figure 3.2: Spatial correlation of rain events obtained by the conditioning process compared with the desired reference correlation.

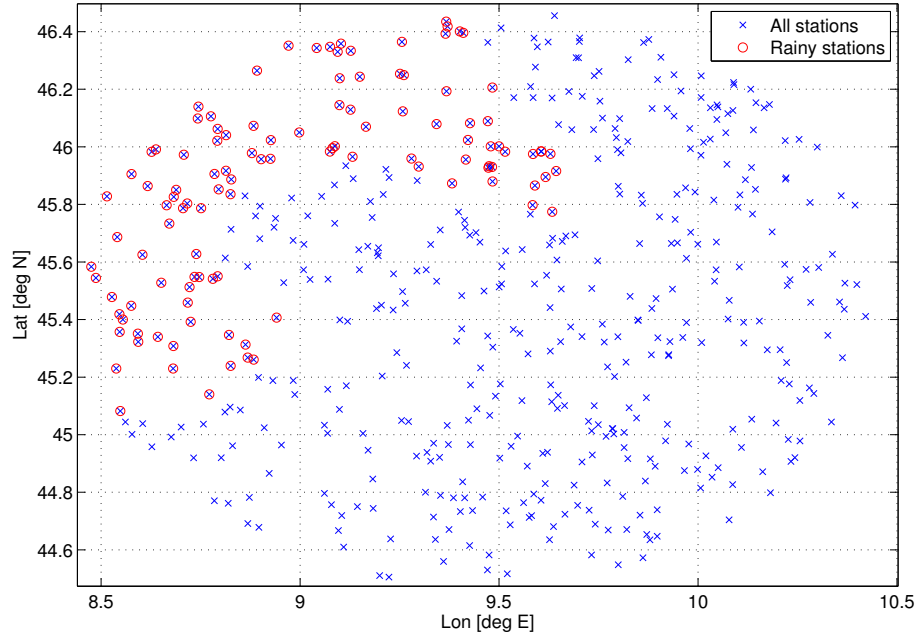


Figure 3.3: Representation of stations in the geographical area of interest. 500 stations are randomly placed in the area $250 \text{ km} \times 250 \text{ km}$ centred at Spino d’Adda. Red circles show the rainy stations at a single “epoch” as obtained by the rain assigning process (conditioning process). Note the well defined rainy area consequence of the spatial correlation imposed in the assigning process.

3.6.2.1 On temporal evolution of rainy states

The temporal evolution of single sites rainy states is described here based on the dynamic parameter β (s^{-1}) [50], used in Eq. (3.10). The value of β is discussed here based on different analysis.

The dynamic parameter β describes the time evolution of the rain attenuation process. It is defined as the correlation interval of the process, according to the exponential correlation coefficient:

$$\rho = \exp(-\beta\Delta t); \quad (3.12)$$

where Δt is the time interval between two process samples. It is the same model used in [50] to describe the rate of change of attenuation in time. A small value of β corresponds to slowly varying rain attenuation dynamics. For a given rain event, the parameter β can be associated to the physical characteristics V_m , D_m respectively the average advection velocity (m/s) of the rain structure and its diameter (m) according to [61]:

$$\beta \approx \frac{V_m}{D_m} \quad (s^{-1}). \quad (3.13)$$

Small values of V are associated with rain events having low maximum rainfall intensities corresponding to stratiform rain. Large values of V are associated to convective rain, characterized by large maximum rainfall. The dynamic parameter β can be derived from experimental results [1, 45, 57] or from specific optimization processes. The correlation time is derived from radar data in [45] while authors of [62] derived the dynamic parameter to optimize the model fade duration statistics.

In the study described in [1], β is extracted by measurements in different experiment in North-western Europe. The β parameter influences in particular the autocorrelation and consequently the Power Spectral Density (PSD) of rain attenuation $A(t)$, as well as the first two conditional moments of rain attenuation [50]. The method to infer β from acquired data relying on the second order conditional moment of $A(t)$, $K_{2A}(A)$ is the most direct one and favoured to estimate the parameter value on a long-term basis. The analytical expression of $K_{2A}(A)$ is given by:

$$K_{2A}(A) = \frac{\mathbf{E} \left\{ (A(t + \Delta t) - A(t))^2 \right\}}{\Delta t} = 2\beta A^2 \sigma \quad (3.14)$$

where σ is the standard deviation of $\log A(t)$. First, the influence of the scintillation (low amplitude but fast dynamics) has to be removed in order to isolate rain

attenuation (significant amplitude but low dynamics with respect to scintillation). A low-pass filtering with cut-off frequency 0.025 Hz is normally used. Then, a set of attenuation thresholds (0 to 10 dB for example) and discrete time lags (1 to 100 s) is chosen: $K_{2A}(A, \Delta t)$ is evaluated for each time lag and attenuation threshold. A linear regression based on the relation:

$$\sqrt{\Delta t \cdot K_{2A}(A)} = \gamma(\Delta t)A \quad (3.15)$$

allows to evaluate the slope $\gamma(\Delta t) = 2\beta\sigma^2\Delta t$ for each Δt for a specific attenuation range (typically $2 < A < 10$ dB). A final linear regression is made on $(\Delta t, \frac{\gamma^2}{2\sigma^2})$ which gives the estimation of the β parameter.

The resulting estimation of β based on a set of experiment listed in Table 3.1 is discussed in [1]. The study shows that a typical value of $\beta = 2 \cdot 10^{-4}$ does not strongly affect the dynamics of the rain attenuation compared to experimentally derived values. The conclusion reported in [1] is that, without any local information on the dynamic parameter, a rough estimate of β for a link in the North-western Europe, for elevation angles between 25° and 38° and frequencies between 12 and 50 GHz is 10^{-4}s^{-1} .

Table 3.1: Estimated β values from different experiments in North-western Europe [1]

Name	Country	Freq. [GHz]	Elev. [deg.]	β [s^{-1}]	Duration
Spino d'Adda	Italy	18.7	37.8	$9.5 \cdot 10^{-5}$	7 years
"	"	39.6	"	$1.03 \cdot 10^{-4}$	"
"	"	49.5	"	$6.5 \cdot 10^{-5}$	"
Sparsholt	U.K.	19	29.9	$3.15 \cdot 10^{-4}$	46 months
"	"	40	"	$2.6 \cdot 10^{-4}$	"
Louvian la Neuve	Belgium	12.5	27.6	$3.6 \cdot 10^{-4}$	21 months
"	"	30	"	$2.44 \cdot 10^{-4}$	"
Lessive	Belgium	12.5	27.8	$3.13 \cdot 10^{-4}$	2 years
"	"	20	"	$2.43 \cdot 10^{-4}$	"
Oberpfaffenhofen	Germany	40	34.8	$1.53 \cdot 10^{-4}$	4 years
Gometz la ville	France	20	30.32	$2.57 \cdot 10^{-4}$	1 years
"	"	30	"	$1.99 \cdot 10^{-4}$	"
Le Folie Bessin	France	20	30.33	$1.74 \cdot 10^{-4}$	1 years
"	"	30	"	$1.45 \cdot 10^{-4}$	"

In addition, a study on the ITALSAT beacon measurements of rain attenuation is reported in [57] for the data relative to the year 1994 and frequency 18.7 GHz. Table 3.2 shows the values of the dynamic parameter $\beta = 1/T_{corr}$. Must be noted

that authors of [57] considered T_{corr} as the time interval after which the correlation coefficient is $\rho = 0.5$. Consequently, the derived correlation interval is smaller than the value for which $\rho = 1/e$. The time correlation interval is extracted by 425 rain events recorded during year 1994, with average duration 54 min. The yearly average rain attenuation is 2.62 dB and a threshold for convective events is set at 7 dB.

Table 3.2: Estimated β values from Spino d'Adda beacon measurements

Name	Statistic	Freq. [GHz]	Elev. [deg.]	T_{corr} [min]	β [s^{-1}]
Spino d'Adda	above 2.62 dB	18.7	37.8	27.9	$5.9 \cdot 10^{-4}$
Spino d'Adda	above 7 dB	18.7	37.8	27.6	$6 \cdot 10^{-4}$
Spino d'Adda	above (54 min, 2.62 dB)	18.7	37.8	36.1	$4.5 \cdot 10^{-4}$

From Tab. 3.2 it is clear that the correlation time interval considering attenuation $A > 2.62$ is very similar to the one obtained for $A > 7$ dB is typical of convective events. Unfortunately, no results are discussed for lower thresholds of attenuation. Interesting is the longer correlation interval for events with duration above 54 min, which is more applicable to stratiform phenomena. Also must be noted that correlation interval would be longer if evaluated for $\rho = 1/e$ instead of $\rho = 0.5$.

In conclusion, a reasonable value of the dynamic parameter to describe rain attenuation time evolution is $\beta = 2 \cdot 10^{-4}$ [1]. This value allows to model the evolution of attenuation due to stratiform events, which are the longer in time. When available, the value of the β parameter can be extracted by local data, especially referring to the average velocity V_m and the average spatial dimension of rain structures D_m . The value of β is used to model the correlation interval of the rainy states in the

simulated process. The desired time correlation is added to the binary sequences previously generated, resulting in a binary space/time correlated multidimensional process. Different correlation can values be easily included in the model, resulting in different time evolution of the spatially correlated binary sequences.

3.6.3 Rain time series assigning process (conditioned process)

Within this second process, the identified series in the auxiliary dataset (AD) are arranged to show the correct spatial correlation for the stations characterized by concurrent rainy times, as resulting from the previous conditioning process in Sec. 3.6.2. The desired spatial correlation of rain attenuation is the one proposed as reference in [24, 54]:

$$\rho_s(d) = 0.94 \exp\left(-\frac{d}{30}\right) + 0.06 \exp\left(-\left(\frac{d}{500}\right)^2\right). \quad (3.16)$$

The following passages allows to impose the desired correlation in terms of average rain attenuation $a_{e,i}$ among the selected series in the auxiliary dataset defined in Sec. 3.6.1. Being $i = 1, \dots, R$ the number of sites under rainy conditions at a given “epoch” according to the conditioning process, a set of uncorrelated average attenuation values $a_{e,i}$ for the rainy stations is extracted from the previously identified auxiliary datasets. The desired mutual correlation among stations, related to the matrix of mutual distances \mathbf{D}_M , is given by matrix \mathbf{R}_M from Eq. 3.16. Considering $\xi = [a_{e,1}, a_{e,2}, \dots, a_{e,R}]$ as a realization of an independent random process ξ , the desired correlation among samples is imposed by a Cholesky decomposition of the correlation matrix \mathbf{R}_M . The new process ζ is defined as:

$$\zeta = \xi \mathbf{A}^T; \quad (3.17)$$

where the \mathbf{A} is the Cholesky decomposition of the desired correlation matrix:

$$\mathbf{R}_M = \mathbf{A}^T \mathbf{A}. \quad (3.18)$$

The correlation of the new process ζ becomes:

$$E[\zeta \zeta^T] = \mathbf{A}^T \mathbf{A} E[\xi \xi^2] = \mathbf{R}_M \sigma_\xi^2, \quad (3.19)$$

which is the desired spatial correlation \mathbf{R}_M weighted by the variance of the original random process ξ . The output process ζ is a new set of average rain attenuation values over the “epoch” duration, which statistically exhibits the desired correlation properties. The linear transformation in Eq. 3.17 applied to a Gaussian process results in a new Gaussian process [63], thus not affecting the desired statistic of rain attenuation previously obtained. Given the vector ζ of desired rain attenuation for the stations, a maximum likelihood procedure allows to choose the best set of available series, obtaining a vector $\tilde{\zeta}$ which minimizes the mean square error with ζ . In this way, the auxiliary dataset of series, whose statistic well represent the target site $P_i(A)$, are arranged in time to show the proper correlation, as close as possible to the theoretical one imposed by the Cholesky decomposition. In a mathematical formulation, the final set of average rain attenuation values $\tilde{\zeta}$ satisfies:

$$\tilde{\zeta} = x : \min \sum_{i=1}^K (\zeta_i - x_i)^2. \quad (3.20)$$

The error in terms of attenuation correlation obtained by the maximum likelihood selection is limited when a large auxiliary set is available, while the benefit of this approach is more relevant since the auxiliary set guarantee the correct reconstruction of each single site $P_i(A)$.

The following figures show the results obtained by the described correlating procedure. Fig. 3.4 shows the correlation among the simulated rain conditions for the station of Spino d’Adda and 5 other stations at different distances. For each station, a set of 1000 series of rain attenuation samples are selected and arranged to describe the target spatial correlation among the stations. The duration of each series is the “epoch” duration of 30 minutes, consequently a number of 1000 series represent with good approximation the probability of rain over 1 year for a site similar to Spino d’Adda.

The correlation of the ideal rain process ζ , obtained by applying the Cholesky decomposition in Eq. 3.17, is compared with the reference correlation function in Eq. 3.16. As clear, the rain attenuation correlation is well described by the series assigned to the other stations: the resulting correlation is well centred around the theoretical values of matrix \mathbf{R}_M for the 10 realizations shown in the figure.

Fig. 3.5 shows the final correlation obtained after the maximum likelihood selection, evaluated for 10 different realizations. The figure compares the correlation of the initial auxiliary set ξ with the correlation of $\tilde{\zeta}$ at the end of the procedure. As expected, series of the process ξ are uncorrelated, since chosen to satisfy each single site $P_i(A)$ disregarding the other sites. The desired correlation is imposed by arranging the available series in accordance to the theoretical spatial correlation of the rainy stations at any given “epoch”. The result is the same set of series, properly arranged to show the correct spatial correlation (triangles in figure) among the concurrent rainy stations.

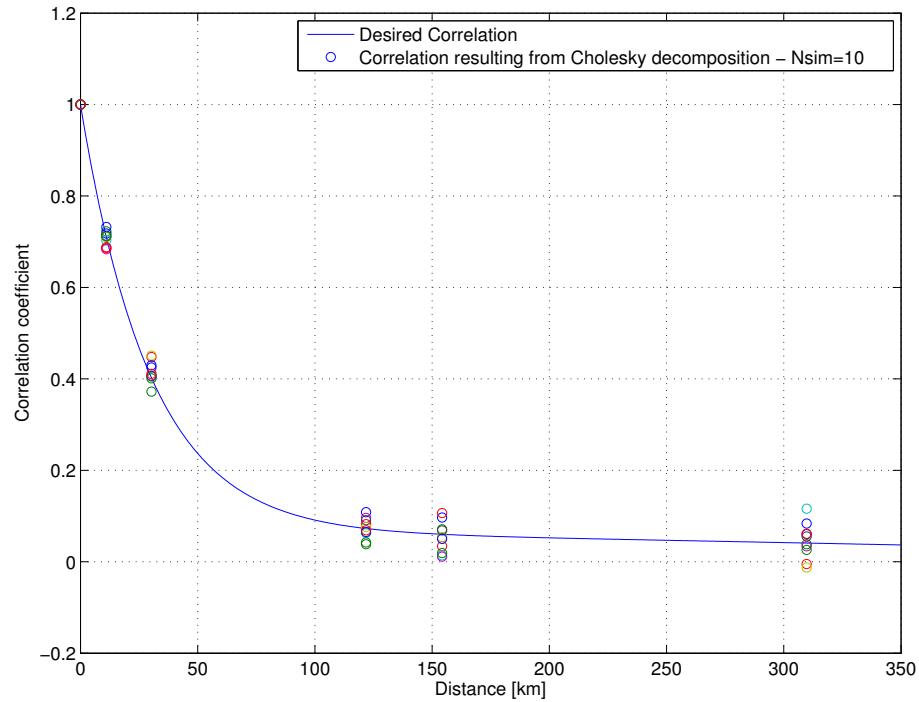


Figure 3.4: Spatial correlation of rain attenuation compared with the desired reference correlation. Example of 6 stations at different distances, 10 realizations.

The performance of the whole algorithm, considering the different processes involved, are discussed in the next Section. The whole algorithm is summarized in the Appendix.

3.7 Numerical simulations

Numerical simulations presented in this section have the purpose of testing the described algorithm considering the following aspects: the accuracy of the attenuation statistics resulting from the generated series compared to reference curves, the adaptability to different test sites and the spatial/temporal correlation of instantaneous rain attenuation for multiple sites time series generation. The reference curves of

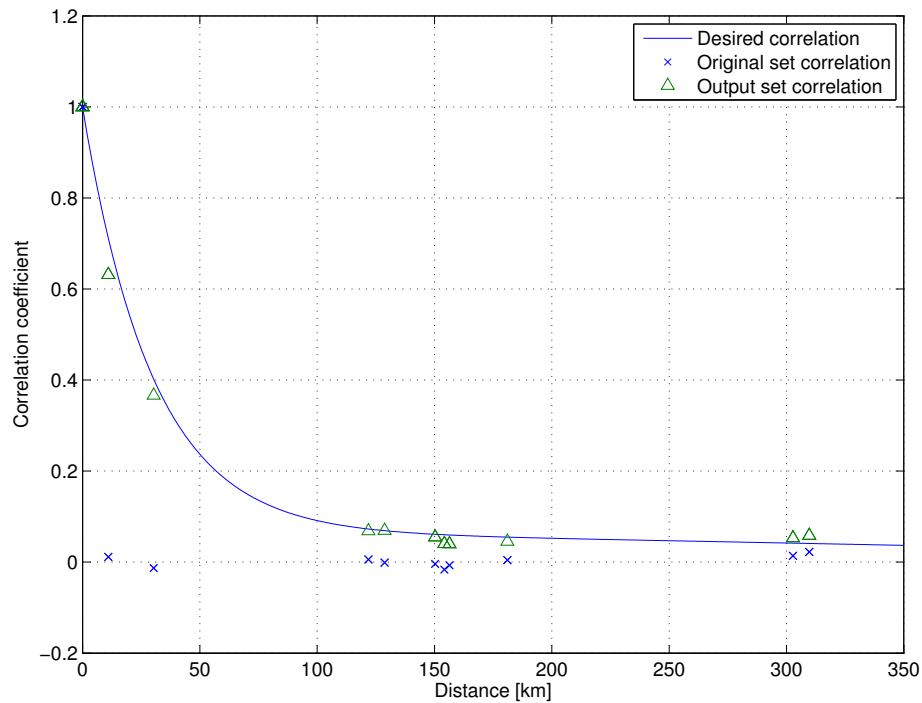


Figure 3.5: Spatial correlation of rain attenuation: result of the Cholesky decomposition and Maximum Likelihood (ML) selection of series. Uncorrelated series (blue crosses) and correlated series after ML selection (green triangles).

rain attenuation statistics are derived according to current available models [31, 38], the multiple sites rain correlation is tested against the results presented in [2]. The simulation parameters are described in the following paragraphs.

3.7.1 Rain attenuation statistics: adaptability to different geographical sites

The described model generates a series of measurements which belong to the attenuation statistic curve of the desired simulated Earth to satellite link. Firstly, the accuracy in reproducing the long-term attenuation statistics is assessed for different

simulation durations, in order to validate the series selection algorithm.

Considering the objective of simulating one year of rain/no rain conditions for a set of stations, the number of rain attenuation series depends on the “epoch” duration and on the year probability of rain attenuation P_0 for the selected site. Considering a fixed “epoch” duration of 30 minutes, one year is equivalent to 17520 “epochs”, among those a number between 400 and 1000, depending on the site P_0 , are rainy series. In the following figures is shown the attenuation distribution obtained by the generated time series, considering 1 simulated year and the average of 3, 5 and 10 years. The reference curve is the long-term attenuation distribution obtained by the SC-Excell model [32] for the specific location and satellite link. A satellite link at 20 GHz is considered, with a geostationary satellite positioned at longitude 16° East. The model was tested for three location in Europe reflecting different climatological conditions: Spino d’Adda, Italy (high P_0) Fig. 3.6, Prague, Czech Republic (cold climate and rainy, high P_0) Fig. 3.7 and Madrid, Spain (warm climate and dry, low P_0) Fig. 3.8.

Figures show the attenuation distribution obtained by the model generated series for a different number of simulated year. The generated series well approximate the long-term rain attenuation distribution by averaging a small number of simulated years. For all the sites, the starting point of the curves is determined by the station P_0 . The initial part of the attenuation distribution is very well resolved by a single realization down to a probability between $5 \cdot 10^{-2}\%$ (Spino d’Adda, worst case) and $10^{-2}\%$ (Prague, best case). It is a significant result considering that the quantile $10^{-2}\%$ is equivalent to 1 hour/year and that the curve is obtained using a number of rainy time series reflecting the site P_0 . A stable statistic at probability $10^{-3}\%$ (6 minutes/year) is gained by averaging 5 to 10 single years, which is reasonable for a long-term statistic. Must also be considered that the attenuation distribution of a single year of measurements exhibits a significant deviation from the long-term

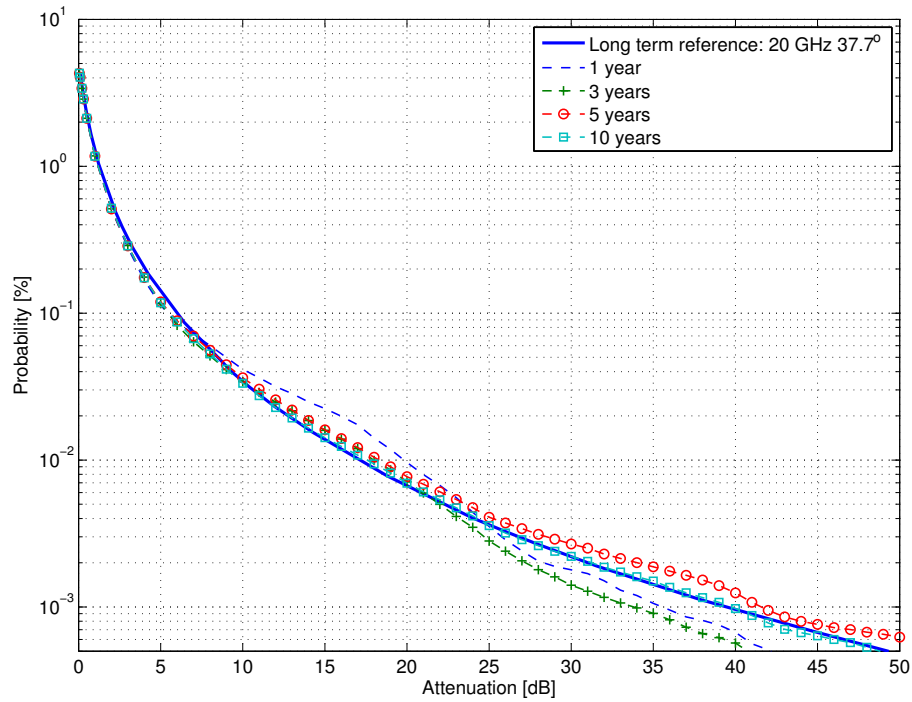


Figure 3.6: Complementary Cumulative Distribution Function (CCDF) of rain attenuation at Spino d'Adda (Lat. 45.4 N, Lon. 9.5 E), Italy. Link at 20 GHz. Reference attenuation from physical model SC-ExCell (solid line) compared with time series of a single year realization and the average of multiple years. Higher stability at low probability values is achieved by averaging multiple years. A good stability down to probability of $10^{-2}\%$ is already obtained averaging 3 years, stability at $10^{-3}\%$ (6 min/year) is gained by averaging 5 to 10 single years.

reference, as shown in [56] for the data collected as Spino d'Adda. From a qualitative point of view, the single year distribution obtained by the proposed model appears reasonable and within the standard deviation of single years measurements [56].

Concerning the climatological characteristics of the chosen locations, the accuracy in reproducing the different attenuation distributions is significant: the algorithm properly select the attenuation series and their occurrence to reproduce the desired attenuation statistic. These results represent a sensible improvement of the conver-

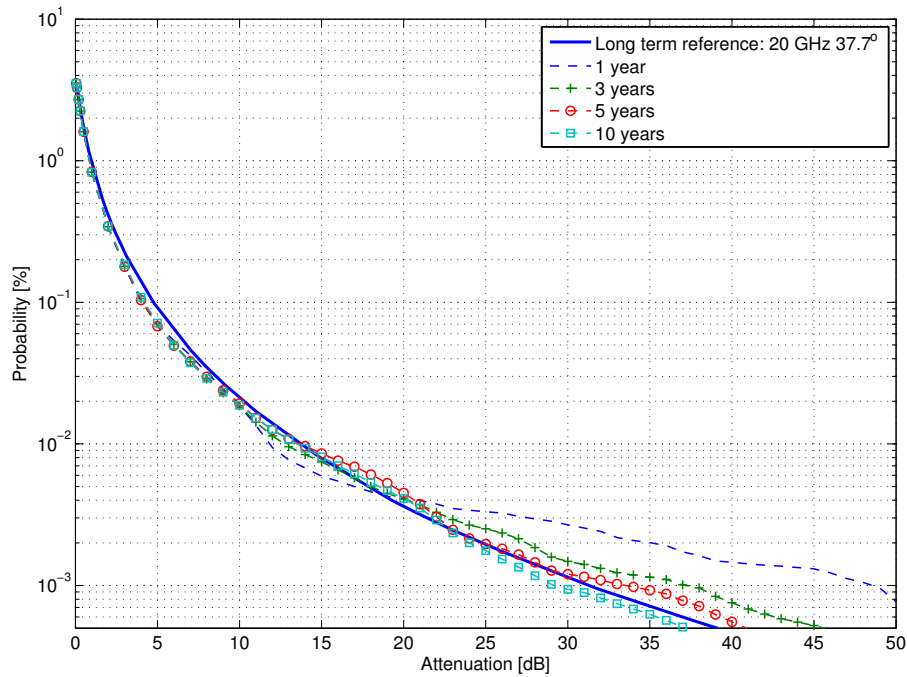


Figure 3.7: Complementary Cumulative Distribution Function (CCDF) of rain attenuation at Prague (Lat. 50.1 N, Lon. 14.3 E), Czech Republic. Link at 20 GHz. Reference attenuation from physical model SC-ExCell (solid line) compared with a single year realization and the average of multiple years time series. The selected series well reproduce the attenuation statistic also in this case by averaging a small number of year realizations. A good stability down to probability of $10^{-3}\%$ (6 min/year) is already obtained averaging 3 simulated years.

gence issues of a single site statistic described in [55].

The joint attenuation distribution among many sites is discussed in the next paragraph, with special attention to the resulting correlation of both rain events and attenuation among the different stations.

3.7.2 Site Diversity results

We considered a set of dual-site diversity test cases, in order to compare the joint exceedance probabilities obtained by the proposed model with the site diversity joint

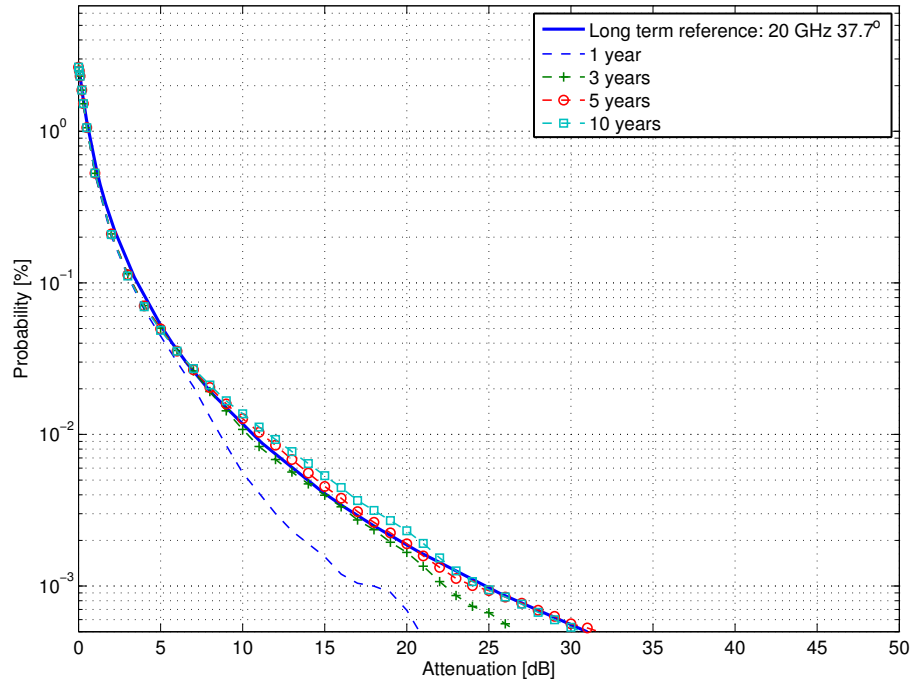


Figure 3.8: Complementary Cumulative Distribution Function (CCDF) of rain attenuation at Madrid (Lat. 40.4 N, Lon. 3.7 W), Spain. Link at 20 GHz. Reference attenuation from physical model SC-ExCell (solid line) compared with single year time series realization and the average of multiple years time series. In this case the station exhibits lower attenuation values in the statistical distribution. Also in this case, the curve is well represented by the selected “epochs” statistic. A good stability down to the probability of $10^{-3}\%$ (6 min/year) is obtained averaging 5 simulated years.

probabilities obtained by the ITU-R statistical model [24]. Stations are located at different distances (6, 19, 22 and 40 km) to test different levels of resulting rain attenuation correlation coefficient (respectively 0.82, 0.55, 0.51, 0.3 according to 3.16). Results are the average of 3 simulated years.

Figure 3.9 shows the results for a dual-site in Chibolton (U.K.). The distance between the simulated stations is 6 km, leading to a high degree of attenuation correlation (0.82) among the simulated time series. The agreement between the joint

statistics of the TS model and the ITU-R model curves is satisfactory. The oscillating behaviour of the joint curve for very low probabilities ($10^{-3}\%$) is due to the lack of joint attenuation values in the generated series.

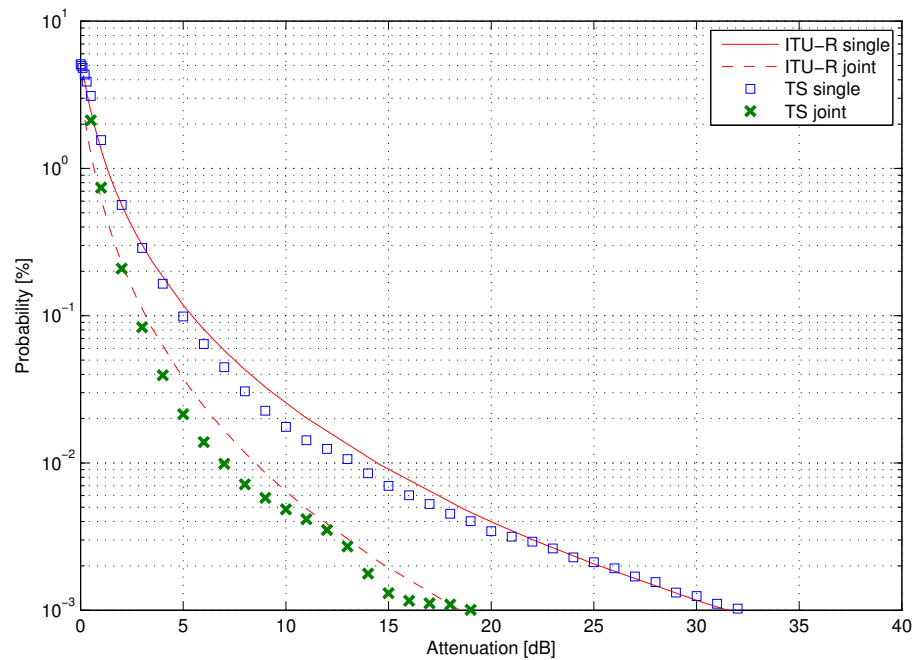


Figure 3.9: Dual-diversity results in Chibolton, U. K. Distance 6 km

Fig. 3.10 and Fig. 3.11 show the same curves for dual-sites at 19 and 22 km. In this cases the correlation coefficient of rain attenuation is close to 0.5, results show a good agreement between the TS model and the ITU-R statistical reference. The single site exceedance probability is well represented, the joint probability well follows the reference curve almost down to $10^{-3}\%$, except from the case of Toulouse, where the statistic obtained by the chosen TS exhibits a little lack of joint attenuation higher than 10 dB due to the chosen set of series.

The last case is a dual-diversity in Prague, with distance 40 km corresponding to a correlation coefficient $\rho = 0.3$ 3.16. The rain attenuation joint exceedance prob-

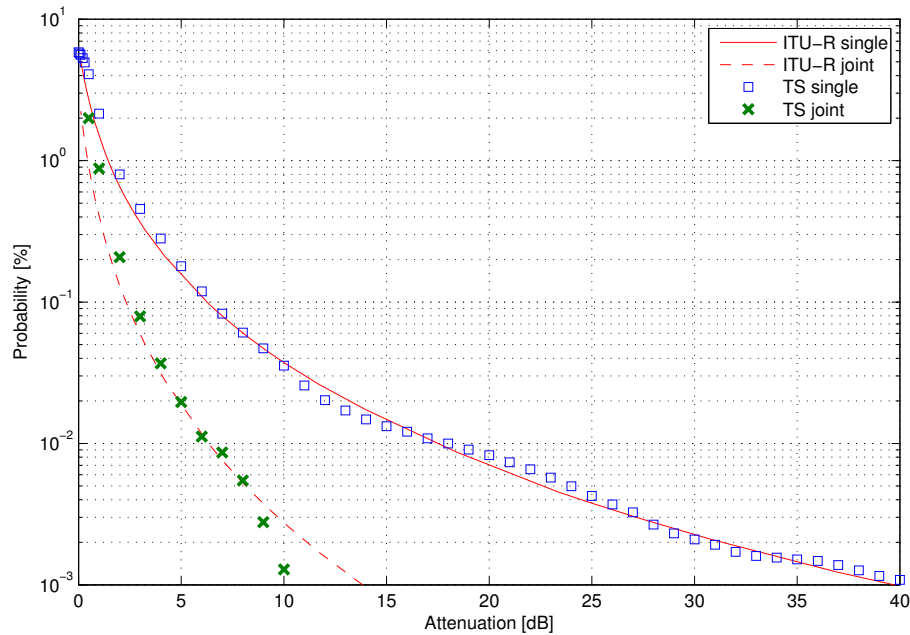


Figure 3.10: Dual-diversity results in Toulouse, France. Distance 19 km

ability is shown in Fig. 3.12. Statistics obtained by the generated time series exhibit a good accuracy with the reference ITU-R model.

The obtained results exhibit a good statistical behaviour imposed by the series correlation, considering that series are not generated “ex-novo” but are “chunks” of recorded rain events suitably arranged in time and space according to their average attenuation values. Since the original purpose of the model is to describe concurrent rain attenuation conditions for many users over a large area, in order to prove the validity of the imposed spatial dependence the χ index is introduced and discussed in the next paragraph.

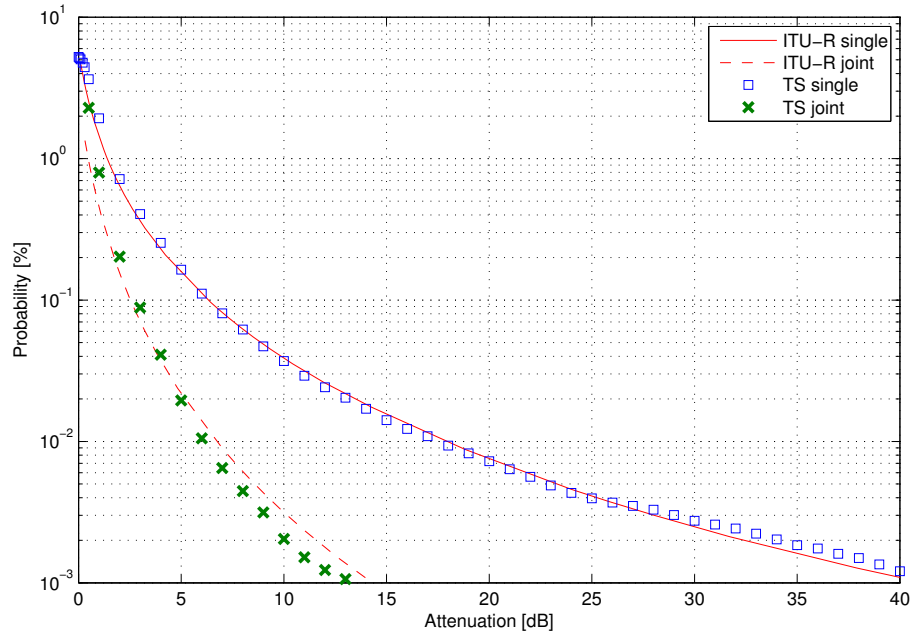


Figure 3.11: Dual-diversity results in Spino d’Adda, Italy. Distance 22 km

3.7.3 Rain decorrelation: Statistical Dependence Index χ

The rain attenuation spatial correlation is tested over one simulated year of time series obtained with the methodology previously explained. Results are provided in terms of the statistical dependence index χ described below and are assessed against an independent data set derived from the NIMROD C-band radar network.

The rainfall correlation between two sites can be assessed by means of a customary correlation coefficient but also through the statistical dependence index χ [54], defined in terms of rain intensity as:

$$\chi = \frac{P(r_1 > \tilde{r}, r_2 > \tilde{r})}{P(r_1 > \tilde{r})P(r_2 > \tilde{r})} = \frac{N(r_1 > \tilde{r}, r_2 > \tilde{r})}{N(r_1 > \tilde{r})N(r_2 > \tilde{r})} N_{tot}, \quad (3.21)$$

where

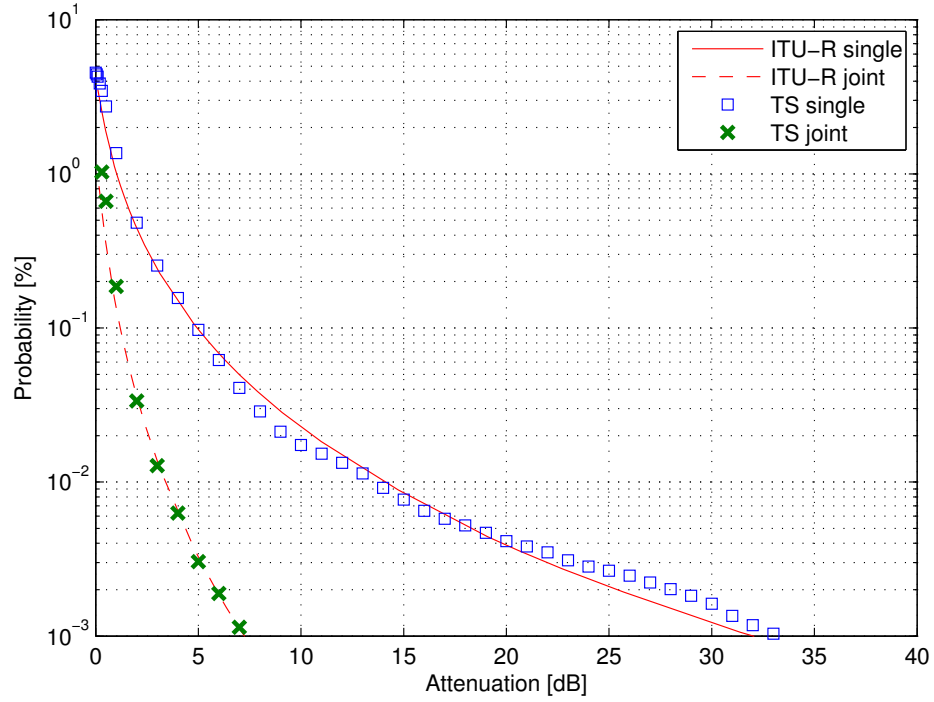


Figure 3.12: Dual-diversity results in Prague, Czech Republic. Distance 40 km

- r_1 and r_2 indicate the rain intensity in site 1 and 2,
- $N(r_1 > \tilde{r}, r_2 > \tilde{r})$ is the total number of samples for which both r_1 and r_2 exceed the rain threshold \tilde{r} ,
- $N(r_1 > \tilde{r})$ is the total number of samples for which r_1 exceeds \tilde{r} regardless of r_2 ,
- $N(r_2 > \tilde{r})$ is the total number of samples for which r_2 exceeds \tilde{r} regardless of r_1 ,
- N_{tot} is the total number of samples

The advantages originating from the use of the statistical dependence index are [54]:

- It is less noisy of the correlation coefficient which depends on all rain rate values, also on those typically less accurately measurable (e.g. samples of rain intensity equal to few mm/h .),
- It allows to directly calculate the two-site joint statistics from the knowledge of the marginal statistics of the two sites.

For these reasons, the χ index appears to be the most adequate indicator of the spatial decorrelation of rain. In order to evaluate the χ index, the model time series are converted from attenuation measurements into rain intensity referring to the well-known relation [38]:

$$A_L = kR^\alpha L \quad [dB], \quad (3.22)$$

where A_L is the attenuation in dB for a link of length L , R is the rain intensity in mm/h, coefficients α, k are obtained from ITU-R Recommendation [21]. Considering the frequency of transmission of 20 GHz, the α parameter is very close to 1, thus Eq. 3.22 can be easily inverted with minimum loss of accuracy. The rain intensity values are obtained by generating time series of rain attenuation taking into account a link elevation of 90° , resulting in a link length L equal to the actual rain height.

Referring to Eq. 3.21, the threshold \tilde{r} to evaluate the statistical index χ is chosen to obtain statistically meaningful result, consequently a good trade-off between measurements stability and rain variability. The threshold selected is $\tilde{r} = 3$ mm/h, which allows to compare the χ results with the average χ obtained by processing the NIMROD network data in [2]. The NIMROD network is an extensive independent weather radar dataset managed by the UK Meteorological Office. It was shown in [2] that the average χ evaluated from the NIMROD network well represents the behaviour

of other measurements previously obtained in Europe in two distinct experimental campaigns [64, 65]. The good agreement between the three data types is a hint of the fact that the rainfall average spatial correlation tends to be similar throughout Europe. For these reasons, the average χ computed from the NIMROD network in [2] is chosen as reference result for rain decorrelation over the simulated area. Details of the NIMROD radar network and the data processing to obtain the statistical dependence index used as reference can be found in [66].

The following figures show the χ index, as function of distance, evaluated from the time series of rain attenuation generated accordingly to the methodology previously discussed.

The test area to evaluate the rain decorrelation is a spot of $250 \text{ km} \times 250$ centred around the reference station of Spino d'Adda, Italy. A number of $N = 500$ stations are randomly displaced in the area. The time duration of a single realization is one simulated year, composed by “epochs” of rain attenuation and no rain (attenuation equal to zero) .

Fig. 3.13 shows the χ index obtained by simulations compared with the reference average trend obtained by NIMROD data. Results are the average of 10 independent realizations of one simulated year. The statistical dependence χ is evaluated for the N stations considering 8 secondary stations at different distances among the N simulated. For graphical clarity only the subset of stations is represented. Referring to Eq. 3.21, the two colors plotted (circles and crosses) represent two different primary stations among the possible tested; this is to prove that the mutual correlation among all the stations is well imposed and not biased by a specific reference station. The model results show a good agreement with the reference curve, with an expected difference in the starting point (χ index at distance 0 km), which depends only on the probability of having rain rate larger than the threshold \tilde{r} for the single

site: $P_3 = P(r > 3)$.

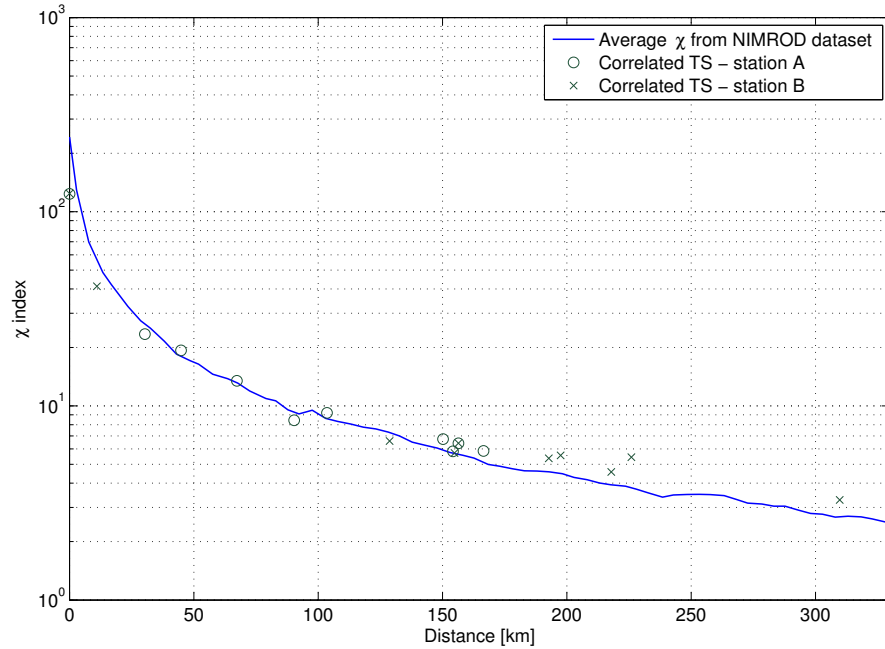


Figure 3.13: χ index obtained from the proposed model compared to the average χ index obtained by the NIMROD network. Simulation of 1 year (17520 epochs of 30 minutes, 910 rainy epochs), average of 10 different realizations. Two stations (circles and crosses) are selected as primary for the evaluation of the χ index to show the correct mutual correlation of rain events.

Fig. 3.14 shows the effect of the conditioned process previously discussed in Sec. 3.6.3. Circles in the figure correspond to the χ index evaluated from the correlated time series of rain attenuation, after the conditioned process. Red dots in the figure correspond instead to the χ index evaluated from series generated only by the conditioning process, with no correlation of attenuation imposed. The curves are normalized to the same P_3 of rain intensity. Consequently the starting point of simulated results is equal to 1 and for comparison purposes also the reference curve was scaled by the same value P_3 . The effect of the conditioned process, responsible of the spatial attenuation correlation, is evident at small and large distances: at distances

up to 50 km, the rain attenuation correlation is significant (please see Fig. 3.5) and the difference between the two simulated χ is more evident. It appears clear that the conditioned process well arrange the single site attenuation series in order to achieve the correct spatial correlation of rain attenuation. It is also interesting to note that, for distances between 50 and 200 km, there is no significant difference between the two processes. In other words, given a set of time series representing the long-term attenuation distribution of a number of sites, for those distances the only important process is the one that generates correlated rainy times over the stations (i.e. the conditioning process), disregarding the spatial correlation of rain attenuation. Moreover, for distances greater than 250 km, the effect of the conditioned process becomes again important, resulting in a better decorrelation of rain attenuation compared to the results of the conditioning process only. This figure shows that the process explained in Sec. 3.6.3 well impose the desired correlation of rain attenuation and, consequently, of rain intensity.

Moreover, that the statistical dependence index takes into account both the rain distribution over the area (concurrent rainy/not rainy times) and the rain attenuation, which are the two independent processes considered in the proposed model. The χ index shows that the model framework works properly, especially the combination of the two independent processes which assign rainy times and the rain attenuation time series.

3.7.4 Fade duration statistics

Finally, we discuss fade duration statistics to prove that the generated series are reliable in terms of attenuation fades intervals. Fades duration statistics are of concern for the evaluation of parameters associated with the risk of failure of a variety of

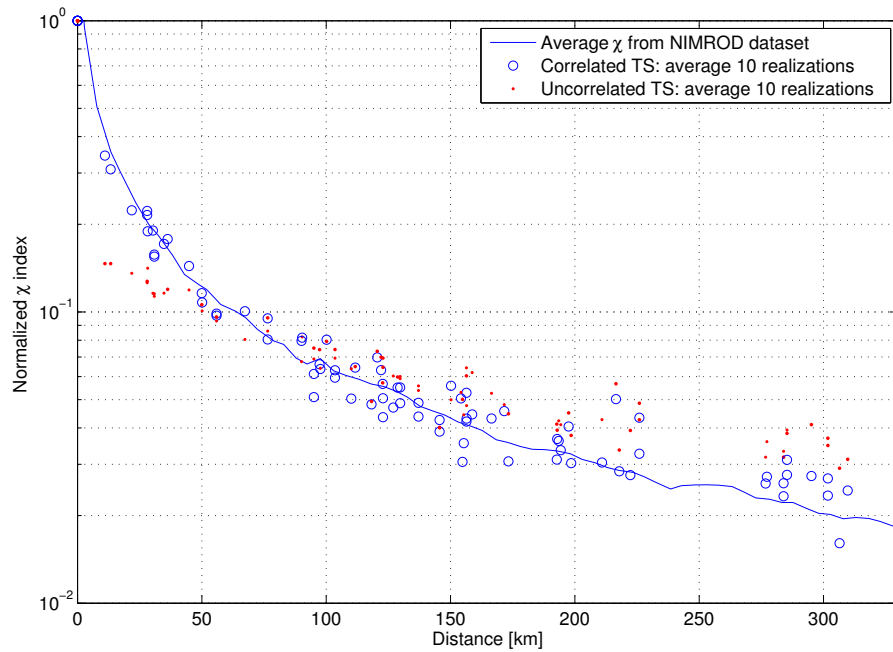


Figure 3.14: χ index obtained from the proposed model compared to the average χ index obtained by the NIMROD network. The χ index obtained from the conditioning process (red dots) is compared with the χ index resulting from the complete model (circles). The effect of the conditioned process, which imposes rain attenuation correlation, is evident for small distances (up to 50 km) where the impact of rain attenuation correlation is higher. It is also interesting the more accurate decorrelation achieved for large distances: the result of the two processes of the model better represent the expected rain decorrelation than the single conditioning process.

telecommunication systems. Fade duration is defined as the time interval between two crossings above the same attenuation threshold. In the context of availability criteria, of particular interest is the distinction between fades of shorter or longer duration than 10 s. Knowledge of the distribution of fade duration as function of fade depth is also a prerequisite for the application of risk concepts in the provision of telecommunication services [67].

Fade duration statistics are defined by two different distribution functions [67]:

- $Prob(d > D|a > A)$, the probability of occurrence of fades duration d longer than D (s), given that the attenuation a is greater than A (dB). This probability can be estimated from the ratio of the number of fades of duration longer than D to the total number of fades observed, given that the threshold A is exceeded;
- $F(d > D|a > A)$, the cumulative exceedance probability, or equivalently, the total fraction (between 0 and 1) of fade time due to fades of duration d longer than D (s), given that the attenuation a is greater than a (dB). This probability can be estimated from the ratio of the total fading time due to fades of duration longer than D given that the threshold A is exceeded, to the total exceedance time of threshold.

The latter statistics has been considered to test the proposed model. Fade duration statistics are evaluated from the obtained time series according to:

$$F(A|D) = \frac{N_S(D)}{N_{TOT}} \quad (3.23)$$

where $N_S(D)$ is the total time the attenuation A (dB) is exceeded composed of intervals longer than D (s) and N_{TOT} the total time the attenuation A is exceeded. The ITU-R model for fades duration [67] is taken as reference in terms of prediction accuracy. The ITU-R model [67] is expected to be valid for durations longer than 1 s and requires the following parameters:

- f : frequency (GHz): 10 – 50 GHz;
- φ : elevation angle (degrees): 5 – 60°
- A : attenuation threshold (dB)

Table 3.3: List of the DBSG3 considered experiments

Name	Country	Lat. [deg]	Lon. [deg]	Alt. [m]	Duration [dd]	Freq. [GHz]	Elev. [deg.]
Ottawa	CAN	45.34	284.11	81	362.74	20.19	27.32
Chibolton	UK	51.13	358.57	89	365	20.7	28
Sparsholt	UK	51.08	358.61	119	365	20.7	28
Dundee	UK	56.45	357.02	49	365	20.7	23.29

The proposed model was tested against a set of experimental data, results have been compared with the predicted statistics of the ITU-R model for the same experiments. Measured statistics of fade duration are obtained from the DBSG3 database [37], a set of 9 experimental statistics for 4 different sites, listed in Tab. 3.3, have been selected. The experiments were chosen based on the availability of statistical data at the frequencies close to 20 GHz.

Time series of rain attenuation for the considered links were generated by the proposed model. Statistics were obtained for different duration (60 120 180 300 600 900 1200 1500 1800 2400 s) and for different attenuation thresholds (3 5 10 15 20 25 dB). The statistics obtained by the time series and the ITU-R model are compared with those of the experimental data, the overall results are presented in terms of average error and RMSE error of the figure of merit $\varepsilon(D, A)$ [68]:

$$\varepsilon(D, A) = \ln \left(\frac{100\% - F_p(D|A)}{100\% - F_m(D|A)} \right) \quad (3.24)$$

Tab. 3.4 shows the overall error obtained by averaging over all the attenuation values and thresholds, for all the stations considered. The proposed model exhibits a mean error and RMSE very similar to the ITU-R statistical prediction, proving that fades duration statistics obtained from the correlated series are reliable.

Model	Mean error	RMS error
ITU-R	-0.45	0.66
TS	-0.48	0.69

Table 3.4: Fade Durations Test Results

3.8 Conclusions

This chapter describes a model to generate time series of rain attenuation values (1 sample/s) for multiple receiving stations in a large geographical area by adapting a single set of experimental rain attenuation measurements. The reference rain attenuation measurements are obtained from a large database collected at Spino d’Adda, Italy, during ITALSAT propagation campaign (from 1994 to 2000). The task especially addressed in this work is to reproduce concurrent attenuation time series for a large number of stations with the desired rain statistics and correlation, both in terms of rain occurrence and rain attenuation.

The proposed model consists of two independent processes, one assigning the rainy time to the stations and the other assigning concurrent rain attenuation values for the identified “rainy” stations. A mathematical description based on a multidimensional Gaussian model allows to suit the measured values to the different locations, arranging the attenuation time series with the desired spatial correlation. The obtained time series are composed of basic periods of fixed length (1 hour in this case, which was found to be a good trade off between the correlation interval of events). The generated time series is composed of discrete periods either of real rain measurements or no rain intervals, with a time resolution equal to 1 sample/sec. An important advantage of the proposed model is that, within the basic period duration, the characteristics of the rain process are defined by the real measurements. The basic period duration defines the update timing of the model: at every period (“epoch”) rainy

stations are properly identified and series of rain attenuation measurements assigned. The temporal evolution of the rainy events is driven by an exponential correlation model and the spatial correlation of rain events and attenuation is correctly imposed.

The model has been tested on its ability to reproduce the long-term rain statistics of single stations with different climatological characteristics and for different simulation durations. In addition to the first-order statistics of rain attenuation, the model is able to reproduce the spatial distribution of rain attenuation: concurrent rain conditions over multiple sites have been verified by the evaluation of joint attenuation CDF and by measuring the decorrelation index of rain among the stations (χ index). From a temporal point of view, a validation in terms of fade duration statistics is proposed.

Results obtained by simulations are compared with current models, showing a good agreement and proving the model validity. Especially, long-term statistics are well reproduced for a wide range of probability levels with a limited number of simulated year-long time series. In terms of space diversity, joint attenuation CDF are reproduced with good accuracy compared to ITU-R statistical model. Looking at multiple sites, the rain correlation among multiple stations well matches independent reference measurements, validating the mutual correlation processes implemented. Finally, fade duration statistics show the same accuracy of current statistical model for a set of radio links with available measurements. In conclusion, the model here proposed is suitable for simulating accurate concurrent rain attenuation conditions for multiple sites, taking into consideration the spatial correlation of rain events and attenuation.

The knowledge of concurrent attenuation values over a large geographical area can be used to verify the effectiveness of proper Fade Mitigation Techniques FMTs for current and new SatCom systems. In this perspective, the joint use of the gen-

erated time series with other FMT, such as Adaptive Modulation and Coding and Reconfigurable Antenna [69] is introduced and discussed in the next Chapters.

Chapter 4

Fade Mitigation Techniques

4.1 Introduction to Fade Mitigation Techniques for satellite transmissions

A serious challenge for satellite communications systems operating in Ka or higher bands is represented by the atmospheric propagation impairments. In fact, at those frequencies the additional attenuation due to meteorological phenomena is so high that it may not be practically feasible to reach the required link availability and system capacity by classical means.

As discussed in Chapter 2, the major impairment for medium/high availability systems is certainly represented by rain attenuation but also gaseous absorption and scintillation may have significant effects. It is worth noting that rain attenuation affects a specific location only for a small percentage of time in a year.

The simplest solution for counteracting the atmospheric impairments is to over-size the system elements. This approach is not always feasible and is, however, uneconomical. In fact, even when it is feasible, the system over sizing represent a waste of resources for the most of the time, i.e. when the satellite link is in clear sky conditions, because it can not exploited to obtain additional benefits. For these reasons, in the course of the years, several Fade Mitigation Techniques (FMTs) have been devised to cope with the atmospheric phenomena.

The focus is on a Geostationary Earth Orbit (GEO) multibeam broadband satellite system for interactive applications, where users are not mobile. The forward link is defined as the communications link between the ground GateWay station (GW) and User Terminal (UT). The GW sends through the satellite transponder one carrier per beam to the multiple receivers located within each satellite beam and, therefore, a certain division of the power allocation and Time Division Multiple Access (TDMA) is necessary. The beam frequency plan is designed according to a specific frequency reuse scheme.

After a brief introduction to those techniques which appear more interesting for the Multimedia Fixed SatCom scenario, two of them, the On-Board Dynamic Power Allocation (OBDPA) and Adaptive Coding and Modulation (ACM), are discussed in more details. Their joint use to support higher system capacity is proposed.

4.2 Review of most important Fade Mitigation Techniques

Several FMTs strategies have been devised in the course of years to make easier the migration towards higher frequency band in satellite telecommunication systems. Below is a shortlist of the effective techniques in counteracting atmospheric fading in the forward link of a Multimedia Fixed SatCom scenario:

- Site Diversity
- Power Control
- On-Board Dynamic Power Allocation OBDPA
- Adaptive Coding and Modulation ACM

The Site Diversity technique, Power Control and other FMTs not applicable to the proposed scenario are briefly introduced in the following, while separate sections are dedicated to the OBDPA and ACM.

4.2.1 Site Diversity

Site diversity is a helpful technique that can greatly reduce the additional link margins necessary to overcome the atmospheric impairments for systems operating in Ka band or higher frequencies. This technique relies on the use of two or more distant earth stations transmitting and/or receiving the same information for increasing the overall link availability. In fact the presence of more than one earth station allows to receive or transmit the signal using the earth station that is currently experiencing the best atmospheric propagation conditions.

From system point of view, the effect of site diversity on the link budget is equivalent to a reduction of the margins needed for achieving the required link availability. This reduction, generally expressed by the diversity improvement factor, directly depends on the decorrelation of the atmospheric fading on the ground station sites. According to propagation measurements, full spatial decorrelation of fading requires distances between sites which approaches 1000 km. However, distances in the order of 15 to 30 km may be enough to reduce fading correlation to acceptable levels. An example of the possible link margin reduction is shown in Chapter 3, Sec. 3.7.2, where the joint rain attenuation distribution CCDF is shown for a single site diversity (two stations) at distances ranging between few km and 40 km.

Site diversity introduces additional system level complexity due to the need to coordinating between the two cooperating ground stations. The coordination between the two ground stations can be less or more critical depending if Receiving (Rx)-only

or Transmitting (Tx) site diversity is employed. Rx-only site diversity can avoid most of the coordination problem. The rationale for such an approach is that on-board power is more costly than ground stations power. Thus up-link attenuation may be compensated by over sizing the ground station available power margin. Down-link attenuation will instead be counteracted by the site diversity. In this case, the demodulated streams of both ground stations will be sent to a suitable access controller which will select one of them basing on their quality. Tx site diversity is, instead, more complex to implement due to the need of a mechanism for the synchronization of the transmission chain of the ground stations working in diversity mode. The critical point of the coordination is also dependent on whether it is allowed to have a short interruption of the service when the transmission is switched from one ground station to the other one.

Due to the need of two cooperating ground stations located at several km from each other, this technique is not generally economically viable for counteracting fading at user terminals because of the required low cost of such terminals. In fact, the saving in terminal cost deriving from a possible smaller sizing of the terminal (in terms of EIRP and G/T) made possible by site diversity is completely offset by the cost of the communication infrastructure required for supporting the site- diversity operation. Viceversa, for the larger gateway stations used in a star network scenario or for professional ground stations (e.g. for internet data trunking), the station sizing saving may be economically significant to justify the additional cost of the site-diversity infrastructure.

At this regard it shall also be mentioned that site diversity is seen as particularly suited for the GWs in the Broadcast and Multimedia Fixed SatCom scenarios where the availability of the feeder-link shall be much higher than that of user-link. The concept of *smart* diversity implies a network of interconnected GWs. If one GW

becomes unavailable due to rain fade (or for any other reason), traffic is switched to other ones within the network. The system capacity in this scenario depends on the number of active feeder links at the same time, which depend on their joint attenuation conditions. This is a very recent topic under investigation [70, 71].

4.2.2 Power Control

Power control is among the most important and most used FMTs. It is in fact quite simple to implement but also very effective, making it a worth solution for counteracting atmospheric fading. Power control is typically performed at the ground GW stations to control up-link power (UPC). Down- link power control instead is currently not generally utilized due to constraints in on-board power management.

This technique relies on an extra power margin available at the ground station, which is exploited when fades are detected in the earth-to-satellite link. Different implementation techniques are available according to the kind of traffic to be supported and the control loop to be used. For the Forward-Link of both Broadcast and Multimedia Fixed SatCom scenarios, up-link power control could be operated according to several strategies:

- Open loop PC utilizing the estimation of up-link fading based on the Signal to Noise Ratio (SNR) measurement of a beacon signal. This approach is affected by the frequency scaling error, being the beacon frequency likely in a different frequency band;
- Open loop PC utilizing the up-link fading estimation based on the radiometer measurement of the sky temperature increase. This technique has the disadvantage that radiometer calibration is difficult and the equipment costs are high. The solution based on downlink beacon measurement is to be preferred.

- Closed loop PC based on on-board measurement of the received level. This measurement could be done indirectly through the status (gain) of the on-board amplifier employed to stabilize output power even in presence of strongly attenuated up-link signal. Such status could be inserted in the telemetry stream forwarded to ground. Inaccuracies may be present due to the gain instabilities of the transponder receiving chain and affect the returning information.

4.2.3 Other FMTs

Others FMT are available as possible solutions to counteract atmospheric attenuation in Earth-to-satellite links, but do not find application in the forward link of Multimedia Fixed SatCom scenario.

Angular diversity is generally used in mobile satellites/users scenarios or where a constellation of satellite is in place (Low Earth Orbit (LEO)). Time diversity it generally used in mobile communications. The application of time diversity for fixed UT, due to the rain de-correalion time, would lead to excessive delay in the transmissions. Frequency diversity is hardly employable due to the high required bandwidth and the costs of multi-frequency receivers. Data Rate Adaptation which foresee a variable symbol rate cannot be applied due to the fixed channel bandwidth.

Table 4.1 provides a summary of the possible FMTs considered for the proposed scenario. Major details on the applicability of the techniques here reported can be found in [2]. The rest of the Chapter is dedicated to a more detailed explanation of the OBDPA system and ACM transmission schemes.

FMT	Applicable	Notes
Site Diversity	Yes	It can effectively mitigate the fading in the up-link and increase the link availability
Uplink Power Control	Yes	Effective in up-link, control loop required
Angular Diversity	No	Not applicable. Generally used in mobile communications
Time diversity	No	Not applicable. Generally used in mobile communications
Frequency diversity	No	Hardly employable due to the high required bandwidth
On-Board Dynamic Power Allocation	Yes	It can effectively increase link availability and capacity
Adaptive Coding and Modulation	Yes	It can effectively increase link availability and capacity
Data Rate Adaptation	No	Not applicable since the channel bandwidth is fixed

Table 4.1: FMTs applicable to the forward-link of Multimedia Fixed SatCom scenario

4.3 The On-Board Dynamic Power Allocation System (Reconfigurable Antenna)

Among other, the OBDPA system is one of the most promising techniques to overcome the attenuation effects when there is strong precipitation affecting the satellite-earth link. The reconfigurable technique take advantage of the spatial and time decorrelation of the rainfall processes to reallocate dynamically in both time and space the system power margin among the users.

The OBDPA system accounts a multi-feed antenna which illuminate the service area with multiple beams. The power radiated by the feeds can dynamically modified in time according to the time variant attenuation conditions. This kind of antenna is applicable in both Broadcasting scenarios and Multimedia SatCom scenario, with dif-

ferent characteristics in terms of coverage of the service area and system performance evaluation [69, 72].

Propagation impairments such as signal attenuation and scintillation, if faced with the traditional satellite system design, would lead to an oversized antenna front-end. In fact, the classical approach to design satellite system is based on a climatological fixed-front end antenna design, aimed at coping with the worst-case fading occurrences all over the service area. Actually, due to the localized nature of the most of the meteorological phenomena such as rain, bad propagation conditions never occur simultaneously across the whole service area. It is in fact more frequent the case in which only a small fraction of the service area is affected by severe fading, as it can be experienced in the usual situation of localized meteorological fronts evolving in time. In Ka band (20 to 30 GHz), expected total attenuation may exceeds 6 dB and 10 dB respectively at probabilities $p = 1\%$ and $p = 0.1\%$ of the year time (reference ITU-R model [24] for a Earth-space slant path with elevation 37.7° , temperate areas).

Because of this characterization, a fixed front-end would need a significant power extra-budget to accomplish the required availability performance, which would be actually necessary only when predicted “bad” propagation conditions happen, leading to a waste of resources for most of the time. On the contrary, a reconfigurable antenna front-end could be better exploited, if able to spatially arrange power distribution according to the actual time-variant propagation needs. The power would be allocated only in the amount and in the area where it is really needed, thereby allowing a considerable economy in the management of the limited on-board available resources, targeting the same system availability.

In a reconfigurable antenna system the power available on board is dynamically allocated on the ports of a multibeam antenna by means of a Beam Forming Network (BFN), composed of Multi Port Amplifiers (MPAs). The radiation patter is in

essentially controlled by a set of excitation coefficients (as many as the antenna feeds) which ensure the required power at each port and which are related among each other by the MPA structure. To properly identify the optimum distribution of power flux on the ground and, accordingly, to select the proper set of excitation coefficients, the system needs to process current meteorological data for the service area.

The above system involves a great number of design aspects: technological devices design, meteorological data processing, system control operations. One of the key issues in the design of the front-end is its optimization on the basis of the fading distribution detected across the service area. The attenuation conditions for the service area are in turn predicted according to another key strategy based on the collection and appropriate processing of meteorological weather information, obtained from the ECMWF [73] predictions. Once the fading distribution is available from predictions, the radiation of the on-board power is reconfigured by a proper BFN, defined by components such as phase shifters and amplifiers. The BFN reconfiguration is carried out according to the outcome of an optimization procedure, driven by merit figures based on such fading predictions. For the Multimedia Fixed SatCom scenario, the link SNIR has been proposed as merit figure for the BFN optimization, since taking into account interference among co-channel beams is mandatory due to the adoption of frequency reuse schemes [74].

4.3.1 The service area model

As basic system configuration, a multibeam satellite system with N feeds is considered, which generates a set of spots with the arrangement represented in Fig. 4.1. The service area (Europe in this case) is divided into a regular grid of N_s subareas, called “pixels”. For each pixel its area dimension, latitude and longitude coordinates

are defined. The area is served by N beams, which are fed by an independent signal directed to the users located within the spot (different colors refer to the different allocated frequency bands, distributed among the spots in order to minimize inter-beam interference). Regardless to the number, position and shape of the beams we will make reference to a well defined transfer function relating the power injected in a beam-port to the power density incident on any point of the Earth served by the corresponding spot:

$$S_i = T_{i,j}P_j \quad (4.1)$$

which relates the power P_j (W) injected on the j^{th} beam port to the power flux S_i ($\frac{W}{m^2}$) incident on the i^{th} point on the Earth among the N_s ones chosen to sample the served region (as in Fig. 4.1). The T matrix describes the satellite system geometry, it is strictly dependent upon: the position of the satellite with respect to the service area, the multibeam directivity function and the geometrical distribution of the grid of ground receiver stations used to sample the service area. Therefore, each element of $T_{i,j}$ takes into account the antenna directivity function in the direction of the i^{th} point and its distance from the satellite. $T_{i,j}$ is defined once, considering the antenna characteristics, the satellite position and the grid of served users.

4.3.2 Antenna design

4.3.2.1 Multi Port Amplifiers

The most important aspect of the OBDPA system is to efficiently share the radiated power, reducing inter-beam interference and allowing high flexibility in the power allocation among antenna ports. The adaptive beamforming network is composed of N elements, one per each antenna feeds, clustered by a set of MPA devices. The MPA is a multi-input and multi-output system that is capable to amplify multiple

input signals at the same time by using shared amplifiers. The multiple input signals and outputs are amplified separately via different output ports to reduce any mutual interference.

The MPA scheme is a well known and consolidated technique to carry out power reconfiguration among spot beams. The technique has been implemented in the Japanese satellite WINDS for an experiment strictly related to power reconfiguration aimed to the compensation of Ka-band rain attenuation.

The general scheme of the antenna is shown in Fig. 4.3, where each beam is radiated by a single feed via distributed amplification and final composition of the different amplified contributions. The amplified contributions are collected by a High-Power BFN (HP-BFN) which has the goal to focus the whole power on the single feed in charge for radiating the current beam.

The classical layout of the HP-BFN is based on a set of MPA, composed by a number of hybrid couplers properly connected to each other. The basic assembly, named Butler-Like Matrix (BLM) because similar to Butler Matrix layout with the exception that phase shifters between successive layers of hybrid couplers are not present. Apart from the trivial BLM with 2 inputs and 2 outputs, i.e. a single hybrid coupler, the lowest level of BLM is the one with 4 inputs and 4 outputs, also called 4×4 ; it is shown in Fig. 4.2, where a number of 4 Hybrid couplers $3\text{dB}/90^\circ$ is recognized.

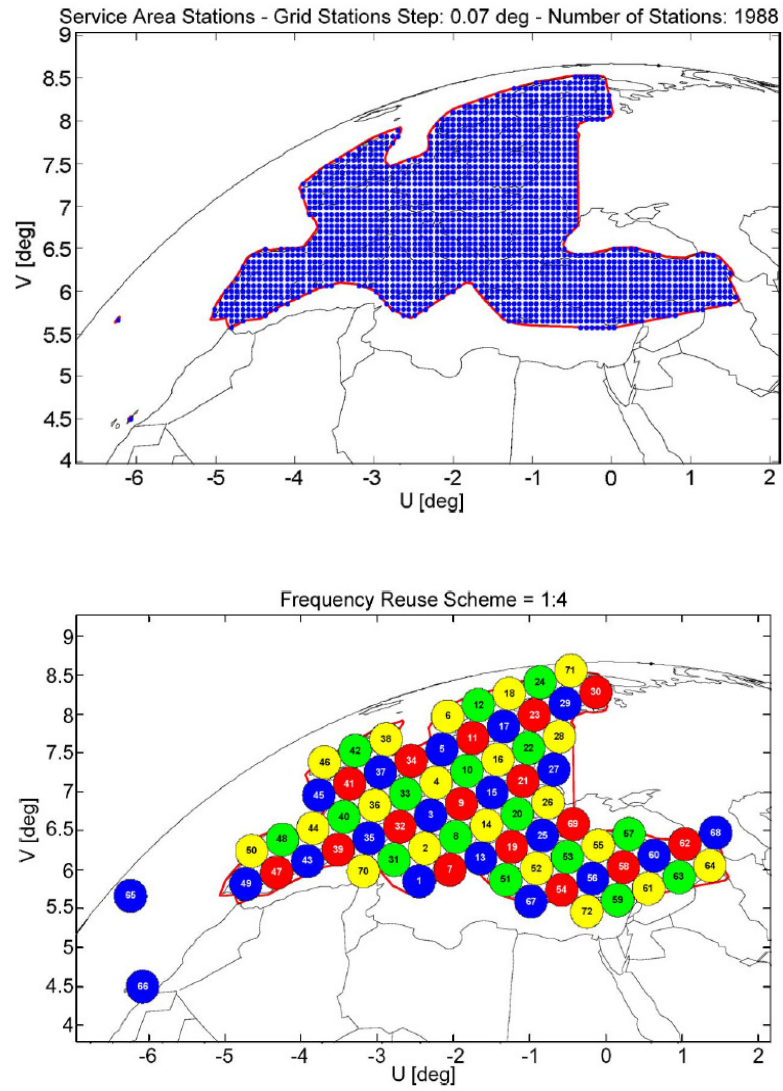


Figure 4.1: Coverage area over Europe: reference grid points and multibeam antenna scheme [2]

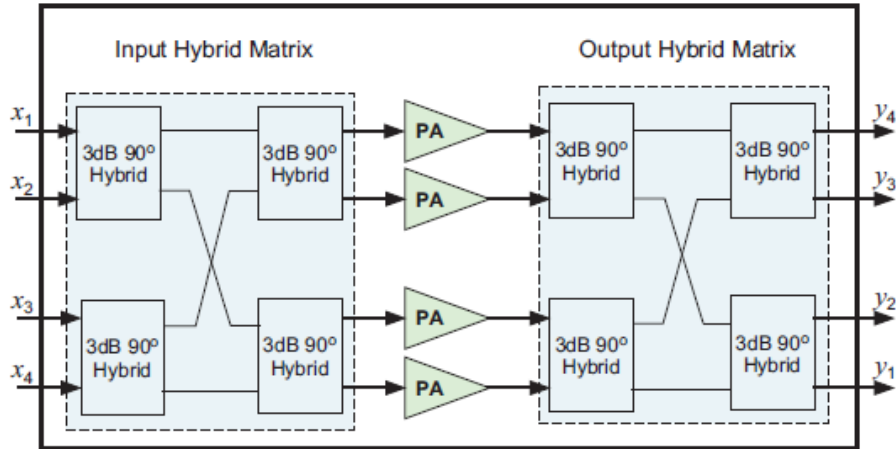


Figure 4.2: MPA general scheme

As a result, the available on board power is firstly equally divided among the MPAs and afterwards a set of coefficients assign the power to the 4 (or 8) ports that belong to the same MPA. Reconfiguration is actuated in MPA scheme by means of a variation of the carrier level among the different beams at the MPA input.

In order to best exploit the power allocation between the ports of an MPA, the weather condition detected inside the spots covered by the MPA feeds should be not correlated. Consequently, in case there is high rain intensity over one spot linked to an MPA, the needed power could be subtracted to the same MPA remaining spots. As a consequence, the spot assignment to each MPA assumes the maximum geographical distance between elements of the same MPA, trying to ensure the highest dissimilar weather conditions among the feeds. In this way, the co-frequency interference among the same MPA beams is also minimized.

4.3.2.2 Antenna Front-End

The front-end architecture for the TLC antenna under analysis is based on fixed amplifiers it is divided into 2 main sections:

- the *reconfiguration control section* is composed by a set of beam amplifiers and it is responsible for supplying the amplification section with optimum amplitude distribution among beams according to the selected criterion;
- the *amplification section* is composed of MPAs of 4×4 order.

From a reconfiguration point of view, the optimum beam amplitude distribution is obtained by a single amplitude-only optimization including all the beams [74].

4.3.3 Antenna Optimization

4.3.3.1 Dynamic Optimization

In Fig. 4.4 the main steps of the adaptive antenna control are reported. The core of the reconfigurable system is constituted by the *dynamic optimization* of the excitation coefficients of the antenna BFN coefficients. This process is devoted to the identification of the optimum power flux distribution over the service area to reduce the slant path attenuation effect. The optimization procedure is called dynamic since it updates the flux profile each time new meteorological information for the service area are available. The first step is the elaboration of the meteorological input information to estimate the atmospheric attenuation over the service area. The meteorological reference database is composed of numerical weather predictions supplied by the ECMWF [73]. It provides vertical profiles of different atmospheric parameters (humidity, temperature, etc.) and surface integrated values (cumulated rain, etc.) 4 times a day with 6-hours intervals, with a spatial resolution of $1.125^\circ \times 1.125^\circ$. The

elaboration purpose is to match the input meteo data to the grid of the service area, generating a *snapshot* of meteorological conditions. The snapshot is simply an instantaneous description (6-hours duration) which collects the parameters of “clear sky” attenuation (clouds, water vapor and oxygen) and rain attenuation contributions, for each pixel in the grid. Rain, if present in the pixel, is described in statistical terms by a spatial distribution of rain. Once the service area has been set and the elaboration completed, each i^{th} pixel of the grid is modeled by a curve, which provides the information of the fraction of the pixel area subject to attenuation higher than a specific threshold. These functions, different if we consider a rainy or not rainy pixels, are calculated for each specific snapshot.

Regarding rain attenuation, two meteorological parameters provided by ECMWF predictions allow to estimate the rain distribution over the pixel area: the cumulated rain amount m_t in the observation period and the fraction of convective rain β . A spatial rain modelling is needed to derive the rain distribution over the pixel area and over the 6-hours period, starting from the two above integral information. A rain field generator [66] is used to calculate the rain rate CCDF in space, while the SC-ExCell [32] model derives the rain attenuation distribution. The obtained distribution identifies the fractional area of a given pixel where a certain attenuation value is exceeded.

The goal of the OBDPA system is the compensation of the degradation due to atmospheric attenuation (clear-sky and rain) by means of a flexible reallocation of available power resources over the set of beams. The previous meteorological elaboration provides a map of attenuation distribution over the service area which should be overcome by radiated power flux, in order to improve the user receiving conditions.

The optimization algorithm aims to achieve the power distribution which best

cope with the described attenuation conditions. The definition of the appropriate optimization strategy actually consists in the definition of a suitable merit figure which is mostly representative of the global system performance. Considering the Multimedia Fixed SatCom scenario, the real performance of a multibeam antenna operated in frequency-reuse is the received carrier power at any ground user weighted by the noise power and interference [74]. The pixel SNIR for the considered service area is defined as:

$$\text{SNIR}_i = \frac{1}{\frac{1}{\text{SNR}(w_j, a_i)} + \frac{1}{\text{SIR}(w_j, w_{k \neq j})}} \quad (4.2)$$

where the dependency with the pixel attenuation a_i and the interference of co-frequency beams is shown. For a given power available on board, the flux $S_{i,\text{dB}}$ incident on the generic pixel i^{th} is given by:

$$S_{i,\text{dB}} = P_{j,\text{dB}} + T_{ij,\text{dB}} - A_{i,p,\text{dB}} \quad \frac{\text{dBW}}{\text{m}^2} \quad (4.3)$$

in which $P_{j,\text{dB}}$ is the power injected in the port j , expressed in dBW, $A_{i,p,\text{dB}}$ is the total atmospheric attenuation in dB affecting the i^{th} pixel link at a certain probability value p , $T_{ij,\text{dB}}$ is the transfer matrix element defined in Eq. 4.1. The SNIR definition in Eq. 4.2 takes into account two components: the SNR dependent on the radiated power and attenuation on the link; the Signal to Interference Ratio (SIR) dependent on the interference due to co-frequency beams and defined by the antenna design and power configuration. Therefore, once the attenuation distribution on the ground pixels has been evaluated, it can be provided as input to the dynamic optimization routines.

The optimization algorithm of the power flux distribution aims at maximizing the SNIR in the most critical point of the service area, given a total radiated power.

The choice of the worst pixel in the area as reference for the optimization at each iteration is not the only solution possible. It is chosen since it provides to the optimizer the information of the worst pixel in the service area, information which could be lost by considering the average SNIR. By acting on the worst pixel, the optimization ensures to increase the area SNIR low level. The dynamic optimization process is performed at every new meteorological snapshot, available on a regular time frame (every 6 hours if ECMWF data are considered). The routine implemented consist in a standard gradient descent optimization algorithm. The optimizer takes as input also the information regarding the antenna architecture (number of feeds, available power, and MPA order). The optimization works on the N transmission coefficients, responsible for the radiated power in each beam. Because of the interference term, the SNIR of any considered pixel is dependent not only the power radiated in the beam to which the pixel belongs, but also on the power radiated on the co-frequency beams around, according to the specific frequency reuse scheme in place (Fig. 4.1). At every iteration, a new map of interference among the beams is obtained and a new iteration is started. The optimization procedure ends when the relative gain of new iterations is no more significant. The dynamic optimization results in a set of optimal coefficients w_{opt} which drive the power radiated in each of the N beam. Finally, the OBDPA system performances are evaluated by a proper post-processing.

Must be underlined that the optimization procedure based on the worst pixel SNIR is not the most sophisticated approach to the problem. Different solutions can be envisaged, especially by adding side constraints the optimization process should satisfy. The proposed solution represents the first approach to the problem and it is definitely open to future development and refining [69].

4.3.3.2 Climatological optimization: optimal fixed transmission coefficients

A different kind of optimization for the multibeam antenna is the one that takes into account long-term prediction of attenuation distribution to derive the optimal set of fixed transmission coefficients. In this case no dynamic optimization procedure is present: the radiated power is fixed in time but not uniform over the service area, according to the attenuation statistics. This solution is adopted in traditional satellite antennas exploiting fixed front end. In such cases, the optimization of the antenna pattern is performed once before the launch of the satellite.

This optimization algorithm, called *climatological optimization*, is the same as the dynamic case except for the service area attenuation map, which is based on long-term statistics. For a fixed probability value, the climatological optimization generates a set of antenna coefficients which minimizes the on-board power requirements to account for free-space losses and climatological attenuation.

The optimization takes into account the cumulative distribution functions CDF of attenuation $P(A)$ for each pixel of the service area. The needed $P(A)$ can be derived by means of one of the many attenuation prediction methods available in the scientific literature, some of those like ITU-R [24] or SC-ExCell [32] have been presented in Chapter 2. From the knowledge of the $P(A)$, the climatological optimization takes into account the total atmospheric attenuation (clear sky and rain attenuation) which is exceeded in each pixel of the service area for a percentage of annual time (usually are considered 0.1%, 0.5% and 1.0%).

Fig. 4.5 and Fig. 4.6 show an example of the climatological attenuation predicted by the ITU-R model P.618-10, respectively at a probability levels 0.1% and 0.2% over the service area in Fig. 4.1. The optimization procedure, explained in [69],

aims at the minimum system power margin to serve the worst point in the service area.

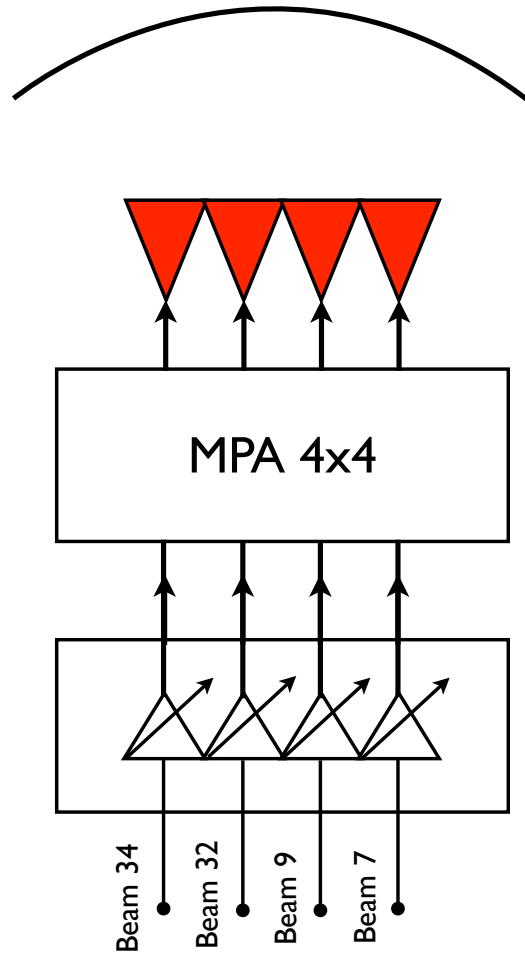


Figure 4.3: Antenna scheme. 1 feed per beam, MPA scheme 4×4 . The 4 feeds relative to red beams 32,34,7,9 in the service area are shown.

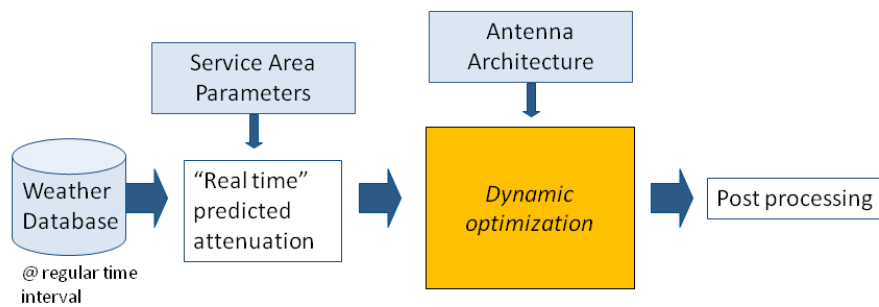


Figure 4.4: Representation of the dynamic optimization process

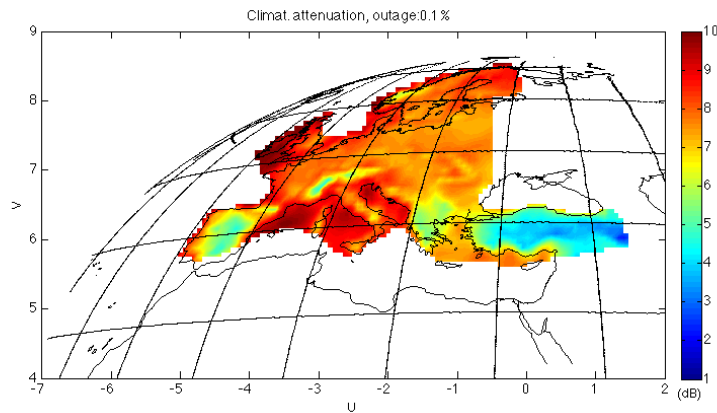


Figure 4.5: Climatological attenuation exceeded for 0.1% of annual time. Service area, model ITU-R P.618-10

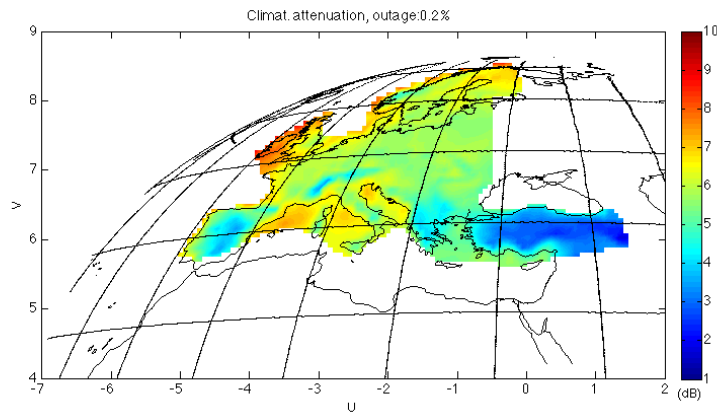


Figure 4.6: Climatological attenuation exceeded for 0.2% of annual time. Service area, model ITU-R P.618-10

The climatological optimization, which results in fixed feed excitation coefficients, is usually considered to assess the advantage of the dynamic optimization process previously explained. In the following, the antenna optimized based on the long-term attenuation statistics is referred simply as *fixed* antenna.

4.4 Adaptive Coding and Modulation for Multibeam satellite systems

ACM is a sophisticated form of data rate control in which information rate is adapted by changing modulation and coding rate while maintaining a constant symbol rate on the channel.

The aim of this technique is to dynamically select, based on the current channel quality, the best transmission ModCod pair to maximize the spectral efficiency satisfying the required BER or FER. According to this principle, when the link is in clear sky conditions the transmitting ground station employs ModCods with high spectral efficiency requiring high SNIR to be decoded, aiming to achieve the highest available information rate. Conversely, when the link is affected by heavy rain, transmitting ground station employs ModCods with low spectral efficiency, but requiring low SNIR, aiming to preserve the link availability. The main advantages of ACM with respect to conventional approaches are:

- *Increase of system throughput:* generally, in SatCom systems operating in Ka or higher bands, high additional link margins are considered in the system design phase in order to guarantee the required link availability. These margins would be wasted for the most of the time, i.e. when the ground station is in clear sky conditions. Those margins can be exploited by ACM to sustain a more efficient transmission by adopting more complex ModCods, in order to increase the system throughput;
- *Increase of link availability:* the employment of low spectral efficiency ModCods requiring low SNIR allows to increase the link availability. Concerning this aspect, it is important to note that when low spectral efficiency ModCods are

employed, the data rate is reduced and it may be not adequate to support the provided service. In fact, the minimum data rate required by the service determines the minimum spectral efficiency and, therefore, the higher bound for the link availability achievable with ACM.

The ModCod selection procedure requires the transmission ground station to estimate, before transmitting, the quality of the radio link in terms of the end user SNIR. The most straight-forward solution to this issue envisages a measurement of the link quality by means of pilot symbols sequences, which are reported back to the transmitting station. In realistic conditions, the SNIR measurements cannot be directly employed in the selection procedure because they might resemble outdated channel conditions. The problem of channel estimation and accurate channel prediction and information represents a significant issue in the implementation of this technique.

Given the purpose of this work to assess the joint use of OBDPA and ACM, the procedure followed by the user to inform the transmitting station, as well as the format of this information, are not discussed in here. The assumptions made hereinafter are that the transmission stations keep track of channel variations occurring to user's terminals, and that the physical layer configuration used in the forward transmission to each individual user are known both at the transmitting and receiving sides. This is a common assumption for the assessment of the ACM transmission strategies, since it represents the theoretical case of application [75, 76]. More detail in the channel estimation procedure and feedback may be found in [77].

4.4.1 Adaptive Physical layer model

The Adaptive Physical Layer (APL) considered on the forward link is based on adapting both the coding rate and the modulation format ACM to best match the user SNIR, making the received data rate location and time dependent.

Referring to the previous antenna OBDPA system description, the received SNIR in the j^{th} beam is a stochastic process $\xi_{tot}^j(t, u, v)$ where t is the time and (u_j, v_j) are the variables modelling the receiver position, such that $(u_j, v_j) \in B_j$, with B_j the j^{th} satellite beam. The approach chosen to describe adaptive transmission system performance follows the one proposed in [75, 76].

A TDMA system is considered. The generic q^{th} frame is addressing a subset of users over the coverage region, whose SNIR at reception time shall allow correct decoding of the frame, with FER below the required threshold. The required minimum energy per bit over noise plus interference spectral density $E_b/N_t = E_b/(N_0 + I_0)$ at the user terminal depends on its physical layer configuration and will be identified with $\gamma_{req}(r, M)$, which depends on the modulation constellation M and the coding rate r . For the following system level analysis, the details of the framing structure are inessential and therefore are not described: for simplicity the index q^{th} for the frame dependency is omitted.

The user terminal SNIR, which represents the chip over noise plus interference spectral density E_s/N_t , for a generic user location $\bar{x} = (u_j, v_j)$ in the beam j of the coverage area is defined as [75]:

$$\frac{E_s}{N_t}(\bar{x}, a(\bar{x}), f_R, N_p) = \frac{C_{CS}(\bar{x})a(\bar{x})}{R_s\{N_0(a(\bar{x})) + I_0(\bar{x}, a(\bar{x}), f_R, N_p)\}} \quad (4.4)$$

where $C_{CS}(\bar{x})$ is the clear-sky received power at location \bar{x} , $0 < a(\bar{x}) \leq 1$ is the propagation fading power loss random variable. $N_0(a(\bar{x}))$ is the noise power spectral

density at the receiver input, which is also function of the fading attenuation due to the antenna noise temperature definition. $I_0(\bar{x}, a(\bar{x}), f_R, N_p)$ is the interference power spectral density at location \bar{x} , which accounts the power radiated over the co-frequency beam in the service area.

Recalling the relation between E_s/N_t and E_b/N_t :

$$\frac{E_s}{N_t} = \frac{E_b}{N_t} \cdot r \log_2 M \quad (4.5)$$

that holds for each modulation format of cardinality M and given the chip energy as $E_c = E_s/L_s$, it follows that for a certain location \bar{x} , affected at a given instant by the fading attenuation $a(\bar{x})$, the link closure condition is verified when

$$\frac{E_c}{N_t}(\bar{x}, a(\bar{x}), f_R, N_p) \geq \frac{r \log_2 M}{L_s} \gamma_{req}(r, M) \quad (4.6)$$

which defines the minimum SNIR to guarantee a correct transmission for a given modulation scheme. Parameters r, M define the coding rate and modulation constellation, the parameter L_s is related to the spreading factor and is greater than 1 if spreading occurs. The most suitable figure of merit to describe the transmission performances to user terminals in TDMA mode is their spectral efficiency η_u , which for correct decoding is defined as [75]:

$$\eta_u = \frac{R_b N_p}{R_c f_R} \quad (4.7)$$

where R_b, R_c are respectively the bit rate and chip rate, N_p is the number of polarizations used (if applicable) and f_R the frequency reuse scheme. Higher spectral efficiency results in higher data rate, thus the target of ACM technique is to select the physical layer parameter for maximizing the data rate at the generic location \bar{x}

conditioned to a given fading process realization $a(\bar{x})$. Since the bit rate is dependent on user location and propagation channel conditions, the optimization of the physical layer parameters is performed on each active link. The corresponding punctual optimized link efficiency conditioned to atmospheric fading a and the polarization and frequency reuse factors $(N_p; f_R)$ can be computed as [75]:

$$\eta_l(\bar{x}, a(\bar{x}), N_p, f_R) = \max_{r, M, L_s} \left\{ \frac{R_b N_p}{f_R R_c} \Big|_{\kappa \frac{E_c}{N_t}}(\bar{x}, a(\bar{x}), N_p, f_R) \geq \gamma_{req}(r, M) \right\} \quad (4.8)$$

where r , M and L_s are the adaptive physical layer parameters described in the previous section, $\kappa = \frac{L_s}{r \log_2 M}$. The spectral efficiency for the user u in the location \bar{x} can be calculated by considering the distribution of the fading random variable $a(\bar{x})$, either by averaging the link efficiency for a large number of independent realizations or by directly introducing the fading Probability Distribution Function (PDF). The average beam efficiency can be obtained by averaging over the all single user η_l :

$$\bar{\eta}_b(N_p, f_R) = \frac{1}{N_u} \sum_1^{N_u} \eta_l(\bar{x}_u, a(\bar{x}_u), N_p, f_R). \quad (4.9)$$

Eqs. (4.8) and (4.9) are function of the user SNIR, which has to be evaluated by expanding Eq. 4.4. In the DVB-S2 standard, a discrete set of ModCods are defined as function of the minimum SNIR to support them targeting a certain FER. The use of the ACM mode with highest spectral efficiency at any given value of SNIR leads to:

$$R_b(t, \bar{x}) = \begin{cases} 0 & \xi(t, \bar{x}) < \gamma_1 \\ \eta_m R & \gamma_1 \leq \xi(t, \bar{x}) < \gamma_{m+1} \\ \eta_M R & \xi(t, \bar{x}) > \gamma_M \end{cases} \quad (4.10)$$

where $\xi(t, \bar{x})$ is the time-location dependent user SNIR, η_m are the different spectral efficiencies and γ_m the SNIR thresholds defined in increasing order. This quantization of the continuous model in Eq. 4.6 results in a power/spectral efficiency granularity: the continuous variable $\xi(t, \bar{x})$ results in a discrete achievable spectral efficiency η_u .

Considering the standard DVB-S2 [78], the set of ModCods and their required ξ values are reported in Tab. 4.2.

Mod.	Inner code rate r	ξ (bits/s/Hz)	γ (dB)
QPSK	1/2	0.99	1.01
	3/5	1.19	2.23
	2/3	1.32	3.10
	3/4	1.49	4.04
	4/5	1.59	4.68
8PSK	5/6	1.66	5.18
	3/5	1.78	5.61
	2/3	1.98	6.72
16APSK	3/4	2.23	8.01
	2/3	2.64	9.07
	3/4	2.97	10.31
	4/5	3.17	11.14
32APSK	5/6	3.30	11.71
	3/4	3.60	12.66
	4/5	3.86	13.63
	5/6	4.03	14.28
	8/9	4.30	15.68
	9/10	4.35	16.04

Table 4.2: Table of ModCod, Spectral Efficiency (SE) and SNIR threshold according to the DVB-S2 standard. The SNIR thresholds are defined targeting a system packet error rate equal to 10^{-7}

In any case, the performance achievable with ACM are closely related to the temporal and spatial variation of the channel attenuation. For this reason, the fading process distribution $a(\bar{x})$ must be introduced.

In this section a methodology for evaluating the performance of ACM transmission scheme for a multibeam satellite system is briefly introduced. In ACM, the physical layer parameters are adjusted according to the actual user attenuation conditions (SNIR) to maximize the user spectral efficiency. The ACM scheme described is based on the DVB-S2 standard [78], which provides the minimum SNIR thresholds to activate the ModCods. The relationship between SNIR and spectral efficiency in Eq. allows to directly include the radiated beam power to the resulting user spectral efficiency. From this point of view, the proposed description appears the most suitable to address the advantage of ACM coupled with the OBDPA system

4.5 Conclusions

This Chapter presents the possible FMTs suitable for Multimedia Fixed SatCom services, with special attention focused on the OBDPA system and ACM. The ACM technique may take advantage of other FMTs like the proposed OBDPA. In fact the ACM performances closely depend on the available user SNIR, which is the merit figure maximized by the OBDPA optimization system.

The two methodologies aim respectively at providing the best SNIR user distribution on the coverage area (based on a specific optimization procedure) and to maximize the achievable user spectral efficiency, which is itself function of the user's SNIR, by optimizing the user transmission formats. It is clear that the two methodologies augment each other: jointly deployed, they will improve performance. Especially, the re-distribution of radiated power may increase the effectiveness of the ACM techniques. The following Chapter provides the result of the simulated use of the two techniques.

Chapter 5

Joint use of On-board Dynamic Power Allocation and ACM

5.1 Introduction

The aim of this section is to introduce a methodology to assess the effects of the joint use of OBDPA system and ACM, considering a multibeam satellite system for interactive multimedia broadband services in Ka band.

Moreover, the obtained SE by OBDPA is compared to the one obtained in static conditions, i.e. in case of antenna front-end optimized in order to counteract at its best the (long-term) climatological attenuation related to the selected system merit figures.

The spectral efficiency function would be suitable as merit function for optimization since it is directly linked to the achievable throughput, but unfortunately, due to its discontinuous nature, it is not worth using it as is in an optimization based on continuous functions. In order to achieve both accuracy and continuity the SNIR figure can be assumed as merit function since, in the end, an improved signal quality directly leads to an increased system capacity; an increase in the system throughput is instead achieved only if a higher efficiency ModCod is available and in use, i.e. its SNIR activation threshold is exceeded.

5.2 TLC antenna system and optimization algorithm

An hypothetical Telecommunication satellite system operating at 19.7 GHz is considered to service the Europe area. The TLC antenna system is constituted by a beamforming network of feeds driven by a set of Multi Port Amplifier (MPA). An optimization algorithm has been realized in order to implement an adaptive process. This optimizer modifies the excitation coefficients of the MPA devices, to achieve the best SNIR profile over the served region, according to the meteorological data. To estimate the weather condition over the service area and to evaluate the performances of the system, the overall region has been sampled with a grid of points, called also “pixels”, as it is shown in Fig. 5.1

The reconfigurable system makes use of meteorological data as the inputs of the optimization process which are provided by the ERA40 Database [15]. This database collects information about weather conditions of the service area, provided as a set climatological information available every 6 hours. Once processed, those information allow to predict the meteorological conditions on the service area for the next 6 hours period. Rain attenuation conditions are obtained by means of two mathematical models:

- Rain field generator: calculate the space-time CCDF of the rain rate, i.e. the fraction of points where the 1-min averaged rain rate exceeds given thresholds during the 6-hour ERA40 slot;
- ExCell model [32]: turns the CCDF of rain rate into the CCDF of slant-path attenuation by simulating the evolution of the precipitation cells

An optimization algorithm has been realized in order to implement an adaptive process to cope with the weather evolution. This optimizer modifies the excitation coefficients of the MPA devices, trying to achieve the best Signal-to-Noise plus Interference Ratio profile over the served region, according to the meteorological data. To estimate the weather condition over the service area and to evaluate the performances of the system, the overall region has been sampled with a grid of points, called also “pixels”, as it is shown in Fig. 5.1(a). The frequency reuse scheme of the antenna feeds has been depicted in Fig. 5.1(b). The geostationary satellite is located at Long. 33° E.

In the remaining part of the Chapter, one of the depicted beams in Fig. 5.1 will be analyzed as a test case. The excitation coefficient w_j for the beam j is function of all the other beam coefficient $w_{i \neq j}$. Hence, the analysis of a single beam includes the situation experienced over the whole service area.

The SNIR figure is chosen as Merit Function for the assessment of the reconfiguration performance of the RA coupled with ACM. The SNIR is defined as:

$$\text{SNIR} = \frac{C(u, v)}{N_0 R_s + I(u, v)} \quad (5.1)$$

where

$$C(u, v) = G_r(u, v) A_p(u, v) A_m(u, v) P_n G_{tn}(u, v) \quad (5.2)$$

is the carrier power actually received by the ground terminal, while

$$I(u, v) = G_r(u, v) A_p(u, v) A_m(u, v) \left[\sum_i P_i G_{ti}(u, v) \right] \quad (5.3)$$

is the aggregated co-channel interfering power actually received by the ground terminal. Specifically:

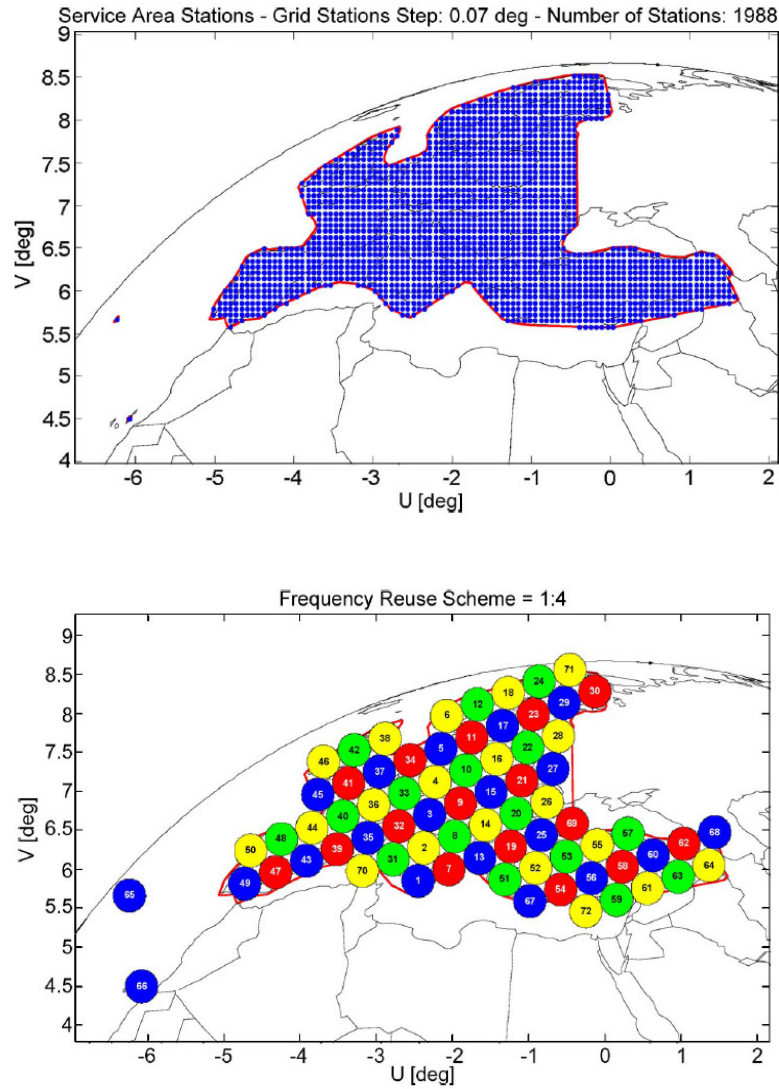


Figure 5.1: Service area Grid G6, satellite position $33^{\circ}E$. Pixels distribution (a) and beam division with frequency reuse scheme 4 (b) [2]

- P_n : Nominal power assigned to beam
- $G_{tn}(u, v)$: Gain of the beam in the ground terminal direction (u, v)
- $\sum_i P_i G_{ti}(u, v)$: Sum of EIRP values extended to co-channel beams
- P_i : Power assigned to the co-channel interfering beam i

- $G_{ti}(u, v)$: Gain of the co-channel interfering beam i in the ground terminal (u, v) direction
- $A_p(u, v) = \left(\frac{\lambda}{4\pi R(u, v)}\right)^2$: Free-space path attenuation in the ground terminal direction (u, v)
- $A_m(u, v)$: Tropospheric fading in the ground terminal (u, v) direction
- $G_r(u, v)$: Ground terminal antenna gain in the satellite direction
- N_0 : Received Noise power density
- R_s : Symbol Rate

The received noise power density is equal to:

$$N_0 = KT_s(u, v) \quad (5.4)$$

where

- $T_s(u, v) = T_a(u, v) + T_r$: System temperature
- $T_a(u, v) = T_m(1 - A_m(u, v))$: Receiving antenna temperature
- $T_m \approx 270$ K: from Recommendation ITU-R P.618-10 [24]
- $T_r = 290(10^{(L_t/10)} - 1) + T_{LNA}10^{(L_t/10)}$: Receiver temperature
- $L_t \approx 0.5$ dB: Transmission line loss (typical)
- $T_{LNA} \approx 150$ K: LNA temperature (typical)

5.2.1 Antenna optimization

The OBDPA optimization algorithm evaluates the optimal beam excitation coefficients to maximize a specific merit function, starting from the knowledge of the predicted attenuation of each pixel in the area. As detailed in Chapter 4, a dynamic optimization and climatological optimization are possible.

Concerning the dynamic optimization, the instantaneous weather information are elaborated by the system on a 6 hours basis (4 snapshots per day). Once the system receives the updated information concerning the weather conditions, a tropospheric attenuation value is calculated for each pixel of the service area. Subsequently the available power is reallocated, through the optimization of the excitation coefficients of the antenna. Such optimization modules consist of a standard gradient optimization algorithm aimed at maximizing the worst-case SNIR level computed on the selected grid of ground terminals.

The climatological optimization is based on the same gradient method and merit figure, with the only difference that the attenuation condition of the service area is derived by a long term attenuation distribution at probability 0.1%.

5.3 Free-space considerations

Firstly, the analysis of radiated power in free-space is beneficial to better understand the characteristics of the considered antenna system. The following graphs show the radiated power of the reconfigurable antenna system, the SNR distribution, SIR and SNIR distribution obtained over the service area by equal excitation coefficients. This analysis is proposed to underline the effect of SIR and SNR on the resulting SNIR across the service area. The proposed consideration led to the choice of a specific

beam in the centre of the service area, to simulate the users attenuation conditions and test the transmission techniques.

The system parameters are adopted for the simulation are reported in Tab. 5.1.

Parameter	Value
Frequency [GHz]	19.7
Number of feeds	72
Number of pixels	1988
MPA order	4x4
Transmission Line Loss (typical) [dB]	0.5
LNA Temperature (typical) [K]	150
Symbol rate [Mbaud]	45
Receiving station gain [dB]	42
Radiated Power [W]	2000

Table 5.1: OBDPA system and simulation parameters

The free-space propagation analysis is carried assuming a fixed antenna front-end, where the 72 feeds are powered by the same radiated power (1/72 of the total radiated power). Referring to the system plan reported in Fig. 5.1, the received power flux distribution on the Earth expressed in $\frac{\text{dBW}}{\text{m}^2}$ is shown in Fig. 5.2. Regarding the power flux radiated over the region, it could be relevant to note that also balancing the excitation coefficients of the radiating feeds, there are pixels which suffer more for the system design. As shown in Fig. 5.2, the ground stations which are located on the edge of the served region and on the border of the spots receive an impinging power that could be from 3 to 6 $\frac{\text{dBW}}{\text{m}^2}$ less than in the central part of the spots.

As previously shown in Eq. 5.1, there is an inverse dependence from sum of the SIR and the SNR with respect to the SNIR values. To appreciate the effects of both these parameters, an analysis has been conducted for both separately. The SIR represents the ratio between the desired received signal power and the interference

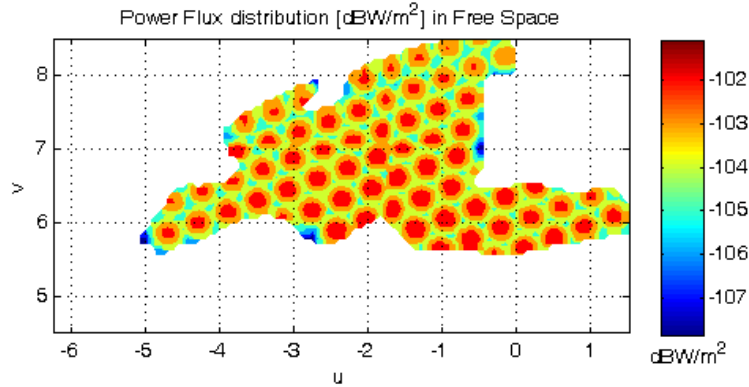


Figure 5.2: Power flux distribution in free-space conditions $\frac{\text{dBW}}{\text{m}^2}$ assuming uniform excitation coefficients.

effects due to the signal generated by different sources working at the same frequency. The spatial distribution of these values has been depicted in Fig. 5.3. It is relevant to note that the higher values of SIR are placed in the edge of the coverage area where the interference effects are noticeably reduced. The lower values of the distribution are located at the intersection of the adjacent spots in the center of the service area, with values approximately 15 dB less than the higher ones. From this distribution it is clear that the spots more affected by the interference term are those in the center of the service area.

The other elements which characterize the SNIR factor are expressed by the SNR profile. These factors depend from the useful signal power received by the antenna and the noise introduced by the receiver equipment and the atmospheric effects. The expected spatial distribution of SNR should show higher values in the center of the beams, with an expected limited decay on the borders of the service area. Fig. 5.4 confirms this description.

As can be seen in Fig. 5.4, the space distribution of these values in each pixel (end user terminal) maintains a strict dependence from the distance of that pixel from

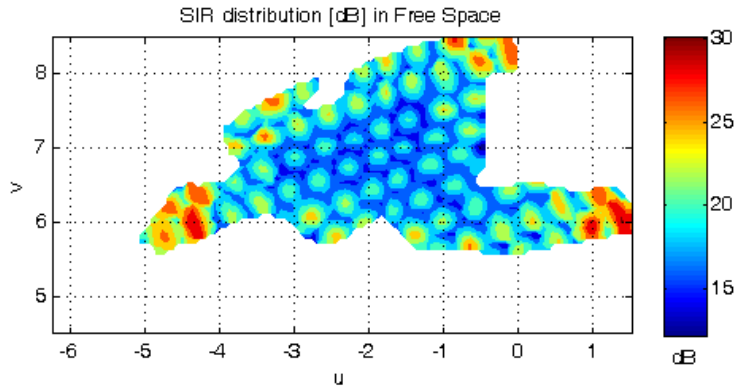


Figure 5.3: Spatial SIR distribution in free-space conditions assuming uniform excitation coefficients.

the centre of the relative spot. The profile values are almost constant over the served region, except for the boundary values that have even 6 dB minor than the higher ones. The SNIR profile obtained from the previous parameters has been represented in Fig. 5.5. This distribution, produced by means of a uniform set of excitation coefficients for the antenna feeds, represents the starting point for the optimization process in absence of any atmospheric effects. Finally, two distinct areas could be discerned: in the central part of the region are located the lower values of the profile (circa 16 dB), while there are pixels located on the edge of the coverage area that benefit in terms of SNIR values (around 20 dB). This discrepancy between these two areas depends from the preliminary system design and defines a system characteristic, which is important to take into account for the study of the user quality of service.

In conclusion for what concerns the free-space analysis, there are spots which a priori suffer more for the antenna configuration and the system definition, while others take advantage for the antenna design. The above distributions show that spots in the center of the service area are those subject to higher radiated power, but also higher interference due to the co-frequency beams, as clear from Fig. 5.5. This

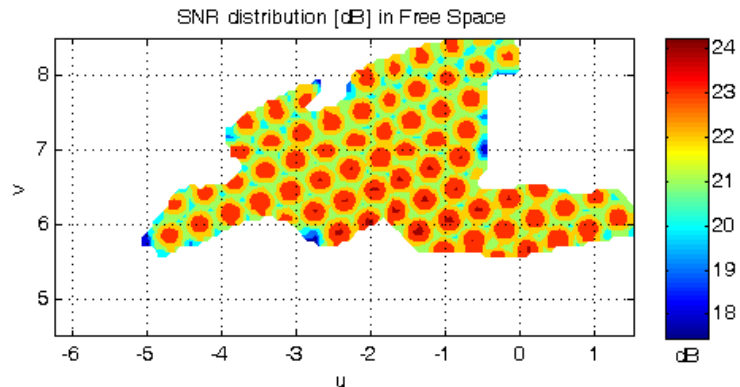


Figure 5.4: Spatial SNR distribution in free-space conditions assuming uniform excitation coefficients.

results in an overall lower SNIR values for users located in those spots. Consequently, a spot located in the center of the service area appears to be the most interesting to test the proposed transmission techniques, due to its lower SNIR characteristics.

5.4 Simulation setup

This section presents the results obtained by simulating the transmission with OBDPA antenna coupled with Constant Coding and Modulation (CCM) and ACM. The purpose of this section is to assess the performances of the different transmission schemes by proper merit figures, with particular interest regarding the benefits of OBDPA coupled with CCM transmission and ACM transmissions.

In the case of OBDPA system, the previous analysis shows that the SNIR distribution on one spot of the service area in Fig. 5.1 is influenced by:

- the multibeam antenna design;
- the radiated power on the specific spot (function of its predicted attenuation);

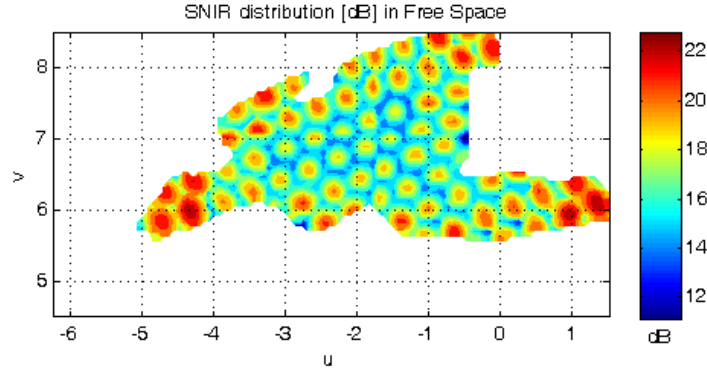


Figure 5.5: Spatial SNIR distribution in free-space conditions assuming uniform excitation coefficients.

- the radiated power by co-frequency beams (interference);
- the power distribution on the whole service area;

consequently, the radiated power on one single spot is dependent on the attenuation of the whole service area. The analysis of the radiated power over a single spot would indirectly take into account the overall area attenuation situation. In the following, a single spot of the service area has been selected to study the performances of the transmission schemes in terms of the final user SNIR distribution. Referring to the free-space analysis presented in Sec. 5.3, the spot number 32 in Fig. 5.1 is chosen for the following analysis.

In order to test the different transmission techniques, the user rain attenuation conditions have to be simulated referring to a consistent meteorological information, which drive the antenna coefficients optimization. The selected input meteorological database are the ECMWF 6-hours predictions of cumulated rain over the service area. Those information can be described as pictures (“snapshots”) of the predicted rain conditions valid for a 6-hours interval for a specific day. The selected “snapshots”

have to be processed to be applicable to the pixel reference grid in Fig. 5.1 by a specific pre-processing scheme.

A selection of test cases was performed among the meteorological data available for the year 2000, with the aim of representing different kind of rain conditions over the selected spot:

- snapshot 001228ss01 (Dec. 28, 2000): stratiform rain (low/moderate rain intensity), wide spread across the service area;
- snapshot 000715ss01 (July 15, 2000): convective rain (moderate/high rain intensity), multiple cells across the service area;

The following figures show the cumulated rain over the 6-hour period relatively to each of the above snapshot, the circle represents the selected beam where the attenuation user's conditions will be simulated.

By a proper pre-processing, the cumulated rain information is translated in the attenuation CCDF for each pixel of the service area [66]. The spot rain attenuation CCDF, necessary to simulate the user's rain attenuation time series by the model

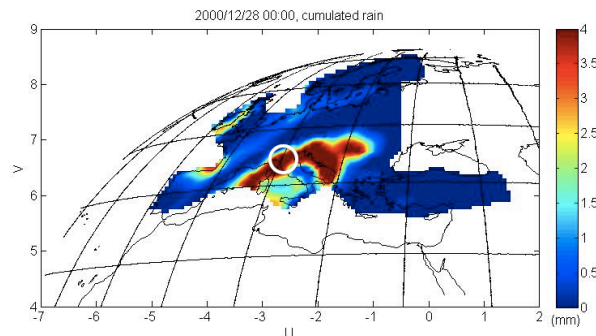


Figure 5.6: Snapshot 001228ss01: processed cumulated rain amount over the service area. Large stratiform rain area

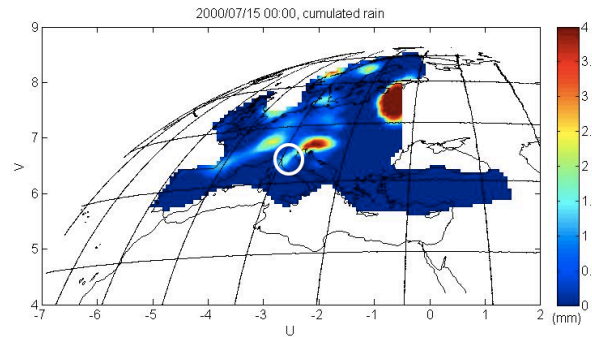


Figure 5.7: Snapshot 000715ss01: processed cumulated rain amount over the service area. Multiple convective rain cells

described in Chapter 3, is then derived by the average of the pixels attenuation CCDF belonging to the spot.

The resulting CCDF of rain attenuation, $P(A)$, for the spot area in the two cases is shown in Fig. 5.8. It represents the fraction of space and time of the spot area in Fig. 5.9 subject to attenuation values higher than the thresholds.

The different rainy conditions are clearly visible in Fig.5.8: wide stratiform rain (green curve), characterized by high covered area (starting point of the curve p_0), wide convective rain (red curve), characterized by highest attenuation values. The Log-Normal approximation of the rain attenuation $P(A)$ s is shown with circle lines. The approximation holds well down to 10^{-3} , which is set as the area probability limit. In terms of spatial resolution, given a typical spot dimension of $300 \text{ km} \times 300 \text{ km}$, the probability 10^{-3} is equivalent to a square of less than $10 \text{ km} \times 10 \text{ km}$.

Given the Log-Normal approximation, the model presented in Chapter 3 is applied to simulate the users' rain attenuation conditions inside the spot area.

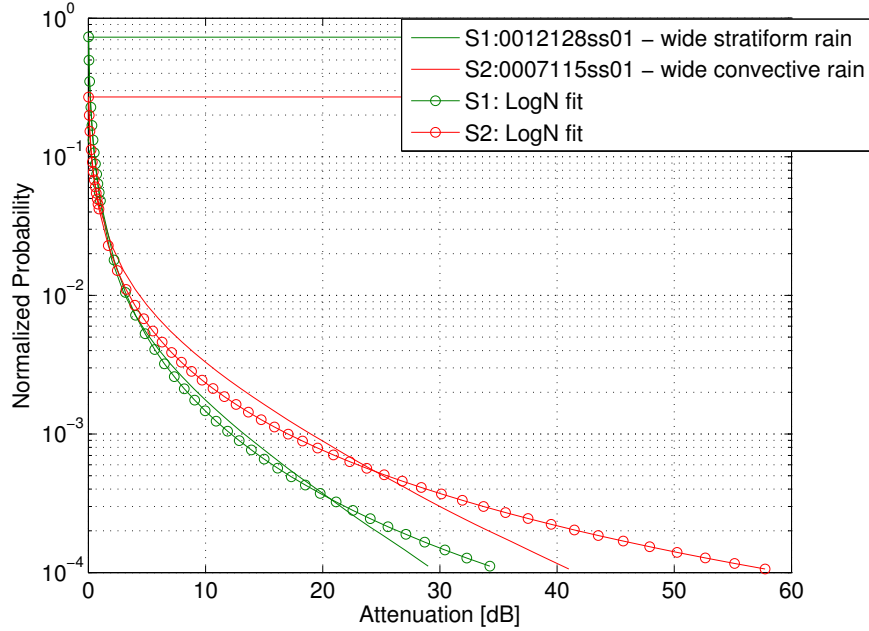


Figure 5.8: Rain attenuation $P(A)$ relative to different snapshot of meteorological prediction information. The attenuation distribution gives the spatiotemporal information (coverage area) relative to the selected spot. Two different rainy conditions are described: wide stratiform rain (green curve), wide convective rain (red curve). For each $P(A)$, the circle-lines represent the approximation by the Log-normal distribution of rain attenuation needed for the TS model.

5.4.1 User's rain conditions simulation

First of all, a proper grid of users is to be defined in order to properly impose climatological characteristics and the desired spatial correlation of rain attenuation. The OBDPA system processes a cumulative information of rain, which describes the portion of the pixel area subject to certain rain attenuation. Given the specific spot of interest, the $P(A)$ curves in Fig. 5.8 represent the aggregate information, in space and time dimension, of the N_P pixels in the spot. The aim is to transform that information in a set of time series of rain attenuation, which represent the evolution over the 6 hours of the rain conditions across the area. To accomplish this task, a

grid of users is created for which rain conditions will be simulated. Fig. 5.9 shows the geographical area corresponding to spot 32 in Fig. 5.1.

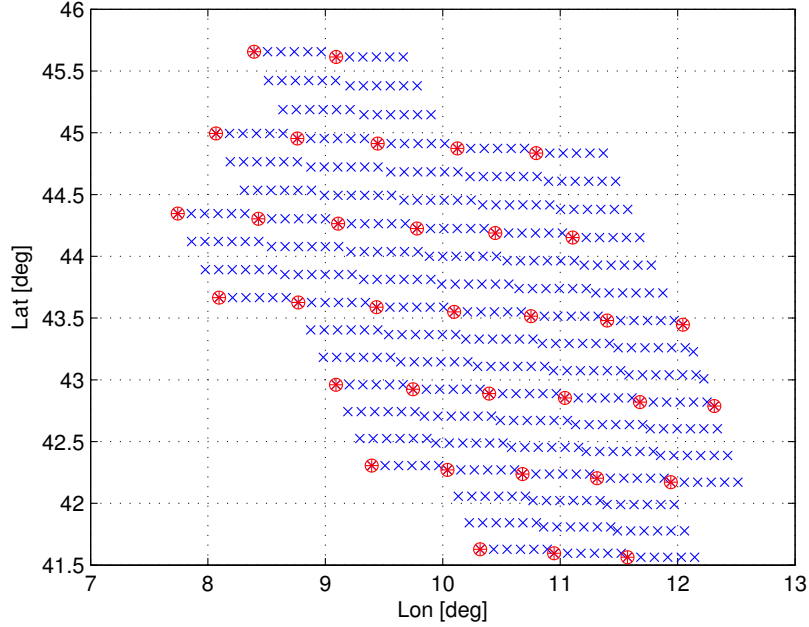


Figure 5.9: Grid of 500 users distributed in the spot n.32 region. Red users corresponds to the pixel grid of the RA system

The shape of the area represents the spot-footprint of the multibeam antenna. Its shape is elliptical and stretched because of the satellite position at latitude 0° (geo-stationary), longitude, 33° E.

The application of the Time Series (TS) model to the simulation of “on-demand” $P(A)$ at 6 hours is explained in the following. The added value of the proposed modelling is the possibility of describing the time evolution over the area during the 6 hours starting from the spot $P(A)$ integral information. This task is accomplished by assigning correlated “rainy” states among users on a hourly basis, then selecting proper time series of rain attenuation values for each user in “rainy” state, as described in Chapter 3.

Looking at the attenuation distributions in Fig. 5.8, each $P(A)$ starting point (p_0) is equivalent to the total fraction of the spot area in Fig. 5.9 covered by rain during the 6 hours. Referring to the rainy states assigning process in Sec. 3.6.2, a binary process is generated for each stations and mutual spatial correlation among rainy states imposed. Statistics of the generated process at 6-hours intervals are calculated to find the closest fraction of rainy area to the p_0 of interest. The resulting 6-hours binary evolution is then selected to provide the information of the rainy users for each single hour in the spot area in Fig. 5.9.

The total number of rainy users N_r is equivalent to the number of rain time series of 1 hour duration to be extracted from the database of measured attenuation to reproduce the target spot $P(A)$. This task is accomplished by applying the same methodology exposed in Sec. 3.6.1 and 3.6.3. Firstly, a set of N_r series of 1 hour duration are selected to model the $P(A)$, secondly the rain time series assigning process is in charge of selecting the most suitable time series for the rainy users every hour, to model the correct spatial correlation of the average rain attenuation over the hour. Resulting from this mathematical framework is a statistical description of the rain spatiotemporal distribution over the spot area for the selected 6-hours period, which resembles the meteorological attenuation distribution used to drive the OBDPA system.

The application of this modelling to realistic meteorological conditions is discussed In the next Sections.

5.5 Simulation methodology

The system analysis is carried by simulating the rain attenuation conditions for multiple users in the selected spot, obtained by implementing the TS model described

in Chapter 3. The purpose of the simulation is to prove the effects of the OBDPA for constant and adaptive ModCod transmissions, with the aim of assessing the advantage obtained by the variable power radiated on the spot, optimized according to the actual meteorological condition of the whole service area. The obtained results are compared with a fixed optimized antenna, i.e. an antenna whose radiated power, optimized for the long-term attenuation distribution, does not change in time.

For both CCM and ACM transmission modes, the methodology implemented for the simulation consists in the following steps:

- For the selected 6-hours period, generating a rain attenuation distribution over the beam area which reflects the meteorological information available to the OBDPA system and which drive its re-configuration, i.e. optimization of the excitation coefficients w responsible for the radiation over the whole service;
- Computing the SNIR in Eq. (5.1), SE in Eq. (4.8) for the OBDPA system, for each user in the selected beam j , according to the 6-hours optimized radiated power $f(w_j)$;
- Computing the SNIR in Eq. (5.1), SE in Eq. (4.8) for the fixed antenna system, for each user in the selected beam j , according to the long-term optimized radiated power $f(\bar{w}_j)$;
- Computing the user throughput according to Eq. (4.10) and availability (percentage of time Eq. 4.6 is verified over the 6-hours interval), according to the available transmission scheme, for both OBDPA system and fixed antenna;
- Averaging the results over the 6-hours time period, defining a proper figure of merit to judge the advantage of the OBDPA. The average value is calcu-

lated taking into account both rainy and not rainy time in the hypothesis of a continuous service.

5.6 Simulation results

The following figures show the obtained SNIR distribution, SE distribution and throughput analysis for the spot 32 in the service area, according to the predicted meteorological conditions described above. The transmission system performances are evaluated in the following cases:

- Fixed front end antenna system: CCM and ACM
- OBDPA system: CCM and ACM

Concerning the modulation and coding, the reference scheme is the one proposed in the DVB-S2 [78] standard. DVB-S2 is envisaged for broadcast services and TLC services including standard and High Definition Television (HDTV), interactive services including Internet access, and (professional) data content distribution. The standard main features in terms of modulation schemes, spectral efficiency and SNIR thresholds are summarized in Tab 5.2.

5.6.1 Test case 1: Wide stratiform rain

In this first example, a wide stratiform rain over the service area is considered. Rain is characterized by a large extension and low to moderate rain rates. This information is derived by the cumulated rainfall amount over the 6 hours period derived by ECMWF predictions [73] and shown in Fig. 5.6.

Mod.	Inner code rate r	ξ (bits/s/Hz)	SNIR (dB)
QPSK	1/2	0.99	1.01
	3/5	1.19	2.23
	2/3	1.32	3.10
	3/4	1.49	4.04
	4/5	1.59	4.68
	5/6	1.66	5.18
8PSK	3/5	1.78	5.61
	2/3	1.98	6.72
	3/4	2.23	8.01
16APSK	2/3	2.64	9.07
	3/4	2.97	10.31
	4/5	3.17	11.14
	5/6	3.30	11.71
32APSK	3/4	3.60	12.66
	4/5	3.86	13.63
	5/6	4.03	14.28
	8/9	4.30	15.68
	9/10	4.35	16.04

Table 5.2: ModCod, SE and required SNIR according to the DVB-S2 standard. Required SNIR is targeting a quasi-error free transmission goal of 10^{-7} packet error rate

5.6.1.1 Rain attenuation modelling

The first step is to describe the rain attenuation conditions over the service area by a proper processing, to make them applicable to the OBDPA system. Considering the single beam area and the time evolution period of 6 hours, the first task is to expand in space and time the integral information of the attenuation distribution, in order to describe each single user conditions on the service area at any given moment within the 6 hours time frame.

This task is accomplished by the TS model as previously introduced. Considering the green curve in Fig. 5.8, it describes the rain attenuation conditions, in space and time, on the service area for the selected meteorological “snapshot”. Fig. 5.10

shows the simulated rainy states over the reference area for the considered curve. Red circles are the users subject to rain in the reference grid at each hour: “rainy” users results from a single realization of a random process, which takes into account the spatial correlation among users (based on their distance) and the temporal correlation interval of stratiform rain events (Chapter 3).

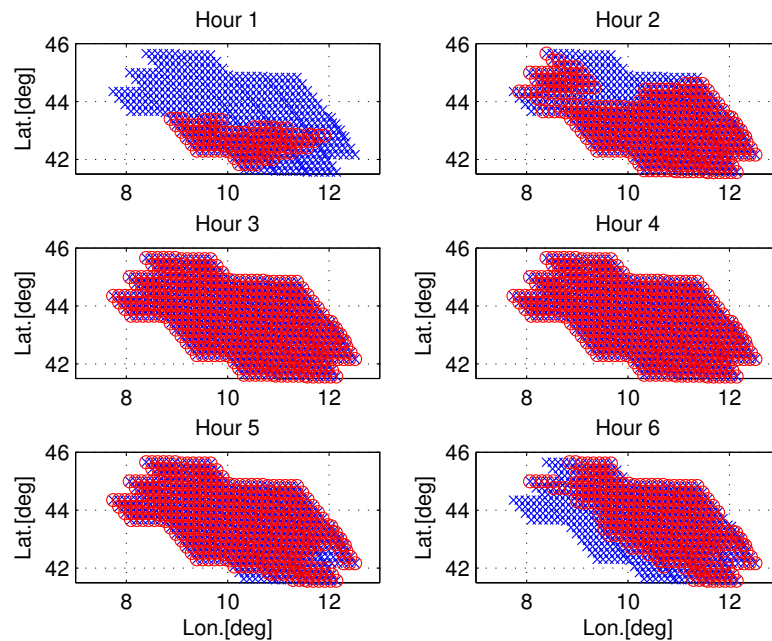


Figure 5.10: Test case I: snapshot 001228ss01. Spatio/temporal evolution of the number of rainy stations during the 6-hours period. Blue crosses represents the simulated users in the area, red circles the fraction of users under rain at each hour. It is clearly visible the spatial feature of rainy states and its temporal evolution.

From Fig. 5.10 it is clear that the considered 6 hours are characterized by a significant rain event, which almost covers the spot area completely (high p_0). The rain attenuation distribution $P(A)$ obtained by the time series selected by the TS model is shown in Fig. 5.11, together with the target $P(A)$ obtained by the meteorological information processing.

As clear from Fig. 5.11, the obtained time series of rain attenuation well de-

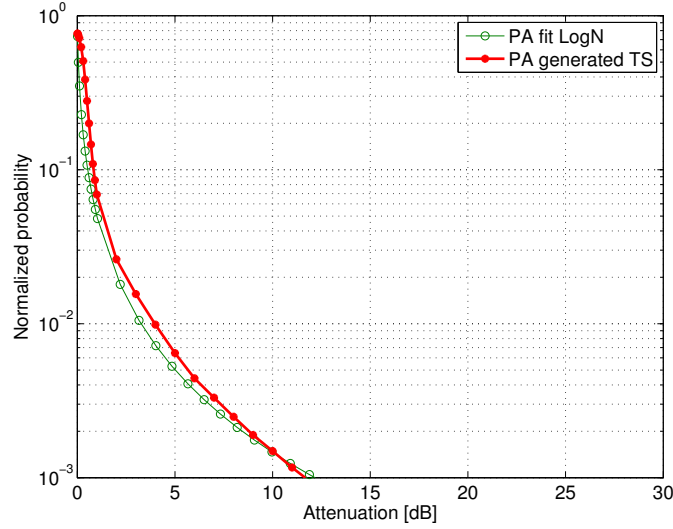


Figure 5.11: Test case I: snapshot 001228ss01. Rain attenuation distribution in space/time. Green line is the target distribution as derived from meteorological information for the 6 hour period, the red line is the simulated rain arranged in time series of 1 hour for all the rainy users. The starting point of the curve is the total fraction of users which experience rain attenuation

scribe the target rain attenuation distribution over the spot area. The rain evolution modelling in Fig. 5.10 well matches the information of the fraction of rainy area over the spot in the 6 hours time. It is clearly visible the spatial correlation among “rainy” users (red dots) and their time evolution over the hours.

5.6.1.2 SNIR and user channel capacity assessment

Given the rain attenuation conditions simulated above, firstly the user’s SNIR is calculated. The time series of SNIR are obtained for each users considering the time series of rain attenuation and the signal power and interference generated by the transmitting antenna, according to Eq. 5.1. Two antennas area considered: a fixed one, optimized for the long term rain attenuation statistics, and the reconfigurable one (OBDPA), whose radiated power is optimized according to the simulated mete-

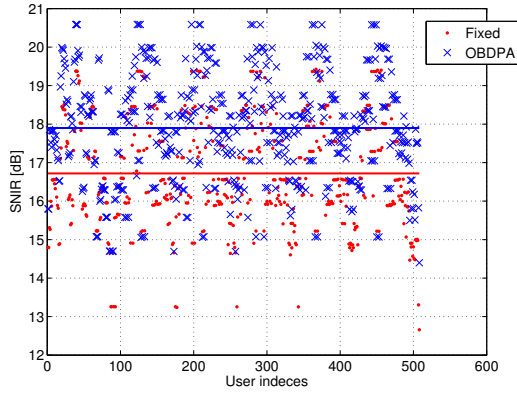


Figure 5.12: Average user SNIR values obtained for Fixed and OBDPA system

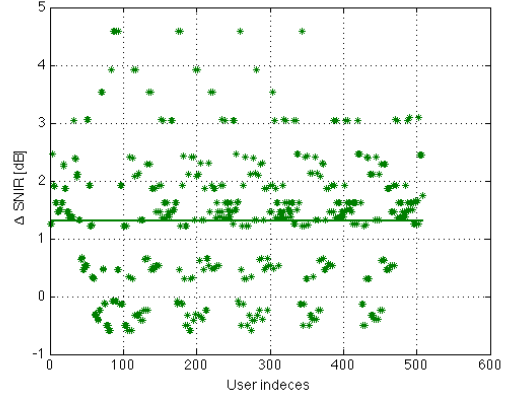


Figure 5.13: Average user SNIR gain of the OBDPA system. The OBDPA provides an average higher SNIR to almost all the simulated users

orological 6-hours prediction.

Fig. 5.12 shows the average user SNIR in the spot over the 6 hours period. The SNIR values are calculated according to the definition in Eq. 5.1. The advantage of the OBDPA system is clearly visible by the blue crosses which are consistently above the red dots. This can be appreciated by looking at the average gain $\text{SNIR}_{OBDPA} - \text{SNIR}_{Fixed}$, which is greater than zero for almost all the simulated users. The CDF of the average users SNIR values is shown in Fig. 5.14: the shift of the distribution towards higher values of SNIR is the effect of the higher power radiated on the spot by the OBDPA system.

The channel capacity for each users is derived by:

$$C = \log_2(1 + \gamma) \quad (5.5)$$

where γ is the user SNIR time series. Referring to Tab. 5.2, the achieved SE of the systems is obtained by considering the best allowed transmission scheme. Given the SNIR time evolution of each users, the theoretical SE is obtained as in Eq. 4.8 by the

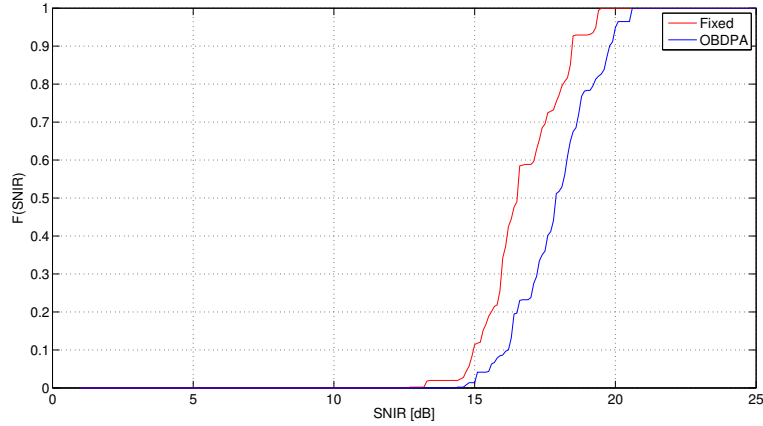


Figure 5.14: Test case I: snapshot 001228ss01. CDF of average SNIR users values in the simulated spot. The average SNIR per user is obtained over the 6-hours period.

Fixed front end antenna (red) compared with OBDPA system (blue)

highest modcod supported in Tab. 5.2. The average user channel capacity and SE over the time period are shown in Fig. 5.15. Values are obtained simply averaging over the 6-hours and taking into account both rain and no rain conditions.

The blue crosses represent the average SE of the OBDPA compared with the red dots of the fixed front-end antenna. A blue cross above the line marked by red dot means an increase in the SE of the specific user. Fig. 5.15 shows that the channel capacity achieved by the OBDPA is in general higher than the one obtained by a fixed front end antenna. In terms of SE (left part of Fig. 5.15), a saturation effect is visible due to the highest transmission scheme in place, as well as significant gain between the red dots and blue crosses on the left part of the graph. The few exceptions (blue crosses below the red dots) represent a subset of users which experience either a very deep rain fade or significant interference. Since the OBDPA system is not able to resolve single users but only the spot attenuation conditions, some users may incur in a SNIR degradation resulting from the combination of local attenuation and co-frequency beams interference. Must be noticed that a degradation in SNIR does not

result automatically in a user outage, which depends on the transmission scheme in place.

In order to better appreciate the effect of the OBDPA in rain fades, the minimum value of users SE is considered, for fixed and OBDPA system. It is expected that the OBDPA would provide an extra power margin to compensate rain fades occurring at users, thus reducing their SE degradation. This is shown in Fig. 5.16, where the SE time series is plotted as function of time. Two random users are selected in the spot area, they experience a visible rain fade in distinct moments of time. The OBDPA (blue line) outperform the fixed antenna by reducing the rain fade impact on the SE curve. Considering now all the users, the minimum SE experienced by the users during the 6-hours is calculated for the two antennas in place. Results are shown in Fig.5.17.

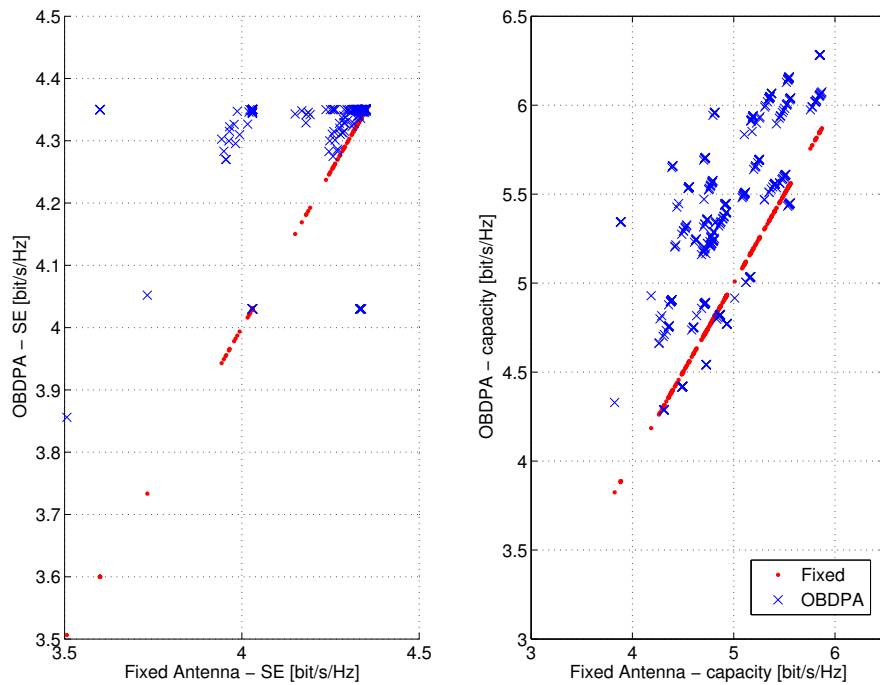


Figure 5.15: Test case I: snapshot 001228ss01. Scatter plot of channel capacity (right) and spectral efficiency (left). Fixed antenna (red) and OBDPA (blue). The blue crosses above the line defined by the red dots represent a gain in terms of channel capacity or SE.

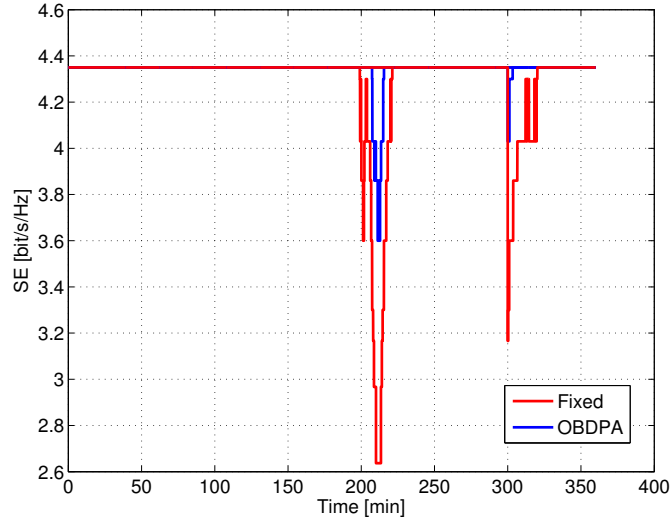


Figure 5.16: Test case I: snapshot 001228ss01. Time evolution of SE for two selected users in the spot, subject to two separate rain fades. The extra margin provided by the OBDPA system results in a less severe degradation of users SE due to rain fades

5.6.1.3 Throughput and availability analysis

In order to better assess the effects of the two power allocation schemes on the system performances, throughput and user availability have been evaluated accounting CCM and ACM transmission, with and without OBDPA. Throughput is obtained by the integral of the achieved SE over the 6-hours period, according to Eq. (4.10). Availability is defined as the percentage of time over 6-hours the required SNIR for the link closure definition in Eq. (4.6) is not achieved. In CCM mode, two constant modcod are selected:

- *CCM1* 8 PSK(2/3): low SE mode [79]
- *CCM2* 32 APSK (5/6): aggressive mode (roughly doubled SE than previous)

Concerning the ACM transmission mode, ideal channel feedback to the transmitter is considered: the best supported modcod is selected at each sample of the SNIR time

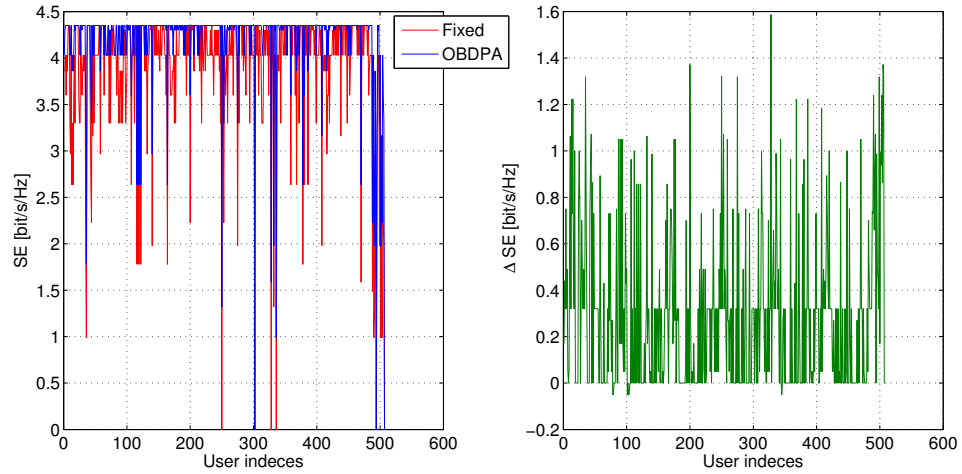


Figure 5.17: Test case I: snapshot 001228ss01. Minimum value of SE for each users for fixed and OBDPA system (Left). Reduction of SE worst degradation: $(SE_{OBDPA} - SE_{fixed})$ (right). Average $\Delta SE = 0.4$

series (ideal channel feedback to the transmitter). Fig. 5.18 shows the average user throughput obtained by the proposed transmission modes.

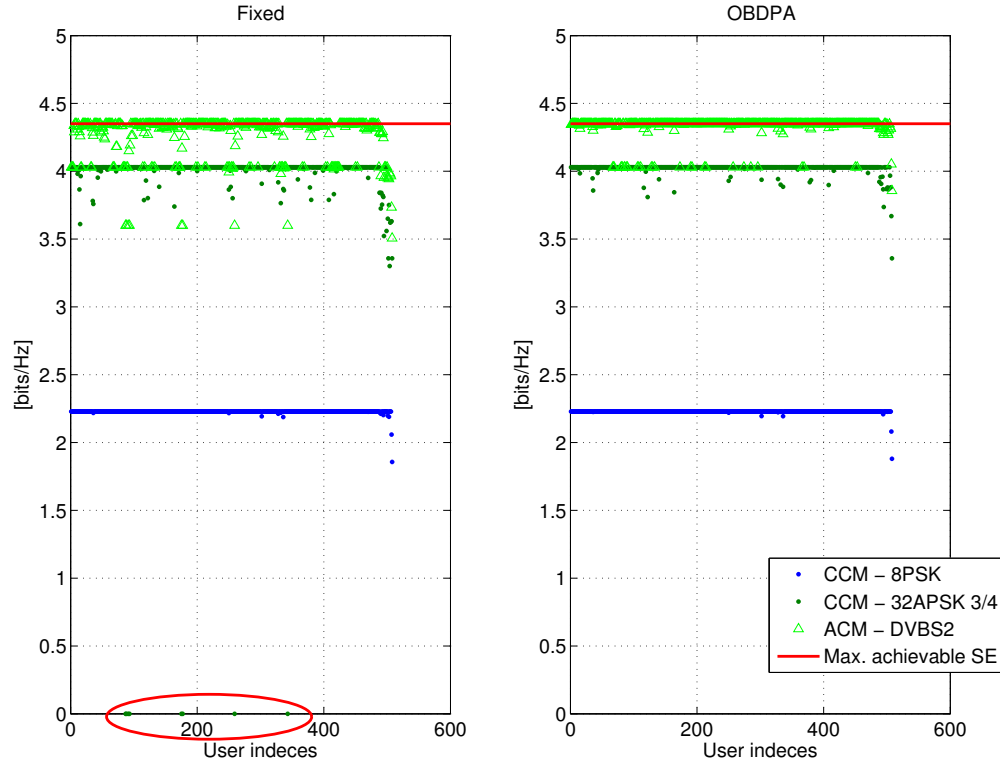


Figure 5.18: Test case I: snapshot 001228ss01. Average user throughput for CCM and ACM, with OBDPA (right) and fixed antenna (left)

On the left side, a fixed front end antenna is shown. The average throughput per user is calculated as the SE of the selected modcod multiplied by the times the user SNIR is above the required modcod threshold. In the CCM case, different values of average throughput results from outages during the 6-hour simulated period. The more aggressive scheme (green dots) results in higher throughput for most of the users, but some users experience severe outages (red circle) in the 6-hours time period: their SNIR time series does not support the high mode selected. Different results are obtained when ACM is in place (light green triangles): ideally the best supported modcod is always selected leading to an increase in throughput and limiting the user

outages. This at the cost of added system complexity to provide the receiver channel information to the transmitter. On the right side of Fig. 5.18, the same transmission schemes coupled with OBDPA are shown. While there is no sensible difference in the lowest constant transmission rate (blue dots), the higher constant rate (green dots) is better supported: no users experience complete outage and a better user availability can be appreciated with no users experiencing severe outages. Looking at ACM modes, green triangles exhibit a lower variation compared to the ACM and fixed antenna. In this case, a more stable throughput among the users is achieved.

The previous considerations find support in the following results. Fig. 5.19 shows the user outage obtained by the high constant rate transmission (CCM2), in case of a fixed antenna (blue) and the OBDPA system (red). The outage is the percentage of time the high constant rate is not supported over the 6 hours. It is clear the benefit of the OBDPA in terms of reduced user outage for the constant rate selected. Considering the outage distribution over users, the same advantage is shown in Fig. 5.20, where the probability of users having outage higher than thresholds is shown. In the considered period, no users experience cumulative outage longer than 5% over the 6-hours when OBDPA is used. Especially for CCM, the benefit of OBDPA is a reduction of almost 50% of users experiencing outage.

Fig. 5.20 shows that the coupled use of ACM and OBDPA does not lead to a sensible increase in user availability: a similar level is already obtained by the ACM use only. Instead, the effect of OBDPA is more visible in the modcod usage distribution. Fig. 5.21 shows the overall availability of modcods in time for all the users. The effect of the OBDPA system is to increase the availability curve for high modcods, thus allowing their use to more users and for a larger fraction of time. The same result can be observed in the histogram of modcod distribution in Fig. 5.22. In general, a reduction in terms of overall use of lower modcod, evaluated for all the

users, is visible. A usage increase appears consequently in the highest modcod bar.

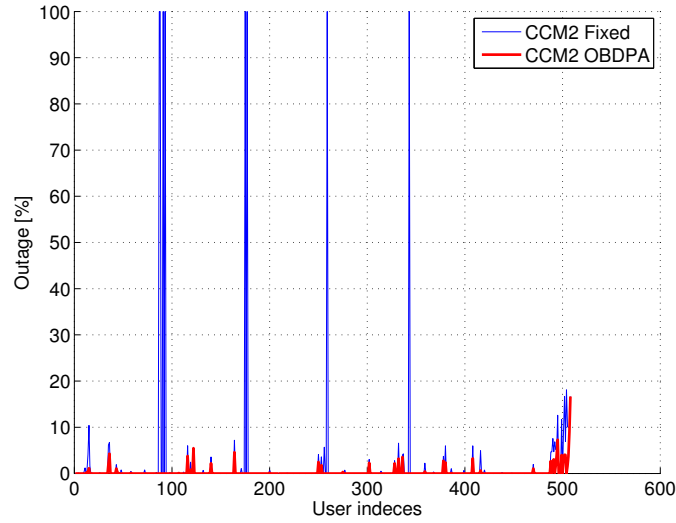


Figure 5.19: Test case I: snapshot 001228ss01. User outage for high CCM, fixed fron-end compared to OBDPA antenna.

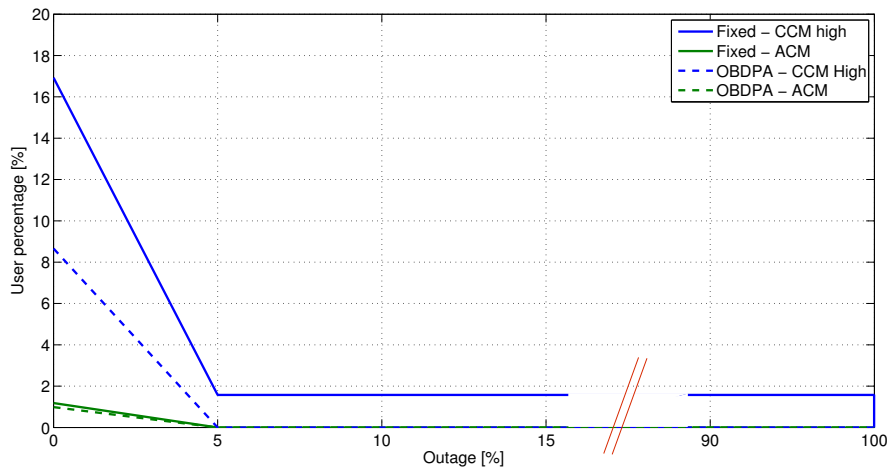


Figure 5.20: Test case I: snapshot 001228ss01. CCDF of user outage for high CCM and ACM, fixed antenna compared to OBDPA antenna.

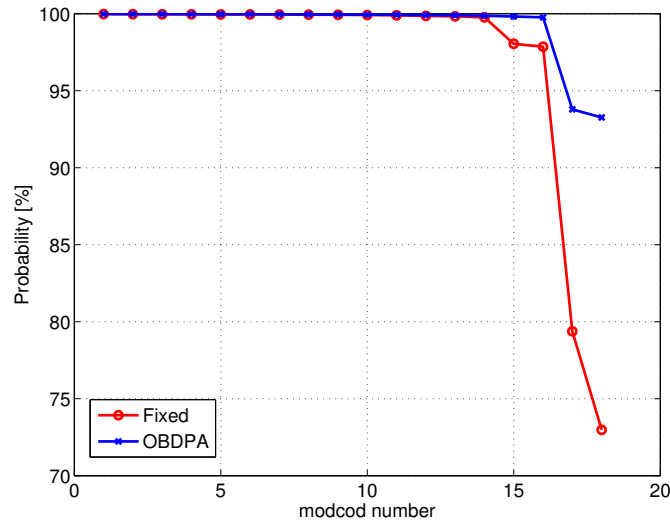


Figure 5.21: Test case I: snapshot 001228ss01. Availability of modcod (percentage of time evaluated for all the users). Comparison between fixed antenna (red) and OBDPA antenna (blue)

Fig. 5.23 shows the advantage in terms of throughput for the simple ACM (fixed front-end) and the ACM with OBDPA. The previous consideration in terms of higher modcod usage is appreciable also by looking at the throughput gain obtained by the joint use of OBDPA and ACM compared to the case of simple ACM, shown in Fig. 5.23. Looking at the throughput statistics, an interesting result is that the average throughput gain is in the order of 5% but the standard deviation of user's throughput is reduced of almost 50%, leading to a more uniform aggregated throughput over the whole spot.

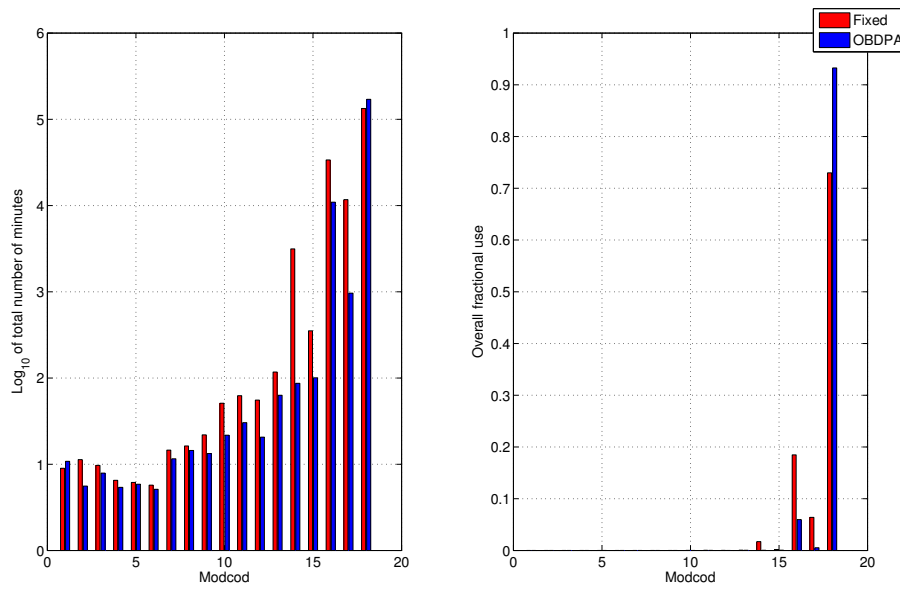


Figure 5.22: Test case I: snapshot 001228ss01. Modcod histogram of overall usage (time evaluated for all the users). Comparison between fixed front end (red) and OBDPA antenna (blue)

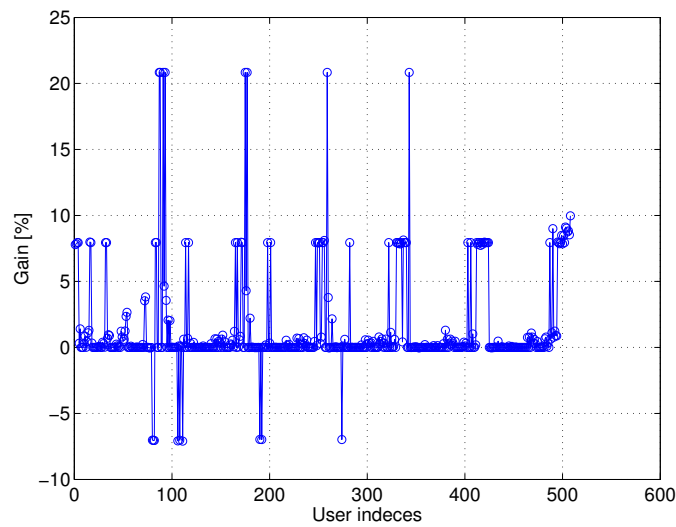


Figure 5.23: Test case I: snapshot 001228ss01. Average user throughput gain using ACM coupled with OBDPA

5.6.2 Test case 2: Multiple convective cells

A similar analysis is carried on a different rain distribution over the whole service area, characterized by multiple convective rain cells, i.e. multiple localized areas subject to moderate/strong rain intensity (Fig. 5.7). This is considered as a critical case for the OBDPA system since a large amount of power has to be redistributed over different service spots. The rain attenuation distribution on the spot is described by the red curve in Fig.5.8: it can be noted the presence of higher attenuation values and a lower integral of rain covered area compared to the previous case.

5.6.2.1 Rain attenuation modelling

As previously explained, integral information related to rain attenuation distribution provided by the curve in Fig. 5.8 is expanded in space and time according to the method in Sec. 5.4.1, in order to describe each single user conditions on the spot area at any given moment within the 6 hours time frame. Fig. 5.24 shows the simulated rainy states over the reference area for the considered curve. Red circles are the users subject to rain in the reference grid at each hour: “rainy” users results from a single realization of a random process, which takes into account the spatial correlation among users (based on their distance) and the temporal correlation interval of stratiform rain events (Chapter 3).

The simulated area in Fig. 5.24 exhibits a different rain distribution than the previous case, limited to the first 4 hours and characterized by separate rainy areas (red circles). The overall amount of rainy users is defined by the p_0 value of the attenuation distribution shown in Fig. 5.25. This information is used to derive a random binary process for each user, with a duration of 6 hours, which assigns the user rainy states preserving the spatial correlation among users and the temporal

correlation of rain (Sec. 5.4.1). The rain attenuation distribution $P(A)$, which is obtained by the current spot predictions and drives the antenna reconfiguration, is reproduced by the time series selected by the TS model, as shown in Fig. 5.25.

5.6.2.2 SNIR and user channel capacity assessment

The time series of SNIR are obtained for each users considering the time series of rain attenuation and the signal power and interference generated by the transmitting antenna, according to Eq. 5.1. A fixed antenna and the OBDPA system are considered. The CCDFs of the average users SNIR are shown in Fig. 5.26 for the two cases.

Concerning the achieved channel capacity and SE, their average value is shown in Fig. 5.27. With respect to the previous case, it is clearly visible a subset of user whose average capacity appears to be reduced by the OBDPA system (blue crosses below the red line of fixed antenna capacity). On the other hand, a large number of users show higher average capacity to be exploited. Interesting is also to look at the minimum value of users SE over the 6-hours period in Fig. 5.28. There is a significant reduction in the worst SE degradation for the major number of users, while a worse degradation must be accounted on others.

The investigation on the worse users in the spot area shown that the responsible for the capacity degradation (and consequently SE reduction) is to be found the the interference due to co-frequency beams. Fig. 5.29 shows the OBDPA antenna excitation coefficients for the whole service area. Co-frequency beams 9 and 34 are characterized by high radiated power which generates high levels of interference in the upper-left spot area, where the users with low channel capacity are located.

5.6.2.3 Throughput and availability analysis

The previous considerations help to explain the analysis of throughput and availability, which have been evaluated for CCM and ACM transmission, with and without OBDPA. The same definition of throughput and availability as in the previous case is considered. As previously done, in CCM mode, two constant modcod are selected:

- *CCM1* 8 PSK(2/3): low SE mode [79]
- *CCM2* 32 APSK (5/6): aggressive mode (roughly doubled SE than previous)

Concerning the ACM transmission mode, ideal channel feedback to the transmitter is considered: the best supported modcod is selected at each sample of the SNIR time series (ideal channel feedback to the transmitter). Fig. 5.30 shows the average user throughput obtained by the proposed transmission modes. On the left side, a fixed front end antenna is shown. The average throughput per user is calculated as the SE of the selected modcod multiplied by the times the user SNIR is above the required modcod threshold. In the CCM case, different values of average throughput results from outages during the 6-hour simulated period. The more aggressive scheme (green dots) results in higher throughput for most of the users, with some severe outages of a subset of users. Different results are obtained when ACM is in place (light green triangles): ideally the best supported modcod is always selected leading to an increase in throughput and limiting the user outages. This at the cost of added system complexity to provide the receiver channel information to the transmitter. On the right side of Fig. 5.30, the same transmission schemes coupled with OBDPA are shown. As expected, there is no sensible difference in the lowest constant transmission rate (blue dots). In this case, also the higher constant rate (green dots) is worse supported with a larger number of users who experience complete outage.

Looking at ACM modes, green triangles exhibit a higher variation compared to the ACM and fixed antenna, while maintaining a good system availability. Also in this case, among the served users, a more stable throughput is achieved.

In terms of user availability, the CCDF of outage probability among users is shown in Fig. 5.31. For a system with no OBDPA, outage affects roughly the 10% of the users with CCM, less than the 2% in case of ideal ACM. The OBDPA in this case results in a higher outage distribution affecting users with low SNIR.

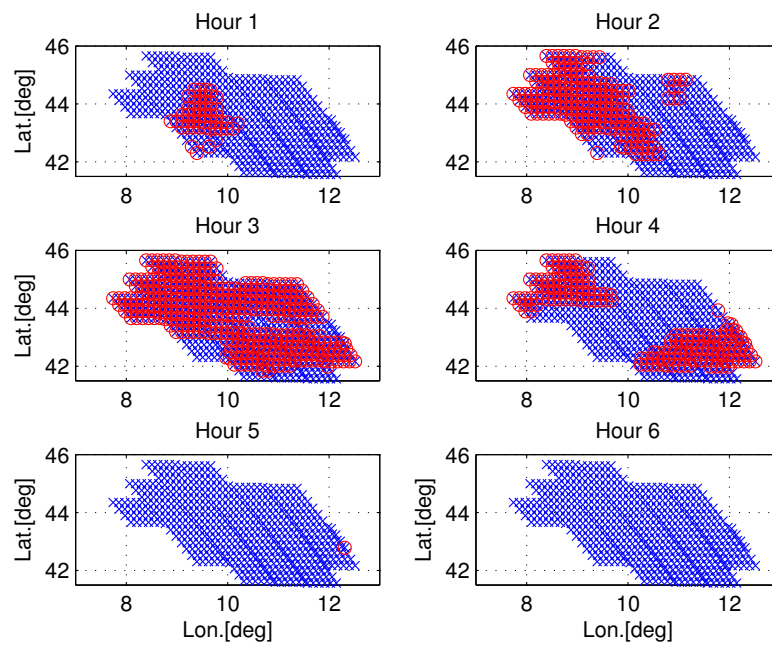


Figure 5.24: Test case II: snapshot 000715ss01. Spatiotemporal evolution of the number of rainy stations during the 6-hours period

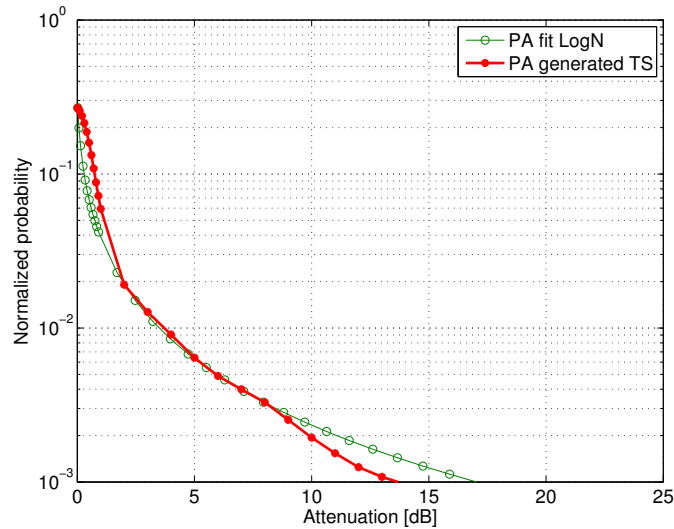


Figure 5.25: Test case I: snapshot 000715ss01. Rain attenuation distribution in space/time. Green line is the target distribution as derived from meteorological information for the 6 hour period, the red line is the simulated rain arranged in time series of 1 hour for all the rainy users. The starting point of the curve is the total fraction of users which experience rain attenuation

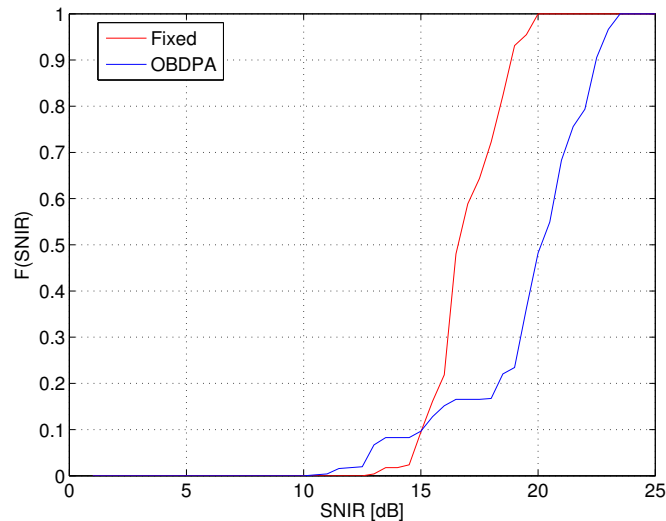


Figure 5.26: Test case II: snapshot 000715ss01. CCDF of average user SNIR for fixed antenna (red) and OBDPA system (blue). The average value is evaluated over the 6-hours time period

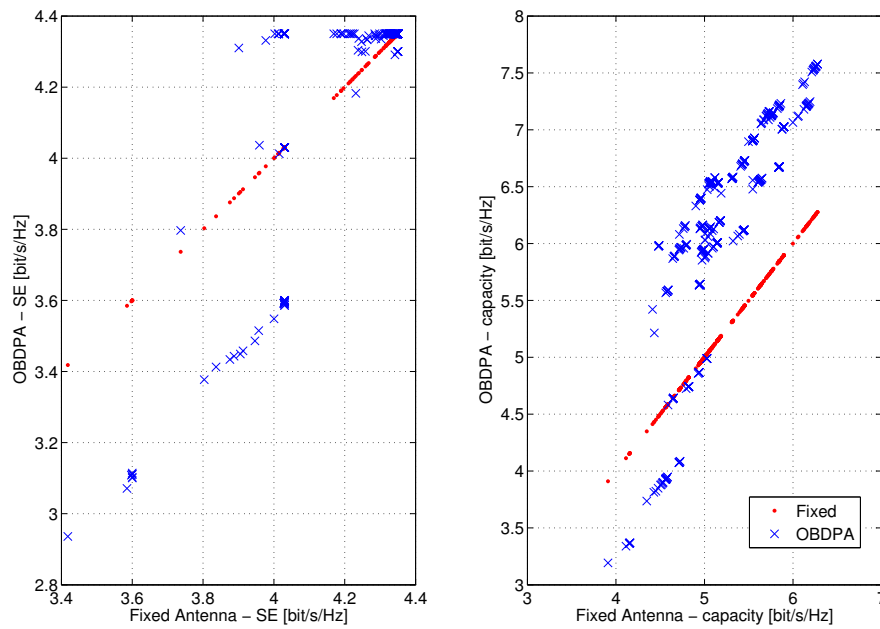


Figure 5.27: Test case II: snapshot 000715ss01. Scatter plot of user average channel capacity (right) and average SE (left) for fixed antenna (red dots) and OBDPA (blue crosses). The blue crosses above the line defined by the red dots represent a gain in terms of channel capacity or SE.

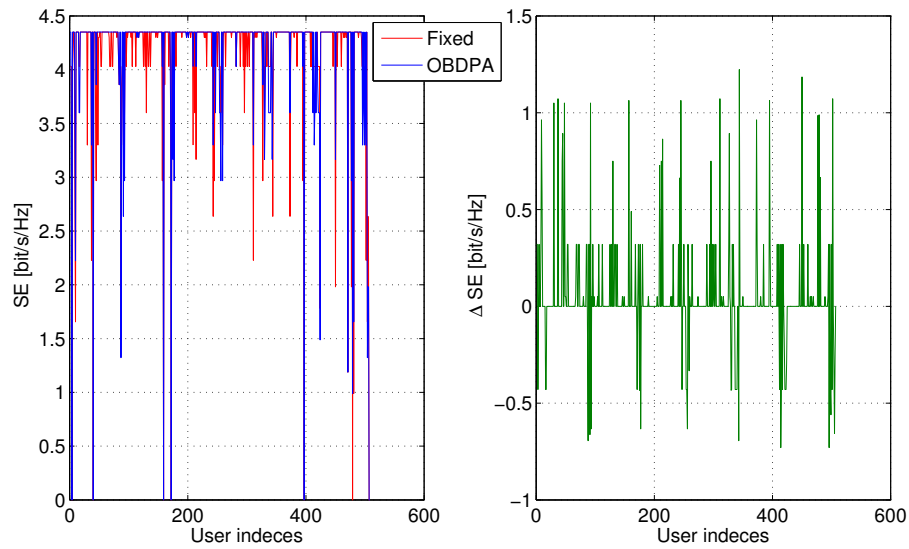


Figure 5.28: Test case II: snapshot 000715ss01. On the left: minimum value of user SE for the considered 6 hours period. Fixed antenna (red) compared with OBDPA system (blue). On the right, the SE gain $SE_{OBDPA} - SE_{fixed}$ in terms of minimum value. Average increase $\Delta SE = 0.35$

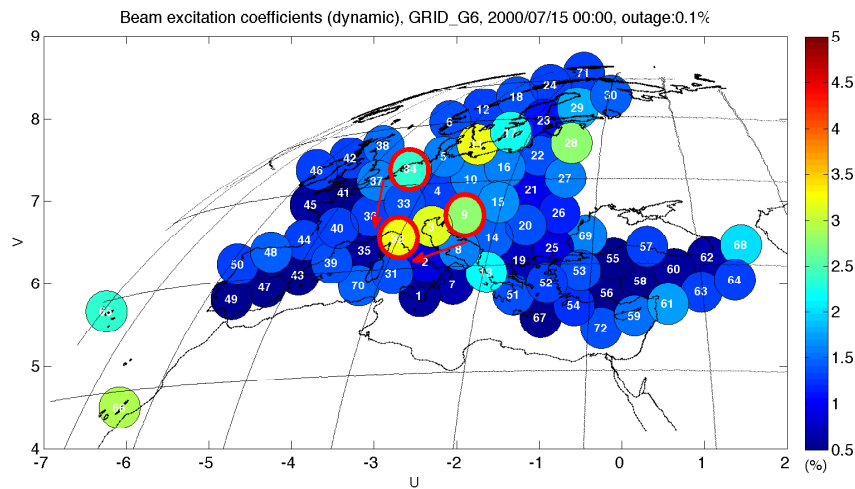


Figure 5.29: Test case II: snapshot 000715ss01. Values of OBDPA antenna excitation coefficients across the whole service area

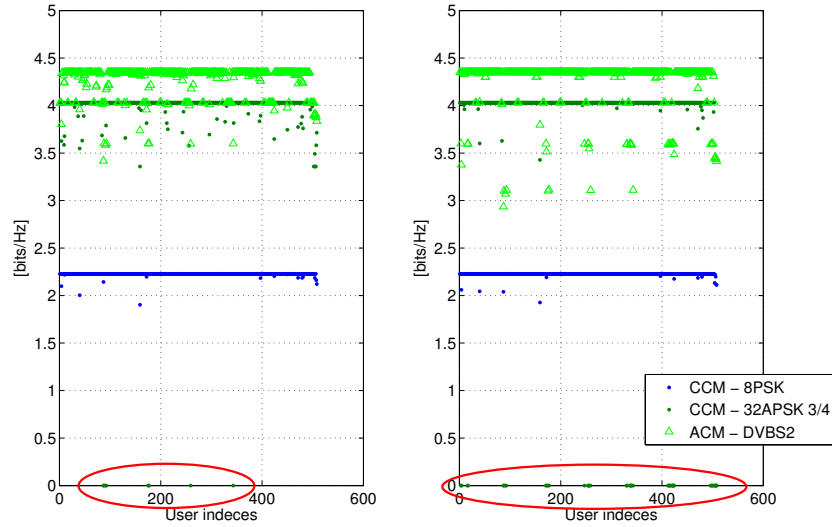


Figure 5.30: Test case II: snapshot 000715ss01. Average user throughput for CCM and ACM, with OBDPA (right) and with fixed antenna (left)

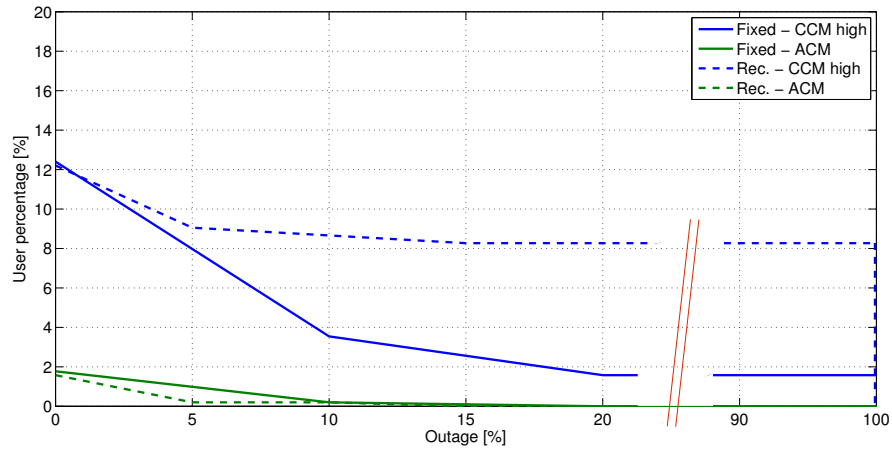


Figure 5.31: Test case II: snapshot 000715ss01. Distribution of user outage for CCM (blue) and ACM schemes (green). The effect of OBDPA is shown by the dotted lines

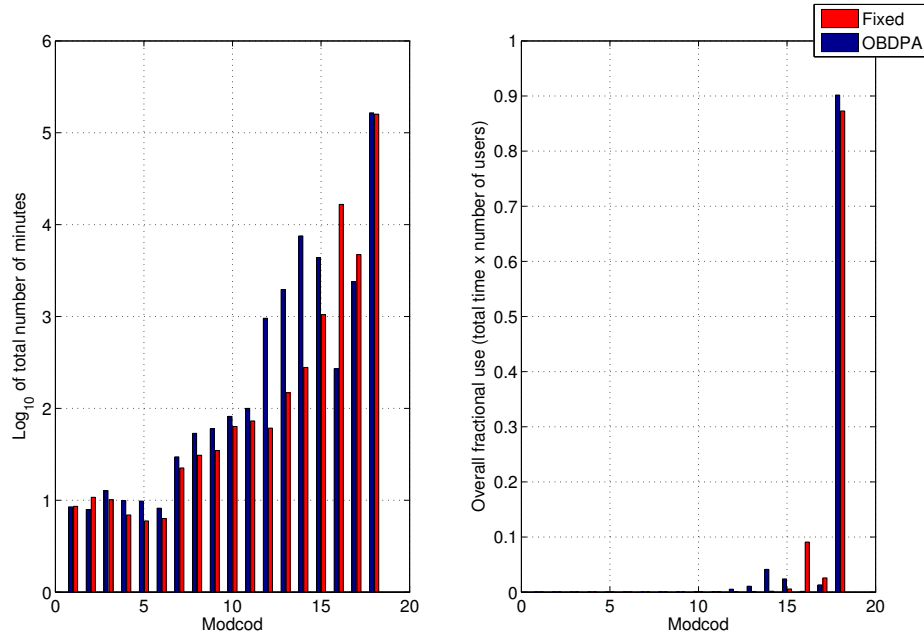


Figure 5.32: Test case II: snapshot 000715ss01. Histogram of modcod overall usage for fixed (red) and OBDPA system (blue)

The effect of OBDPA with ACM is more visible in the modcod distribution in Fig. 5.32. It appears that the dynamic power allocation results in a higher use of lower modcods, possibly related to users with lower SE. Translating this information in terms of throughput for ideal ACM, the user's gain in Fig. 5.33 shows both positive and negative variations, the negative related to those group of users affected by lower SNIR and SE. Considering the throughput statistics over the spot, the variation of the average user throughput is not relevant (-0.2%) while a sensible increase in the throughput standard deviation among users is noted $+58\%$, due to the presence of both positive and negative throughput gains. Considering only the positive throughput gains, the standard deviation of the final throughput with OBDPA is reduced by a factor of 3 compared to the case of ACM transmission with no OBDPA.

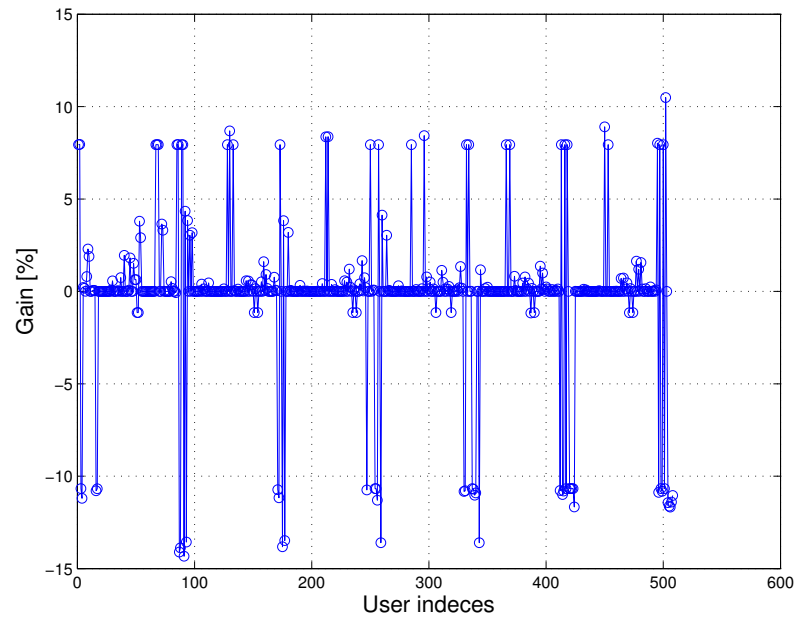


Figure 5.33: Test case II: snapshot 000715ss01. Average user throughput gain using ACM coupled with OBDPA

5.7 Conclusions

In this Chapter the performance of different transmission strategies over one spot of a multibeam antenna system with OBDPA has been derived and discussed.

A multibeam satellite system has been considered, transmission may occur in CCM mode, ACM and OBDPA may be introduced in support to the previous techniques and compared to a fixed antenna system. A grid of users has been defined on the service area, rain attenuation conditions, reflecting real meteorological information made available by ECMWF, have been reproduced on the target spot area by means of the TS model previously introduced.

The SNIR for each users have been defined and selected as a proper figure of

merit to assess the user's conditions in the service area. The users SNIR depend on the current antenna radiated power, link attenuation (rain), interference of co-frequency beams.

One spot in the center of the coverage area has been selected to assess the system performances, based on free-space considerations related to the antenna in place. Two rain attenuation conditions have been selected to test different transmission schemes, in order to assess users service quality in terms of availability and throughput in case of:

- CCM transmission with and without OBDPA
- ACM transmission with and without OBDPA

The first scenario is characterized by a widespread rain distribution (stratiform rain) across the service area. The TS model in use allows to simulate the correlated rain attenuation conditions of multiple users in the spot, in order to test the effects of the different transmission schemes on the simulated users.

The most important system results show that CCM at aggressive rates suffers of users complete outage, which is reduced and avoided by the introduction of the antenna power optimization. The ideal ACM transmission mode is able to almost completely reduce the users outage, at the cost of the very high complexity required to provide accurate user's link state information to the transmitter. The effect of the OBDPA on the ACM is not in terms of user's availability but average throughput gain. By looking at the distribution of modcod usage, it is clear that the OBDPA provides a significant advantage in supporting higher modcods. In terms of throughput statistics, it is important to note that the joint use of ACM and OBDPA leads to an increase of the average throughput of roughly 6%, characterized by a substantial decrease in the throughput standard deviation among users close to 50% for the analyzed case.

The second scenario considered is characterized by multiple cells of convective rain over the service area. The critical aspect in this case is that the OBDPA needs to redirect power on many different areas. The antenna performances appears to be limited in this scenario. The analysis of the power radiated by the optimized front-end shows a good increase in the available users SE, while a group of users are subject to SE degradation. The reason is to be found in the system interference generated by co-frequency beams, which has a dominant effect compared to the rain attenuation. The power dynamic allocation is driven by the lowest SNIRs in the whole area, thus the available power on single beam considered is constrained and degradation of users may occur.

Concerning users outage, in this scenario a CCM system is limited by the users with lowest SNIR. On the opposite, with ACM it is possible to cope with the power limitation imposed by the OBDPA and maintain a very low user outage. By looking at the time evolution of users conditions, the OBDPA results in a consistent limiting action towards the SE degradation due to heavy fades. The average gain is around 10% of the achievable SE.

The average throughput gain evaluated on the simulated users depends on the user SE resulting from the dynamic power allocation: in this case the overall gain is close to 0% due to the loss in SE of a group of users. Instead, the reduction of the standard deviation of throughput who experience a positive gain is reduced by 30%.

By investigating the presented results one can observe the effects of dynamic power adaptation in different transmission modes. When a feedback link is not available (one directional applications), the CCM transmission may incur temporary outages (rain fades) or complete outages for users which are subject to high interference (the required SNIR to support the transmission is not achieved in the observed period). In this scenario, the OBDPA results in reduced outage probability for the

users not subject to high interference.

In case ACM is available (under the assumption of a complex feedback system), results presented above show that the power adaptation effectively support ACM transmission schemes. When extra power margin is available, its effect coupled with ACM results in:

- a reduced heavy fades in the 6 hours time (i.e. higher minimum user SE) gain
 $\Delta SE_{min} \approx +10\%$
- a higher ModCod support: total probability of highest ModCod usage +20% for stratiform rain case and +5% for convective rain;
- a reduced standard deviation of average throughput among some users is observed: -50% for stratiform rain and -30% for convective rain;

In other situations, performances are limited due to the presence of a subset of users limited by system interference. For those users, a reduction in throughput is observed while users availability is preserved by ACM transmission schemes.

The analysis here presented covers a single spot of the service area considered for the multibeam satellite system. By general considerations regarding the whole service area, no significant variations are expected by the analysis of different spots, at least concerning the center part of the service area (spots on the margins are less subject to interference and are characterized by better user conditions simply by the antenna design). The analysis proposed here and the generated results are developed on single meteorological events, thus are not exhaustive to provide an overall performance assessment of the OBDPA system. It appears also difficult to select a significant subset of different meteorological conditions to be able to derive conclusive performance results. The two proposed meteorological situations discussed above

appears of interest due to their rain characteristics in relationship with the OBDPA system. The techniques tested on those short studies can be directly applied to the investigation of long-term simulations, in order to take into account a large ensemble of meteorological conditions and to improve the understanding of the OBDPA system. This future development will be subject of a stand-alone study.

Chapter 6

Conclusions

In this thesis, we have explored a number of topics connected to the joint use of two Fade Mitigation Techniques to counteract rain attenuation for satellite communications in the Ka frequency band. Our goal has been to further the research in these areas in two directions: on one hand we have investigated the joint use of FMTs, on the other to support the use and realization of OBDPA systems, by proving their potential advantage coupled with already in-use ACM techniques. Below we summarize the work presented in the thesis and give our recommendation for extending the research.

Following the introduction in Chapter 1, Chapter 2 presents a comprehensive survey on the modelling of atmospheric attenuation; specifically concerning rain attenuation, the most accurate models to predict rain attenuation distribution have been discussed and their accuracy was assessed by comparison with the reference statistical model ITU-R P.618-10 and a comprehensive database of measurements. Physical based models such as SC-ExCell and SST perform well over a wide probability range in the prediction of the attenuation distribution, both starting from local climatological information or statistical climatological maps.

It has been found that, in order to address multiple users attenuation conditions, vectors of time series which describe the rain attenuation evolution in time are needed. Especially, concerning multisite representation, the problem of spatial correlation

among sites at different distances arises. The spatial correlation reflects the natural characteristics of rain events being limited in spatial extension, according to the kind of rain present (stratiform and convective).

Chapter 3 is devoted to the description and comprehensive discussion of the model proposed by the authors to describe rain attenuation conditions for multiple users. A novel method to generate time series of rain attenuation has been presented. The method accurately reproduces the desired spatial correlation. A model for the time evolution of rain events is also introduced. The performance of the proposed method are assessed: single site attenuation statistics of first and second order are tested against reference models. The de-correlation index has been analyzed and a good agreement between the simulated and reference results has been found.

Chapter 4 explores the characteristics of the Reconfigurable Antenna system (OBDPA system) and ACM transmission techniques with application to the problem at hand. The OBDPA system is described as well as the dynamic optimization which aims at maximizing the worst SNIR over the service area. Ideal ACM transmission schemes aims at maximizing the system SE at any instant by the adapting the transmission format to the user SNIR condition. Consequently, the active fade compensation provided by OBDPA system has potential to increase the effectiveness of the ACM techniques.

In Chapter 5 we have applied the novel model for rain attenuation to the joint use of the OBDPA and ACM. The two FMTs are tested on real rain attenuation conditions described by meteorological data and simulated by the proposed model. The figure of merit to describe the transmission system performance is the user SNIR, evaluated considering the simulated rain attenuation and the optimized power radiation coefficients of the OBDPA.

The analysis presented here covers a single spot of the service area considered

for the multibeam satellite system. By general considerations regarding the whole service area, no significant variations are expected by the analysis of different spots, at least concerning the center part of the service area (spots on the margins are less subject to interference and are characterized by better user conditions simply by the antenna design).

The TS model for rain attenuation generates time series of rain attenuation values (with time resolution 1 sample/s) for multiple receiving stations in the service spot area, by adapting a single set of experimental rain attenuation measurements. It represents one of the few solutions to the problem of modelling concurrent rain attenuation conditions for multiple sites, with the unique characteristics of referring to a database of real acquired measurements. By the analysis of the obtained time series it has been observed that joint rain attenuation statistics among the simulated users are accurately reproduced, in terms of spatial correlation of rain attenuation and its time evolution, both on short and long term.

The model has been applied to generate “on-demand” rain attenuation conditions based on the real meteorological information used in the OBDPA system. The model allows to translate integral meteorological information into a time/space evolution of rain over the selected time period of 6 hours, with desired statistical features in terms of spatiotemporal correlation of rain. The application of the TS model to the OBDPA system allows to simulate the end users states of the system in terms of rain attenuation, gaining a new spatial and temporal resolution for the overall system analysis. The quite simple mathematical framework makes the model an efficient solution to simulate joint rain conditions over the 6-hours time intervals of the OBDPA system.

By investigating generated system performance traces, the effects of dynamic power adaptation in different transmission modes have been studied. When a feedback

link is not available (one directional communications), the CCM transmission may incur in temporary or complete outages (rain fades) for the users which do not achieve the required link closure SNIR in the observed period. In this scenario, the OBDPA results in reduced outage probability for the users not subject to high interference.

In the case when ACM is available, *i.e.* under the assumption of a complex feedback system, the obtained results show that the power adaptation effectively support ACM transmission schemes. When extra power margin is available, its effect coupled with ACM results in the following additional benefits, as applied to studied scenarios:

- reduced heavy fades in the 6 hours time (*i.e.* higher minimum user SE): gain in SE_{min} has been shown in $\approx 10\%$;
- higher ModCod index support: total probability of highest ModCod usage increased by 20% (stratiform rain) and 5% (multiple convective rain cells);
- reduced standard deviation of average throughput among users: -50% overall for stratiform rain case and -30% in convective rain for those users who benefits from the extra power allocated by OBDPA system.

From the analysis of the generated SNIR and SE time series in the selected scenarios, it can be observed that the system at high SNR might be limited by the inter-beam interference. A subset of users may incur in throughput reduction, while their availability is preserved by ACM transmission schemes. In order to improve the system performance, we presume that the OBDPA system optimization procedure may require additional ACM induced constraints.

The analysis here proposed and the generated results are developed on single meteorological events, thus are not exhaustive to get an overall performance

assessment of the OBDPA system. It appears also difficult to select a significant subset of different meteorological conditions to derive conclusive performance results. The two proposed meteorological situations previously discussed have been selected due to their rain characteristics in relationship with the OBDPA system. The techniques tested on those short studies can be directly applied to the investigation of long-term simulations, in order to take into account a large ensemble of meteorological conditions and to improve the understanding of the OBDPA system. This future development will be subject of a stand-alone study.

Considering the results discussed above, we believe that the developed methodology appears of great interest applied to the OBDPA and ACM, even for single meteorological conditions, for the possibility of assessing link and space availability of the different ModCods. The proposed methodology, able to simulate “on-demand” meteorological conditions, may be applicable the satellite system cross-layer scheduling analysis and simulation [76]. From this point of view, the generated rain attenuation conditions, with the proper spatiotemporal correlation, are a significant feature of the proposed modelling.

The methodology presented in this work is currently used to perform a long-term assessment of the joint use of the two presented techniques, in order to obtain more solid results in term of SNIR and SE gain.

References

- [1] F. Lacoste, “Modelisation de la dynamique du canal de propagation terre-espace en bandes ka et ehf,” Ph.D. dissertation, Supaero, Toulouse, France, 2005.
- [2] C. Capsoni (editor), “Verification of Propagation Impairment Mitigation Techniques,” ESA, The Netherlands, Final Report of the ESA/ESTEC Contract N.20887/07/NL/LvH, 2011.
- [3] —, “Assessment of propagation effects in the W frequency bands for space exploration,” ESA, The Netherlands, Final Report of the ESA/ESTEC Contract N.21317/07/NL/HE, 2011.
- [4] P. Mikonen, “Modern 60 GHz radio link.” in *29th European Microwave Conference*, 1999, pp. 83–86.
- [5] G. Timms, V. Kvicera, and M. Grabner, “60 GHz band propagation experiments on terrestrial paths in sydney and praha,” *Radioengineering*, vol. 14, no. 4, pp. 27–32, April 2005.
- [6] S. Bertorelli, C. Riva, and L. Valbonesi, “Generation of attenuation time series for simulation purposes starting from Italsat measurements,” *Antennas and Propagation, IEEE Transactions on*, vol. 56, no. 4, pp. 1094–1102, April 2008.
- [7] L. Ippolito, “Radio propagation for space communications systems,” *Proceedings of the IEEE*, vol. 69, no. 6, pp. 697–727, June 1981.
- [8] R. Stull, *An Introduction to Boundary-Layer Meteorology*. Kluwer Academic Publishers, 1988.
- [9] U. Government Printing Office, “U.S. Standard Atmosphere, Report number: NASA-TM-X-74335; NOAA-S/T-76-1562, 241p,” U.S. Government, Washington D.C., Tech. Rep., 1976.
- [10] ITU, “Recommendation ITU-R P.835-4 Reference Standard Atmospheres,” ITU, Geneva, P Series, 2005.
- [11] J. Van Vleck and V. Weisskopf, “On the shape of collision broadened lines,” *Rev. Mod. Phys.*, vol. 17, 1945.
- [12] H. Liebe, G. Hufford, and M. Cotton, “Propagation modelling of moist air and suspended water/ice particles at frequencies below 1000 Ghz,” in *AGARD 52nd*

- Specialists' Meeting of The EM Wave Propagation Panel*, Palma de Maiorca, Spain, 1993.
- [13] ITU, "Recommendation ITU-R P.676-9 Attenuation by Atmospheric Gases," ITU, Geneva, P Series, 2009.
- [14] E. Salonen, S. Karhu, S. Uppala, and R. Hyvonen, "Study of improved propagation predictions," Helsinki University of Technology and Finnish Meteorological Institute, Final Report ESA/ESTEC Contract 9455/91/NL/LC(SC), 1994.
- [15] ERA40, "ERA40," ITU, Geneva, Tech. Rep., 2009.
- [16] ITU, "Recommendation ITU-R P.840-5 Attenuation due to Clouds and Fog," ITU, Geneva, P Series, 2009.
- [17] L. Ippolito Jr., *Radiowave Propagation in Satellite Communications*. New York: Van Nostrand Reinhold Co., 1986.
- [18] G. Mie, *Ann. Physik*, vol. 25, p. 377, 1908.
- [19] J. Marshall and W. Palmer, "The distribution of raindrop with size," *Journal Meteorol.*, vol. 5, pp. 165–166, August 1948.
- [20] J. Joss and A. Waldvogel, "The variations of raindrop size distributions at locarno," in *Proc. of the Int. Conf. on Cloud Physics*, Toronto, Canada, 1968, pp. 369–373.
- [21] ITU, "Recommendation ITU-R P.838-3 Specific Attenuation Model for Rain for use in Prediction Methods," ITU, Geneva, P Series, 2005.
- [22] B. Arbesser-Rastburg and A. Paraboni, "European research on ka-band slant path propagation," *Proceedings of the IEEE*, vol. 85, no. 6, pp. 843–852, 1997.
- [23] A. Paraboni, A. Martellucci, C. Capsoni, and C. Riva, "The physical basis of atmospheric depolarization in slant paths in the v band: Theory, ITALSAT experiment and models," *Antennas and Propagation, IEEE Transactions on*, vol. 59, no. 11, pp. 4301–4314, 2011.
- [24] ITU, "Recommendation ITU-R P.618-10 Propagation data and prediction methods required for the design of Earth-space telecommunication systems," ITU, Geneva, P Series, 2009.
- [25] M. M. J. L. Van de Kamp, C. Riva, J. Tervonen, and E. Salonen, "Frequency dependence of amplitude scintillation," *Antennas and Propagation, IEEE Transactions on*, vol. 47, no. 1, pp. 77–85, 1999.

- [26] V. Tatarskii, *Wave Propagation in a Turbulent Medium*. New York: Mc Graw-Hill, 1961.
- [27] E. Matricciani and C. Riva, "18.7 Ghz tropospheric scintillation and simultaneous rain attenuation measured at Spino d'Adda and Darmstadt with ITALSAT," *Radio Science*, vol. 43, no. 1, 2008.
- [28] M. Filip and E. Vilar, "Optimum utilization of the channel capacity of a satellite link in the presence of amplitude scintillations and rain attenuation," *Communications, IEEE Transactions on*, vol. 38, no. 11, pp. 1958–1965, 1990.
- [29] ITU, "Recommendation ITU-R P.836-4 Water vapour: surface density and total columnar content," ITU, Geneva, P Series, 2009.
- [30] A. Martellucci (coordinator), "Radiowave propagation modelling for SatCom services at Ku-band and above," ESA Publications Division, The Netherlands, COST Action 255 Final Report, SP-1252, 2002.
- [31] ITU, "Recommendation ITU-R P.837-5 Characteristics of precipitation for propagation modelling," ITU, Geneva, P Series, 2007.
- [32] C. Capsoni, L. Luini, A. Praboni, C. Riva, and A. Martellucci, "A new prediction model of rain attenuation that separately accounts for stratiform and convective rain," *IEEE Transaction on Antennas and Propagation*, January 2009.
- [33] L. Feral, H. Sauvageot, L. Castanet, and J. Lemorton, "HYCELL - A new hybrid model of the rain horizontal distribution for propagation studies: Part 1, Modeling of the rain cell," *Radio Science*, vol. 38, no. 3, 2003.
- [34] E. Matricciani, "Global formulation of the Synthetic Storm Technique to calculate rain attenuation only from rain rate probability distributions," in *IEEE International Symposium on Antennas and Propagation*, San Diego, U.S., July 2008.
- [35] C. Riva (coordinator), "Characterisation and Modelling of Propagation Effects in 20-50 Ghz Band," ESA, The Netherlands, Final report for the European Space Agency under ESTEC Contract No. 17760/03/NL/JA, 2006.
- [36] M. M. G. D'Amico, A. R. Holt, and C. Capsoni, "An anisotropic model of the melting layer," *Radio Science*, vol. 33, no. 3, pp. 535–552, 1998. [Online]. Available: <http://dx.doi.org/10.1029/97RS03049>
- [37] DBSG3, "<http://www.itu.int/ITU-R/>," ITU, Geneva, Tech. Rep., 2012.
- [38] L. Luini and C. Capsoni, "Multiexcell: A new rainfall model for the analysis of the millimetre wave propagation through the atmosphere," in *Antennas and*

- Propagation, 2009. EuCAP 2009. 3rd European Conference on*, march 2009, pp. 1946–1950.
- [39] F. Valle, “Satellite broadband revolution: How latest Ka-band systems will change the rules of the industry. an interpretation of the technological trajectory,” in *Personal Satellite Services*, ser. Lecture Notes of the Institute for Computer Sciences, Social Informatics and Telecommunications Engineering. Springer Berlin Heidelberg, 2009, vol. 15, pp. 49–60. [Online]. Available: http://dx.doi.org/10.1007/978-3-642-04260-7_7
- [40] C. Avanti, “www.avantiplc.com,” aug. 2012.
- [41] F. J. Tapiador, F. Turk, W. Petersen, A. Y. Hou, E. Garcia-Ortega, L. A. Machado, C. F. Angelis, P. Salio, C. Kidd, G. J. Huffman, and M. de Castro, “Global precipitation measurement: Methods, datasets and applications,” *Atmospheric Research*, vol. 104,105, no. 0, pp. 70–97, 2012. [Online]. Available: <http://www.sciencedirect.com/science/article/pii/S0169809511003607>
- [42] O. Peters, C. Hertlein, and K. Christensen, “A complexity view of rainfall,” *Physical Review Letters*, vol. 88, no. 1, pp. 187 011–187 014, 2002, cited By (since 1996) 104. [Online]. Available: <http://www.scopus.com/inward/record.url?eid=2-s2.0-4043167503&partnerID=40&md5=266053858ad9345a657935cb4bcbaa71>
- [43] O. Peters and K. Christensen, “Rain: Relaxations in the sky,” *Physical Review E*, vol. 66, no. 3, pp. 036 120/1–036 120/9, 2002, cited By (since 1996) 39. [Online]. Available: <http://www.scopus.com/inward/record.url?eid=2-s2.0-0-37649031329&partnerID=40&md5=0735292713b15795f3be078250c4680c>
- [44] S. Primak, V. Lyandres, and V. Kontorovich, “Markov models of non-gaussian exponentially correlated processes and their applications,” *Phys. Rev. E*, vol. 63, p. 061103, May 2001.
- [45] N. Jeannin, L. Feral, H. Sauvageot, L. Castanet, and F. Lacoste, “A large-scale space-time stochastic simulation tool of rain attenuation for the design and optimization of adaptive satellite communication systems operating between 10 and 50 Ghz,” *International Journal of Antennas and Propagation*, vol. 2012, 2012, article ID 749829.
- [46] G. Carrie, F. Lacoste, and L. Castanet, “A new ‘event-on-demand’ synthesizer of rain attenuation time series at ku-, ka- and q/v-bands,” *International Journal of Satellite Communications and Networking*, vol. 29, no. 1, pp. 47–60, 2011. [Online]. Available: <http://dx.doi.org/10.1002/sat.951>
- [47] S. Callaghan and E. Vilar, “Fractal generation of rain fields: synthetic realisation for radio communications systems,” *IET microwaves, antennas & propagation*, vol. 1, no. 6, pp. 1204–1211, 2007.

- [48] K. S. Paulson and X. Zhang, "Simulation of rain fade on arbitrary microwave link networks by the downscaling and interpolation of rain radar data," *Radio Science*, vol. 44, no. 2, 2009.
- [49] G. Karagiannis, A. Panagopoulos, and J. Kanellopoulos, "Multidimensional rain attenuation stochastic dynamic modeling: Application to earth-space diversity systems," *Antennas and Propagation, IEEE Transactions on*, vol. 60, no. 11, pp. 5400–5411, November 2012.
- [50] T. Maseng and P. Bakken, "A stochastic dynamic model of rain attenuation," *Communications, IEEE Transactions on*, vol. 29, no. 5, pp. 660–669, May 1981.
- [51] M. Cheffena, L. Braten, and T. Ekman, "On the space-time variations of rain attenuation," *Antennas and Propagation, IEEE Transactions on*, vol. 57, no. 6, pp. 1771–1782, June 2009.
- [52] G. Carrie, L. Castanet, and F. Lacoste, "Validation of rain attenuation time series synthesizers for temperate area - on the enhanced maseng-bakken model," in *Satellite and Space Communications, 2008. IWSSC 2008. IEEE International Workshop on*, 2008, pp. 40–44.
- [53] ITU, "Recommendation ITU-R P.1853 Tropospheric Attenuation Time Series Synthesis," ITU, Geneva, P Series, 2009.
- [54] A. Paraboni and F. Barbaliscia, "Multiple site attenuation prediction models based on the rainfall structures for advanced tlc or broadcasting systems," in *presented at the URSI 27th GA*, Maastricht, The Netherlands, August 2002.
- [55] S. Bertorelli and A. Paraboni, "Simulation of joint statistics of rain attenuation in multiple sites across wide areas using Italsat data," *Antennas and Propagation, IEEE Transactions on*, vol. 53, no. 8, pp. 2611 – 2622, aug. 2005.
- [56] C. Riva, "Seasonal and diurnal variations of total attenuation measured with the ITALSAT satellite at Spino d'Adda at 18.7, 39.6 and 49.5 Ghz," *International Journal of Satellite Communications and Networking*, vol. 22, no. 4, pp. 449–476, 2004. [Online]. Available: <http://dx.doi.org/10.1002/sat.784>
- [57] C. Aletti and M. Semmoloni, "Studio della funzione di autocorrelazione delle serie temporali di attenuazione dovuta a pioggia misurate col satellite ITALSAT nell'anno 1994 a 18.7 Ghz," Ph.D. dissertation, Politecnico di Milano, Milan, Italy, 2003.
- [58] D. Middleton, *An Introduction to Statistical Communication Theory*. New York: McGraw Hill Book Company, 1960.

- [59] J. Van Vleck and D. Middleton, "The spectrum of clipped noise," *Proceedings of the IEEE*, vol. 54, no. 1, pp. 2 – 19, jan. 1966.
- [60] M. Abramowitz and I. A. Stegun, *Handbook of Mathematical Functions with Formulas, Graphs, and Mathematical Tables*, 9th ed. New York: Dover, 1972.
- [61] B. Gremont and M. Filip, "Spatio-temporal rain attenuation model for application to fade mitigation techniques," *Antennas and Propagation, IEEE Transactions on*, vol. 52, no. 5, pp. 1245–1256, May 2004.
- [62] S. Kanellopoulos, A. Panagopoulos, and J. Kanellopoulos, "Calculation of the dynamic input parameter for a stochastic model simulating rain attenuation," *Antennas and Propagation, IEEE Transactions on*, vol. 55, no. 11, pp. 3257–3264, November 2007.
- [63] V. Primak, S. Kontorovich and V. Lyandres, *Stochastic Methods and Their Applications to Communications: Stochastic Differential Equations Approach*. Chichester, Uk: John Wiley and Sons, 2005.
- [64] A. Paraboni, F. Barbaliscia, C. Capsoni, and C. Riva, "Small and large scale spatial distribution of precipitation," in *presented at the URSI 27th GA*, Maastricht, The Netherlands, August 2002.
- [65] A. Benarroch, P. Garcia del Pino, and J. Riera, "Spatial properties of cloud cover and rainfall rate based on data from spanish sites," in *Antennas and Propagation, 2006. EuCAP 2006. First European Conference on*, nov. 2006, pp. 1 –8.
- [66] L. Luini and C. Capsoni, "Estimating the spatial cumulative distribution of rain from precipitation amounts," *Radio Science*, vol. 47, no. 1, pp. n/a–n/a, 2012. [Online]. Available: <http://dx.doi.org/10.1029/2011RS004832>
- [67] ITU, "Recommendation ITU-R P.1623 Prediction method for fade dynamics on earth-space paths," ITU, Geneva, P Series, 2003.
- [68] —, "Recommendation ITU-R P.311-12 Acquisition, Presentation and Analysis of Data in Studies of Tropospheric Propagation," ITU, Geneva, P Series, 2005.
- [69] A. Paraboni, M. Buti, C. Capsoni, D. Ferraro, C. Riva, A. Martellucci, and P. Gabellini, "Meteorology-driven optimum control of a multibeam antenna in satellite telecommunications," *Antennas and Propagation, IEEE Transactions on*, vol. 57, no. 2, pp. 508 –519, feb. 2009.
- [70] P. Thompson, B. Evans, L. Castenet, M. Bousquet, and T. Mathiopoulos, "Concepts and technologies for a terabit/s satellite," in *SPACOMM 2011, The Third International Conference on Advances in Satellite and Space Communications*, 2011, pp. 12–19.

- [71] D. Alvaro, M. Luccini, and C. Capsoni, "Advanced time series synthesizer for simulation of joint rain attenuation conditions: simulation of Gateways in smart site diversity at Q/V bands," in *presented at URSI Commission F Triennial Symposium on Radiowave Propagation and Remote Sensing*, Ottawa, April 2013.
- [72] P. Gabellini, N. Gatti, C. Capsoni, L. Resteghini, A. Martellucci, and P. Rinous, "An on-board reconfigurable antenna system for ka-band broadcasting satellite services," in *Antennas and Propagation (EUCAP), 2012 6th European Conference on*. IEEE, 2012, pp. 2636–2640.
- [73] ECMWF, "ECMWF library," Technical and Scientific Documentation, 2009. [Online]. Available: <http://www.ecmwf.int/>
- [74] ESA, "Reconfigurable Ka-Band Antenna Front End for Active Rain Fade Compensation; Propagation Modelling," ESA, Final Report ESA contract N 17877/04/NL/JA, 2007.
- [75] R. Rinaldo and R. D. Gaudenzi, "Capacity analysis and system optimization for the forward link of multi-beam satellite broadband systems exploiting adaptive coding and modulation," *International Journal of Satellite Communications and Networking*, vol. 22, no. 3, pp. 401–423, 2004. [Online]. Available: <http://dx.doi.org/10.1002/sat.789>
- [76] M. Castro and G. Granados, "Cross-layer packet scheduler design of a multi-beam broadband satellite system with adaptive coding and modulation," *Wireless Communications, IEEE Transactions on*, vol. 6, no. 1, pp. 248–258, 2007.
- [77] S. Cioni, R. De Gaudenzi, and R. Rinaldo, "Channel estimation and physical layer adaptation techniques for satellite networks exploiting adaptive coding and modulation," *International Journal of Satellite Communications and Networking*, vol. 26, no. 2, pp. 157–188, 2008. [Online]. Available: <http://dx.doi.org/10.1002/sat.901>
- [78] ETSI, "Digital Video Broadcasting (DVB): Second generation framing structure, channel coding and modulation system for broadcasting, interactive services, news gathering and other broadband satellite applications," ETSI, EN 302 307 v1.1.1, 2005.
- [79] E. Albery, S. Defever, C. Moreau, R. De Gaudenzi, S. Ginesi, R. Rinaldo, G. Gallinaro, and A. Vernucci, "Adaptive coding and modulation for the dvb-s2 standard interactive applications: capacity assessment and key system issues," *Wireless Communications, IEEE*, vol. 14, no. 4, pp. 61–69, 2007.
- [80] K. Baddour and N. Beaulieu, "Autoregressive modeling for fading channel simulation," *Wireless Communications, IEEE Transactions on*, vol. 4, no. 4, pp. 1650–1662, July 2005.

-
- [81] A. N. Pettitt, I. S. Weir, and A. G. Hart, "A conditional autoregressive gaussian process for irregularly spaced multivariate data with application to modelling large sets of binary data," *Statistics and Computing*, vol. 12, pp. 353–367, 2002, 10.1023/A:1020792130229. [Online]. Available: <http://dx.doi.org/10.1023/A:1020792130229>
- [82] I. Mitola, J. and J. Maguire, G.Q., "Cognitive radio: making software radios more personal," *Personal Communications, IEEE*, vol. 6, no. 4, pp. 13–18, aug 1999.
- [83] S. M. Almalfouh and G. L. Stuber, "Interference-aware power allocation in cognitive radio networks with imperfect spectrum sensing," in *Communications (ICC), 2010 IEEE International Conference on*, May 2010, pp. 1–6.
- [84] C. E. Dangerfield, D. Kay, and K. Burrage, "Modeling ion channel dynamics through reflected stochastic differential equations," *Phys. Rev. E*, vol. 85, p. 051907, May 2012. [Online]. Available: <http://link.aps.org/doi/10.1103/PhysRevE.85.051907>
- [85] I. Bruce, "Evaluation of stochastic differential equation approximation of ion channel gating models," *Annals of Biomedical Engineering*, vol. 37, pp. 824–838, 2009, 10.1007/s10439-009-9635-z. [Online]. Available: <http://dx.doi.org/10.1007/s10439-009-9635-z>
- [86] Y. Gao and R. Billinton, "Adequacy assessment of generating systems containing wind power considering wind speed correlation," *Renewable Power Generation, IET*, vol. 3, no. 2, pp. 217–226, June 2009.

Appendix A

On the Correlation Characteristics of Binary Random Processes

A.1 Introduction

The motivations for the study here reported rose during the development of a model to generate time series of rain attenuation for multiple sites on a large geographical area. The model under development is based on two independent processes, one assigning rain times (basic period of fixed length of 1 hour) and the second assigning rain attenuation sequences. Dealing with multiple sites, the interest of the model is firstly to reproduce the spatial/temporal variation of rain attenuation sequences.

Information of the spatial correlation of rain times and intensity are found in [24], especially the description of the probability of concurrent rain over different sites and its correlation, dependent on distance.

In the framework of the model, the following process was developed in order to assign rainy and not rainy times. Considering N stations randomly placed in the reference geographical area, the state of the N stations at each time is described by means of an N -dimensional binary variable which defines the condition “rainy” or “not rainy”, with the associated multi-variate probability function.

The state is assigned by means of the probability density of an N -dimensional continuous variable r_i , with $i = 1, \dots, N$, and by an N dimensional thresholds t_i , chosen according to the correlated probability of rain for each location. The continuous “rain state variable” r_i for the i^{th} location can be selected with a high degree of freedom.

The assumption here is a Gaussian multi-variate variable normalized to zero mean and unit variance, with covariance matrix imposed to represent the desired joint statistics presented in [24]. The rain assigning process, tested on a long time, must reproduce the rain probability P_0 of each single station, as well as the space correlation of rainy and not-rainy events among the N stations set

The threshold t_i , which defines whether the condition on the site is “rainy” or “not rainy”, is chosen to fulfill:

$$P(t_i) = \int_{-\infty}^{t_i} p(r_i) dr_i = 1 - P_{0,i}, \quad (\text{A.1})$$

where $P_{0,i}$ is the probability of having rain in the i^{th} stations. According to the variable r_i and the set threshold t_i , a binary process z_i is obtained to describe rainy conditions:

$$z_i = T_z(r_i) = \begin{cases} 1 : r_i > t_i \\ 0 : r_i < t_i \end{cases}, \quad (\text{A.2})$$

The hard threshold imposed to the continuous variable is actually a non-linear transformation T_z , which results in a binary process in which 1 corresponds to a rainy hour, 0 to a non-rainy hour.

It was found that the non-linear transformation T_z has a significant effect on the correlation characteristics of the resulting process z_i . Fig. A.1 shows the correlation of the input continuous variables and the one obtained after the clipping process, which is sensibly lower than expected.

In the framework of the time series model, we are interested in imposing the correct correlation to the binary sequences z_i obtained from the transformation T_z . Consequently, defining the output process the one after the non-linear transformation,

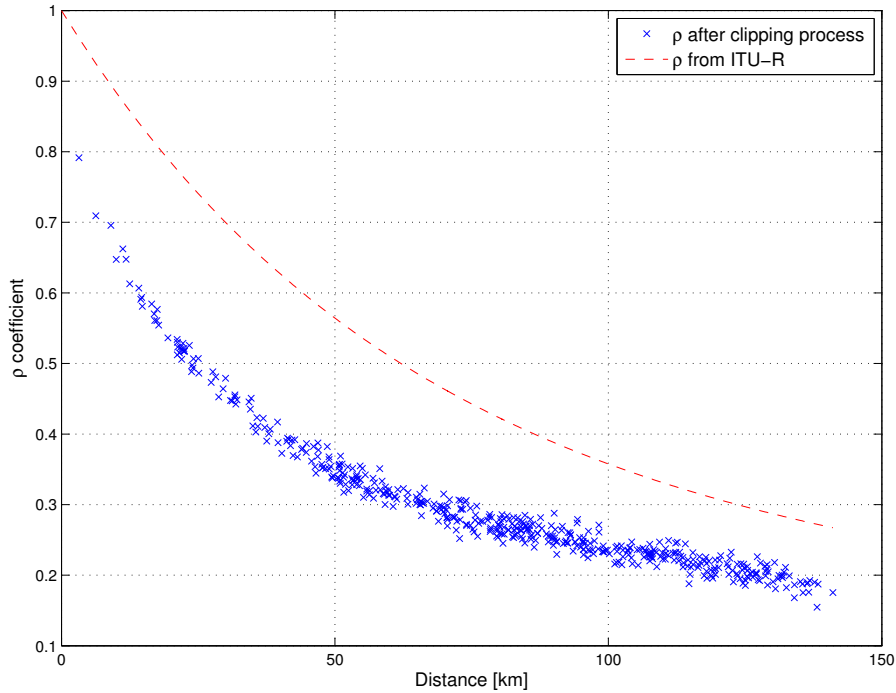


Figure A.1: Correlation of the random noise sequences and resulting correlation after clipping

the correlation of the input process r_i must be derived from the knowledge of the desired correlation of the output process z_i , which describes the rain events.

This issue could be solved by referring to the general theory of noise clipping, deeply discussed in [58,59]. Particularly, the correlation of a random Gaussian process after the non-linear transformation is the topic discussed in this work. Starting from the general results about the spectrum of clipped noise, the case arisen in the model development is addressed here. The solution to this particular case is derived by the use of a series expansion of results in [58,59]. The proposed series expansion allows one to invert the effect of the non-linear transformation, deriving the correct input correlation for a given target function after clipping.

The proposed solution is discussed in terms of its accuracy in reproducing the

target function. The dependence of the result on the order of the series expansion and the threshold used for clipping is also addressed. Finally, this study is applied to the problem exposed above, obtaining the correct correlation among the binary random sequences generated by the transformation T_z

A.2 Second-moment function of a clipped process and the Normal Surface

Referring to [58], given a random process y , the non-linear transformation T_z under analysis can be represented by:

$$z = T_g(y) = \begin{cases} \beta(y - t_s)^v : & y > t_s \\ 0 : & y < t_s \end{cases}, \quad (\text{A.3})$$

which relates the dynamic characteristics between input y and output z processes. β is an appropriate scale factor and t_s is the specific clipping threshold. Clearly, different threshold values leads to different clipping processes. According to [58], the second-moment function of the output is specifically:

$$M_z(t) = \mathbf{E}\{z_1 z_2\} = \frac{\beta^2 \Psi^{-1}}{2\pi} (1-k^2)^{-1/2} \int_0^\infty \int_0^\infty y_1^v y_2^v \exp^{-(y_1^2 + y_2^2 - 2y_1 y_2 k)/2\Psi(1-k^2)} dy_1 dy_2 \quad (\text{A.4})$$

where $\Psi = \overline{y_1^2} = \overline{y_2^2}$ and $k = k(t)$ is the normalized covariance function of a broadband input noise process.

The equivalent result is found in [59], which refers to the statistical concept of *Normal Surface*. In noise problems, we can take X and Y to be the unclipped

amplitude in two moments of time, respectively at $t = 0$ and $t = t_1$. Then, $r(t)$ is the correlation function of the unclipped noise. Statistical reasoning is justified since the noise distribution is Gaussian with zero mean and unit variance. If a distorting apparatus is present, i.e. a clipper, such that after distortion the amplitude is $f(X)$ rather than X , then the resulting correlation function is given by:

$$R_z(t) = \frac{1}{2\pi(1-r^2)}^{1/2} \int_{-\infty}^{\infty} \int_{-\infty}^{\infty} f(X)f(Y) \exp\left(-\frac{X^2+Y^2-2rXY}{2(1-r^2)}\right) dXdY \quad (\text{A.5})$$

In both Eq. A.4 and A.5 the correlation after the clipping process depends on the integral of a bi-dimensional PDF of the variables involved, which appears to be the key point of the expressions.

If the processes involved are Gaussian, the integral of the bi-dimensional Gaussian PDF could be solved analytically only for those limits which take advantage of the PDF symmetry. This is the case of extreme clipping, which involves the function $f(X)$ in Eq. A.5 defined as:

$$f(X) = 1, \quad (X > 0); \quad f(X) = -1, \quad (X < 0) \quad (\text{A.6})$$

Assuming a normalization such that after clipping the variance of the process is unity,

Eq. A.5 becomes:

$$\begin{aligned}
 R(t) = & \frac{1}{2\pi(1-r^2)}^{1/2} \left[\int_0^\infty \int_0^\infty \exp^{-\alpha} dXdY \right. \\
 & + \int_{-\infty}^0 \int_{-\infty}^0 \exp^{-\alpha} dXdY \\
 & - \int_0^\infty \int_{-\infty}^0 \exp^{-\alpha} dXdY \\
 & \left. - \int_{-\infty}^0 \int_0^\infty \exp^{-\alpha} dXdY \right], \tag{A.7}
 \end{aligned}$$

where

$$\alpha = (X^2 + Y^2 - 2rXY)/2(1-r^2). \tag{A.8}$$

The integration in polar coordinates $X = \rho \cos \phi$, $Y = \rho \sin \phi$ brings to the result [59]:

$$R(t) = \frac{2(1-r^2)^{1/2}}{\pi} \int_0^{\pi/2} \frac{d\phi}{1-r \sin 2\phi} - 1 = \frac{2}{\pi} \sin^{-1}(r) \tag{A.9}$$

which describe the relationship between the input correlation r and the output correlation after the clipping process in Eq. A.6.

In order to assess the effect of different clipping function, especially the one of interest for this work, there is the need to evaluate the integral of the *Normal Surface* for limits different from 0 or ∞ . This leads to the issue of representing the integral of the PDF in such a way to allow its evaluation. Specifically, we look for a representation to be inverted to derive the correct correlation to impose to the input process given the desired correlation of the output binary sequences. To solve this

task one could expand the PDF by means of a proper series of orthogonal functions.

A.3 Orthogonal expansion of probability densities: the Edgeworth series

In practical cases one has to deal with a probability density $p_1(x)$ which looks similar to a Gaussain on defined by Eq.

$$p(x) = N(x, m, \sigma) = \frac{1}{\sqrt{2\pi}\sigma} \exp \left[- \left(\frac{x - m}{\sigma} \right)^2 \right] \quad (\text{A.10})$$

Two Characteristics features of such distributions can be summarized as follows:

1. Unimodality, i.e. the PDF has a single maximum, and
2. The PDF has tails extending to infinity on both sides of the maximum, which decay fast when the magnitude of the argument approaches infinity.

In this case it is always possible to approximate such PDFs using a series of Hermitian or Laguerre polynomials.

A.3.1 The Edgeworth Series

The possibility of expanding a general function by a series of terms is mainly driven by the necessity of simplify calculations. In this case a PDF $p(x)$ under consideration is approximated by the following series:

$$p(x) = p_0(x) \sum_{n=0}^{\infty} \frac{1}{n!} \frac{b_n}{\sigma^n} H_n \left(\frac{x - m}{\sigma} \right) \quad (\text{A.11})$$

where $p_0(x)$ is the Gaussian PDF in Eq. A.10 with mean value m and variance σ^2 and $H_n(z)$ stands for the Hermitian polynomials [60].

A.3.2 Rodrigues formula and Hermite polynomials

Hermitian polynomials, named after the French mathematician Charles Hermite (1822 - 1901), is a family of polynomial functions which is the solution of a special case of differential equation appearing in the analysis of harmonic oscillators in quantum mechanics. They appear in the Edgeworth series because they can be used to evaluate the n^{th} order partial differential equation of a Gaussian kernel. By recalling Eq. A.19, it appears clear how Hermitian polynomials are related to the solution of the considered problem.

Referring to the Rodrigues formula [60], Hermitian polynomials are defined as:

$$H_n(z) = (-1)^n \exp\left[\frac{z^2}{2}\right] \frac{d^n}{dz^n} \exp\left[-\frac{z^2}{2}\right] \quad n = 0, 1, \dots \quad (\text{A.12})$$

Hermitian polynomials are orthogonal with weight $p_0(x)$, i.e.

$$\int_{-\infty}^{\infty} H_n(z) H_m(z) p_0(z) dz = n! \delta_{m,n} = \begin{cases} n! & m = n \\ 0 & m \neq n \end{cases}, \quad (\text{A.13})$$

the coefficients b_n in Eq. A.11 can be calculated as:

$$b_n = \sigma^n \int_{-\infty}^{\infty} p(x) H_n\left(\frac{x-m}{\sigma}\right) dx = \sigma^n \mathbf{E} \left[H_n\left(\frac{x-m}{\sigma}\right) \right] \quad (\text{A.14})$$

This expansion is based on the theorem of functional analysis reported in [63], which states that if $p(x)$ is an arbitrary function such that:

$$\int_{-\infty}^{\infty} |p(x)|^2 dx < \infty \quad (\text{A.15})$$

then

$$\lim_{N \rightarrow \infty} \int_{-\infty}^{\infty} \left| p(x) - p_0(x) \sum_{n=0}^{\infty} \frac{1}{n!} \frac{b_n}{\sigma^n} H_n \left(\frac{x-m}{\sigma} \right) \right|^2 dx = 0 \quad (\text{A.16})$$

In practice the function $p(x)$ is known only with a certain degree of accuracy. Thus, the sum in Eq. A.11 can be truncated after a finite number N of terms. The number N depends on the values of m, σ of the target distribution.

According to these literature results, it is reasonable to expand the expression of the *Normal Surface* according to the Rodrigues formula in Eq. A.12. Then the resulting series could be inverted to obtain the correct correlation to impose to the initial process

A.4 Hard thresholding problem

In this section we focus on the problem of the extreme clipping of a noise sequence [59] for a given threshold. The clipping result is a binary sequence defined as follows. Given a standard process y with a specific correlation $r_y(\tau)$, the non linear transformation in this case is given by:

$$z = T_g(y) = \begin{cases} 1 : & y > t_s \\ 0 : & y < t_s \end{cases}, \quad (\text{A.17})$$

which generates a binary sequence with a new correlation function $R_z(\tau)$.

In the case of the considered transformation, Eq. A.4 is approximated by the series [63]:

$$R_z(\tau) = \frac{1}{\sigma^2} \sum_{n=1}^{\infty} \left\{ \int_{-\infty}^{\infty} g(\xi) \Phi^{n+1} \left(\frac{\xi}{\sigma} \right) d\xi \right\}^2 \frac{r^n(t)}{n} \quad (\text{A.18})$$

in which the term Φ^{n+1} represents the n^{th} derivative of the Gaussian distribution, i.e.

$$\Phi^{n+1}(z) = \frac{\partial^n}{\partial z^n} \left(\frac{1}{\sqrt{2\pi}} \exp -\frac{1}{2}z^2 \right) \quad (\text{A.19})$$

Expression A.19 involves the n^{th} derivative of a Gaussian kernel, which can be conveniently represented by *Rodrigues* formula [60] and Hermite Polynomials.

The clipping threshold enters directly as the limit of the integral in Eq. A.18. Before considering a general clipping threshold t_s , it is useful to address the case for $t_s = 0$. This is a special case since the threshold of transformation is equal to the mean value of the original noise sequence. The integral expressed by Eq. A.4 is symmetrical with respect to the mean value of the variable distribution and can be solved in a closed form. Specifically, referring to Eq. A.18, we have:

$$\begin{aligned} R_z(\tau) &= \frac{1}{\sigma^2} \sum_{n=1}^{\infty} \left\{ \int_{-\infty}^{\infty} g(\xi) \Phi^{n+1} \left(\frac{\xi}{\sigma} \right) d\xi \right\}^2 \frac{r_y(\tau)^n}{n} \\ &= \frac{1}{\sigma^2} \sum_{n=1}^{\infty} \left\{ \int_0^{\infty} 1 \Phi^{n+1} \left(\frac{\xi}{\sigma} \right) d\xi \right\}^2 \frac{r_y(\tau)^n}{n} \\ &= \frac{1}{\sigma^2} \sum_{n=1}^{\infty} \{ \Phi^n(\infty) - \Phi^n(0) \}^2 \frac{r_y(\tau)^n}{n} \end{aligned} \quad (\text{A.20})$$

The use of Rodrigues formula [60] allows to express $\Phi^n(x)$ as:

$$\Phi^n(x) = \frac{\partial^{n-1}}{\partial x^{n-1}} w(x) = (-1)^n \left(\frac{1}{\sigma\sqrt{2}} \right)^{n-1} H_{n-1} \left(\frac{x}{\sigma\sqrt{2}} \right) w(x); \quad (\text{A.21})$$

with $w(x)$ being the Gaussian distribution $w(x) = \frac{1}{\sqrt{2\pi}} \exp \left\{ -\frac{x^2}{2} \right\}$;

In this particular case, the closed form solution of the integral is given by [63]:

$$R_z(\tau) = \frac{1}{\sigma^2} \sum_{n=1}^{\infty} |\Phi^n(0)|^2 \frac{r_y(\tau)^n}{n!} = \frac{1}{2\pi} \int_0^R \frac{dx}{\sqrt{1-x^2}} = \frac{2}{\pi} \sin^{-1} r_y(\tau); \quad (\text{A.22})$$

which is the same result obtained by the use of the normal surface in [59]. This particular result is useful to assess the quality of the polynomial representation, especially to assess the necessary number of terms in the series to well represent the original correlation $r_y(\tau)$.

For thresholds different from $t_s = 0$ no close expressions are present for the value of the integral in Eq. A.18. On the other hand, Eq. A.18 is general for any clipping threshold t_s : the value of the integral can be obtained with arbitrary accuracy using the series expansion according to Eq. A.16.

A.5 Numerical Simulations

In this section the results previously described are implemented. The original stationary process $y(d)$ is a random sequence with exponential correlation, i.e.

$$r_y(d) = \exp -\frac{d}{D_0} \quad (\text{A.23})$$

where τ_0 represents the correlation interval. The problem of interest involves a spatial correlation, D_0 can be considered as the correlation distance.

Given a broadband noise process, the first goal is to generate a random process with the desired correlation function in Eq. A.23. Referring to the work in [80], a simple AR filter was used to impose the correct correlation to a white Gaussian process, with zero mean and unit variance. The estimation of the correlation of the generated process requires attention. The quality of the estimation is dependent of the number of independent samples available, leading to the need of simulating process samples for large multiples of the correlation interval D_0 . Averaging different realizations must be introduced, leading to the definition of a variance of correlation function σ_{r_y} .

As explained in the previous section, the output correlation can be approximated by a series expansion of n terms involving the input correlation $r_y(d)^n$ and a set of weights based on Hermitian polynomials, as in Eq. A.20 and Eq. A.21.

We considered a first example with threshold $t_s = 0$. Since random gaussian processes with zero mean are used as input, this first threshold corresponds to clipping at the mean value of the process. Eq. A.22 allows to have an analytical reference to assess the accuracy of the expansion of $R_z(\tau)$, the process correlation after clipping. Given the threshold $t_s = 0$, $\Phi^n(0)$ can be expressed by Hermite polynomials $H_{en}(0)$ according to the Rodrigues formula. The value of $H_{en}(0)$ is given by [60]:

$$H_n(0) = \begin{cases} (-1)^m \frac{(2m!)}{m!} : & n = 2m \\ 0 : & n = 2m + 1 \end{cases}, \quad (\text{A.24})$$

from which results that odd terms of the series are equal to 0.

The following figures show the obtained correlation after clipping, compared

with the expected \sin^{-1} function in Eq. A.22.

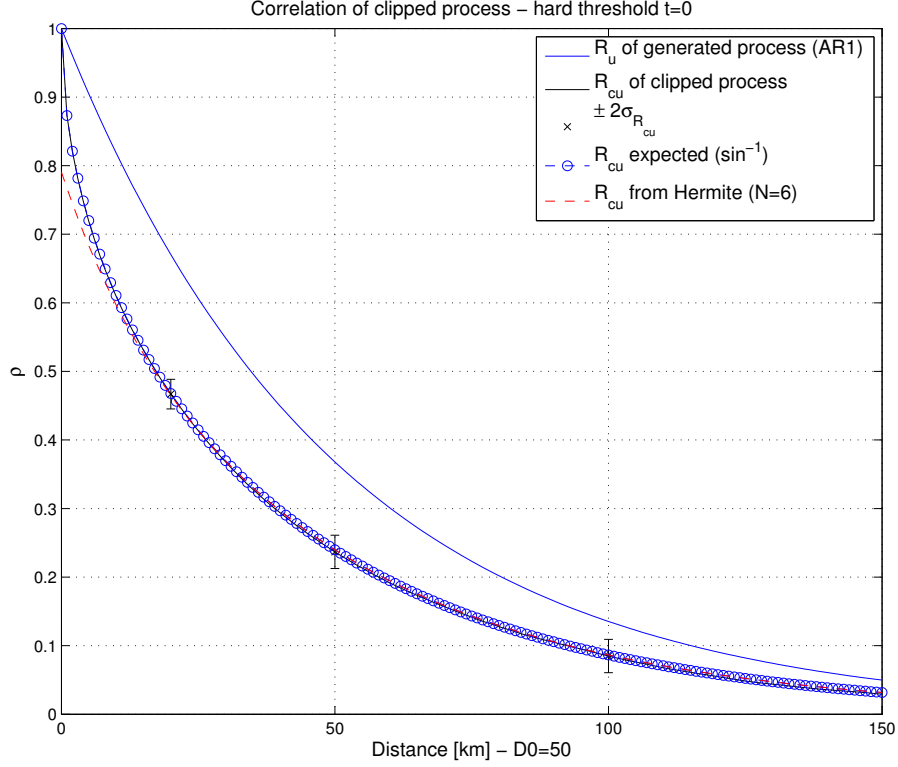


Figure A.2: Approximation of clipped process correlation (output) by Hermitian series expansion of order $N = 6$. Note the slow convergence at correlation values close to 1

Figure A.2 shows the original exponential correlation, the expected correlation after hard thresholding as from Eq. A.22, the correlation of the clipped generated process with its error deviation $\pm 2\sigma_{r_y}$, and the results of the series expansion with Hermite polynomials in Eq. A.18. The series expansion converges fast for high values of distance lags, the convergence at lag 0 requires instead a large number of elements in the series. This is expected, since for small distances coefficients are close to 1. Fig. A.3 shows the approximation error as function of distance and the expansion order N . Convergence is quite fast except from the very beginning, the accuracy

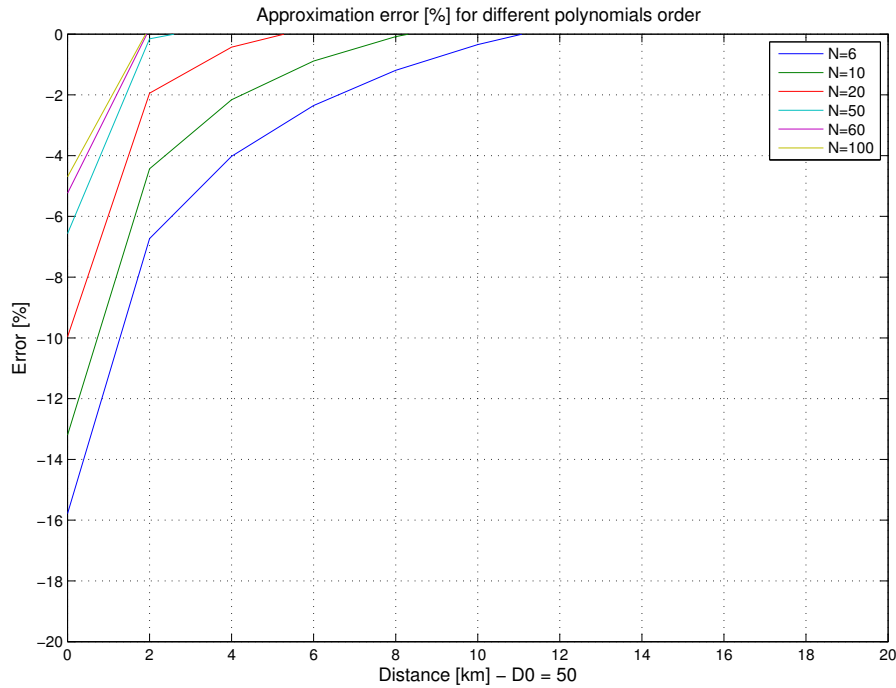


Figure A.3: Estimated Correlation at threshold 0

increases sensibly up to $N = 50$, slowing its progress for larger N . A reasonable error is already obtained with few elements ($N = 6$) and it is definitely acceptable for $N \geq 20$.

A set of threshold different from for the non-linear transformation is then defined. These thresholds define the value above which the input random process is assigned to a value 1 of the output binary sequence. In order to assess the effect of the clipping process, three thresholds are defined equal to $0, \sigma, 2\sigma$. The effect of clipping at different thresholds is shown in Fig. A.4. Given the input correlation, the greater the threshold the larger is the effect on the correlation of output binary sequence. This is reasonable since an higher threshold generates few “ones” in the output sequence and the importance of those ones in the correlation evaluation becomes higher: a little difference in the number of “ones” has a large effect on the

correlation evaluation. This is also confirmed by the results described in [58] about the spectrum of clipped noise at different thresholds (recalling the strong relationship between spectrum and correlation).

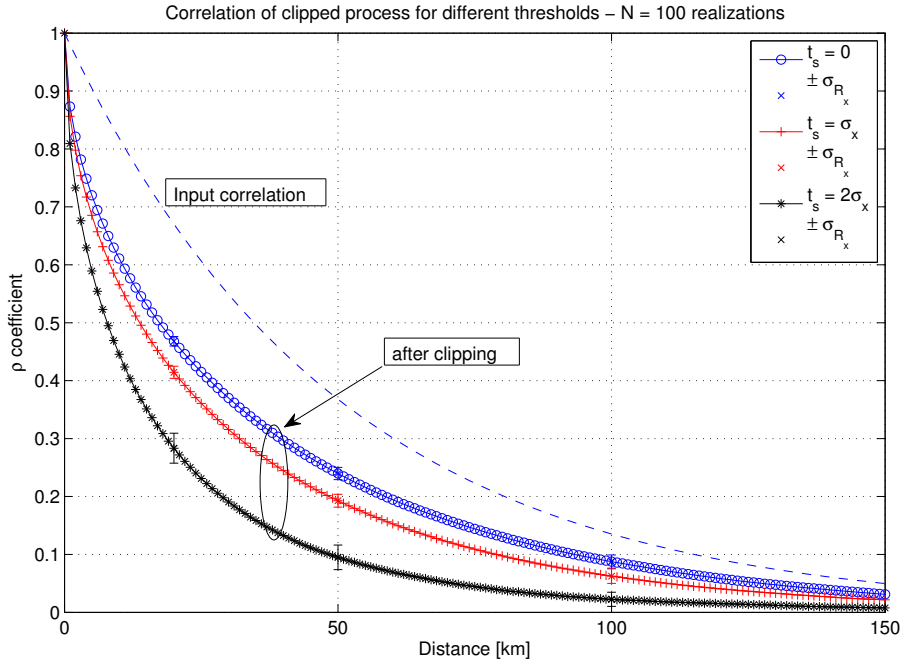


Figure A.4: Output correlation of clipped process for three different thresholds: $0, \sigma, 2\sigma$

A better accuracy for correlation values close to 1 is achieved by an higher number of terms in the expansion. Considering a threshold of 2σ , which results in a strong effect on output correlation, Fig. A.5 shows the convergence of the series for different expansion orders: $N = 6, 10, 20$. The percentage error evaluated with the reference curve is shown in Fig. A.6. Both figures are a zoom on small distances $1 - 50$ km which is the area of slower convergence.

Must be taken into consideration that increasing the expansion order leads to numerical and computational difficulties due to the presence of Hermitian polynomials of order N (which grow fast) and the need to evaluate $N!$ to scale them. Approxima-

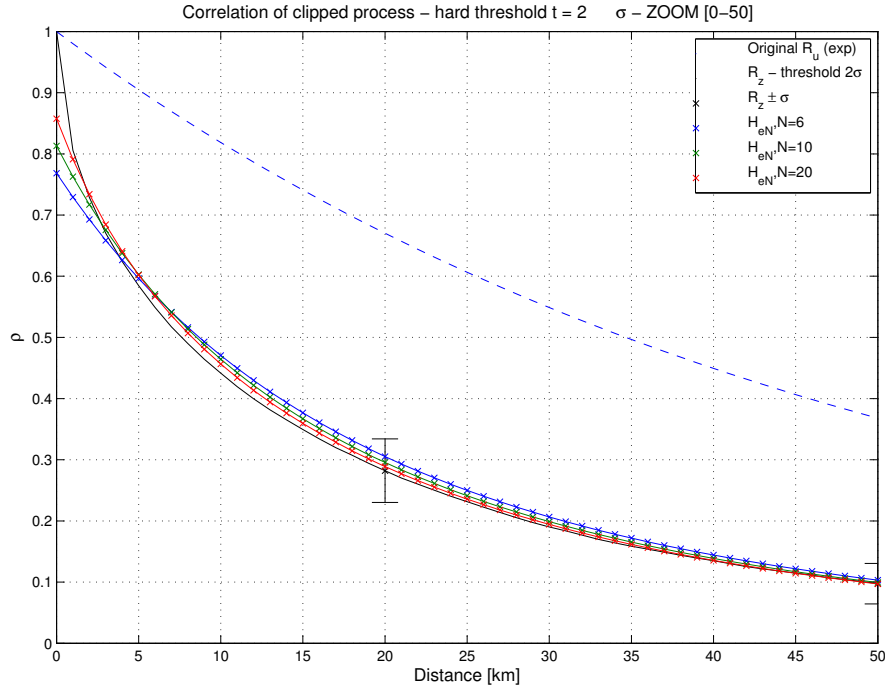


Figure A.5: Convergence for different expansion order: $N = 6, 10, 20$

tions of Hermitian polynomials can be found in [60] only for special cases. Moreover, the error at distance 0 appears to be reasonable already at order $N = 20$ as clear from Fig. A.6, leading to the choice of this order of expansion for the purposes of this work.

Once the accuracy of the series expansion is assessed for a fixed N , we want to solve the inverse problem of deriving the input correlation given a desired output correlation imposed to the binary sequences. This problem can be seen as a pre-filtering operation to correct the effect of the clipping process between the input and output series. Given the series expansion, this means to solve a N^{th} order equation in which the unknown variable is the input correlation at a specific distance d .

Referring to the case of threshold $t_s = 0$, thanks to the symmetry of the Gaussian PDF with zero mean, the integral of the PDF can be easily solved analytically

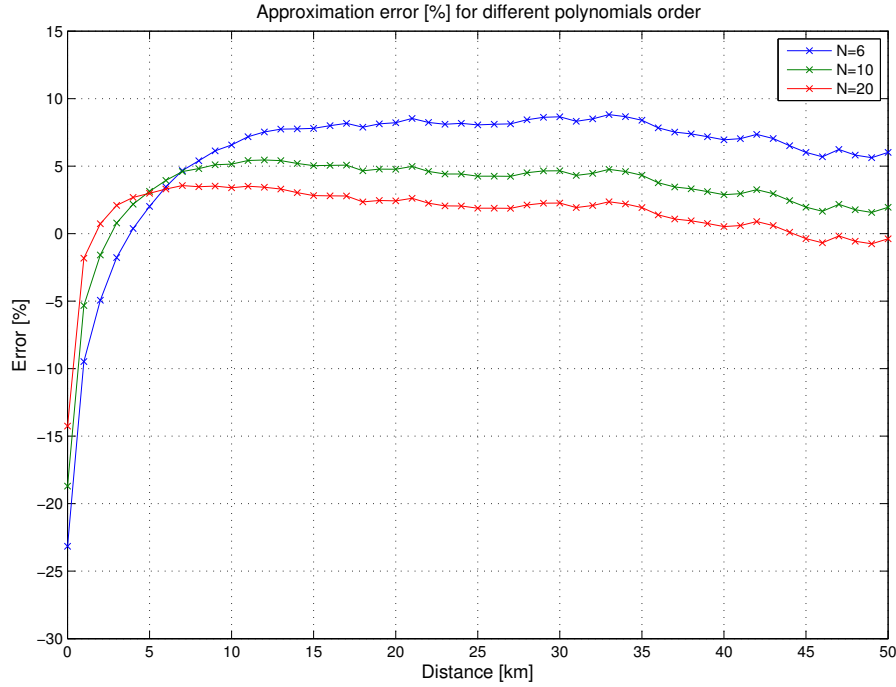


Figure A.6: Percentage error of convergence for different expansion order:
 $N = 6, 10, 20$

to obtain the result in Eq. A.22. This result provides an analytical result from the pre-filtering problem in this specific case. Fig. A.7 shows the pre-filtered correlation function as obtained by the Hermitian expansion equation. The error at values close to 1 of the expansion for limited order N appears also in the inversion, with correlation values greater than 1 which are clearly not possible. Apart from the initial values, the pre-filtered correlation follows well the reference analytical result, validating the proposed procedure.

The pre-filtered correlation for the three different thresholds is shown in Fig. A.8, where it is clear the dependence between the correlation to be imposed as input and the threshold used for the non linear clipping.

Finally, Fig. A.9 shows the relationship between the desired correlation of the

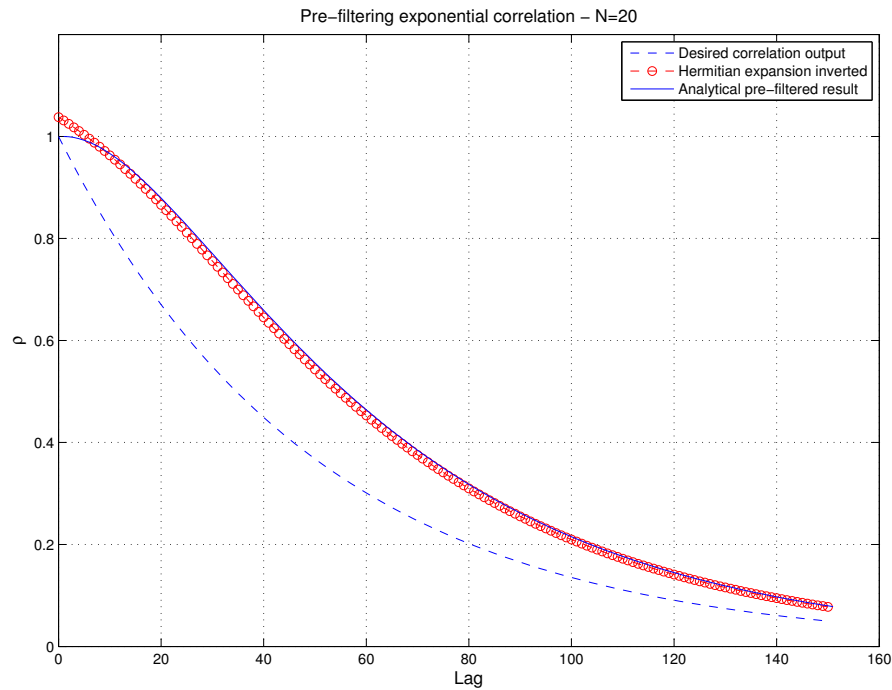


Figure A.7: Pre-filtering: solution obtained by inverting the Hermitian expansion of order $N = 20$ compared with analytical solution for the special case of $t_s = 0$

binary sequences and the one to impose at the random processes before the non-linear clipping. Again, it is evident the effect of the different clipping thresholds as well as the error introduced by the limited series expansion (input correlation greater than 1 when the desired correlation is close to unity).

The issue due to the limited series expansion can be solved by not considering the first few samples of correlation at the very small distances, as shown in the next section. A more complete solution would be to try to fit the pre-filtered curve avoiding the initial distances and forcing the fit to be 1 at $d = 0$. The fitting possibility by a simple function is under consideration at the time of this report and is left as a future development.

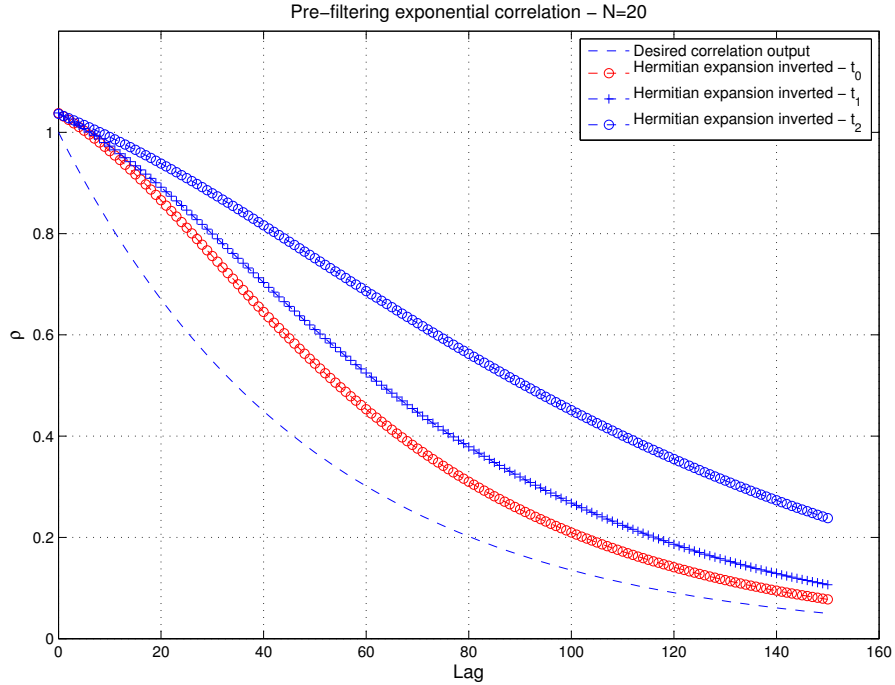


Figure A.8: Pre-filtering: solution obtained by inverting the Hermitian expansion of order $N = 20$ for different clipping thresholds

A.6 Application to the rain model problem - Pre-filtering example

Referring to the rain model described in Sec. A.1, the aim is to generate a set of binary sequences (one for each station in the area) which exhibit the desired spatial correlation of rain. Given N stations in the area, we generate N Gaussian random processes (zero mean and unit variance). The “rain event” condition is imposed when the random variable exceed a defined threshold $t_{s,i}$ dependent on the rain probability of the station i (see Sec. A.1).

Referring to the description above and Fig. A.1, the desired correlation among the binary sequences is not the one to be imposed to the input random processes before

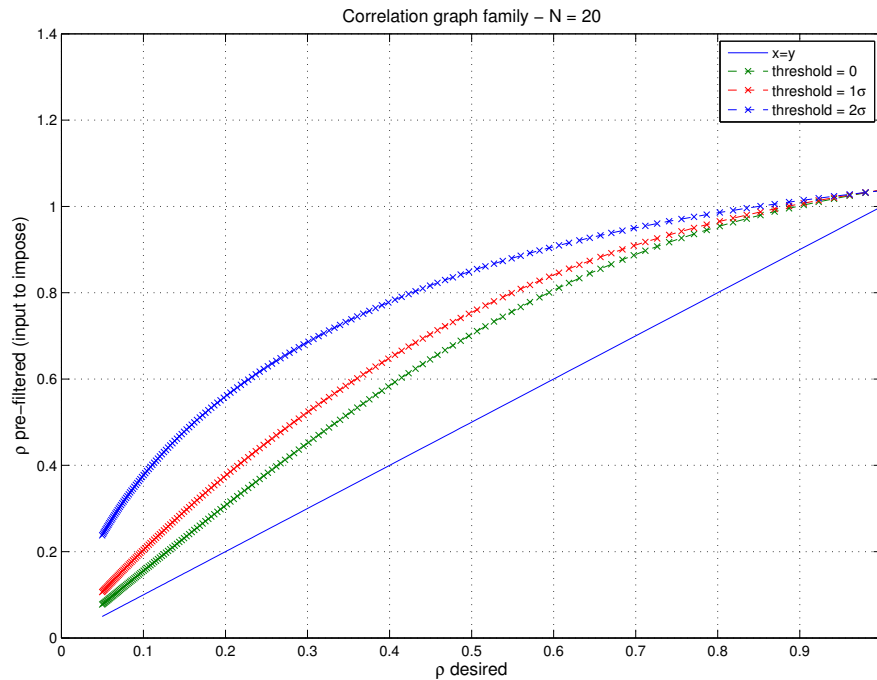


Figure A.9: Relationship between the desired correlation to be shown by the output binary sequences and the required correlation to be imposed to the input Gaussian random processes

clipping. Here the input spatial correlation is derived by inverting the series expansion which takes into account the effect of the clipping. Firstly, the series expansion of the desired correlation is evaluated by means of the Hermitian polynomials. The input correlation value is simply the only positive root of the polynomial obtained by the expansion. Fig.A.10 shows the result obtained for the same test case in Fig. A.1.

In order to obtain the desired correlation (blue dash) of the binary sequences after the clipping process, we derived the correlation to be imposed to the Gaussian random processes at input (red - dotted). Because of the limited number of terms in the Hermitian expansion, the start of the curve is not well resolved and the correlation values are greater than unity for the first distances. Since it is known that correlation at lag 0 is equal to 1, the inversion can be performed not considering the first distance

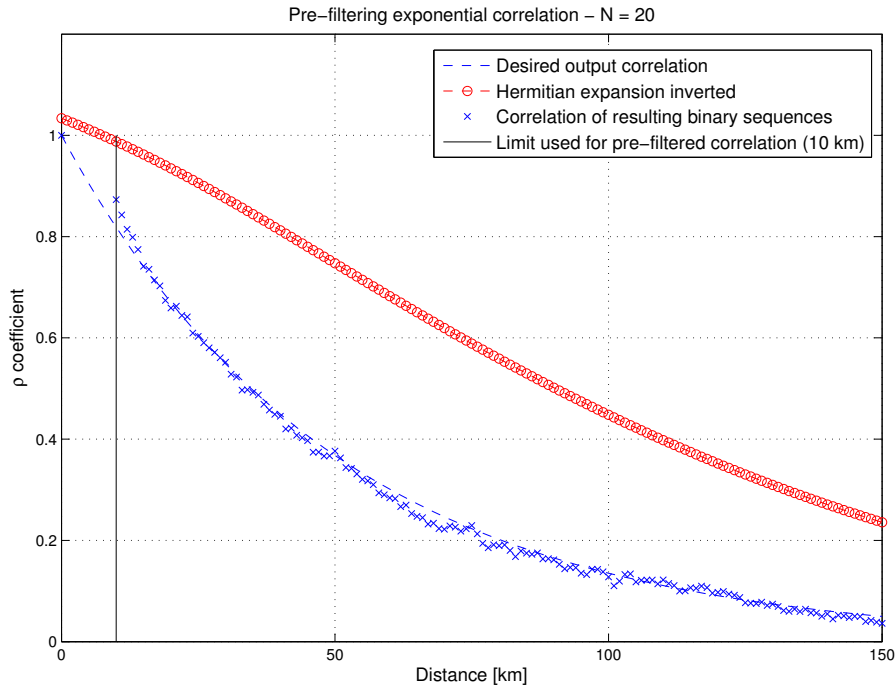


Figure A.10: Test case of rain model: resulting output correlation of binary sequences after hard thresholding

values (in the case considered $D_{min} = 10$ km). In the figure, blue crosses show the correlation of binary sequences generated after the clipping process: the correlation values corresponding to the red dots were imposed to the input random processes to obtain the correct correlation after clipping. Note that the accuracy of the solution is very high even for a single realization.

A.7 Other Interesting Applications

This work could be useful when it is required to work with many variables whose state can be modelled as a binary sequence. Particularly interesting are applications in Biology, when many cases of study need to model the presence or absence of a specific condition. In those cases, being able to impose a desired correlation among

the test variables is important [81].

More related to the field of communications the study of Cognitive Radio Systems [82]. Wireless communications are subject to signal fading and interference due to propagation conditions and the presence of other users in the same area. A binary variable related to each user can state the level of interference or fading by which the user is affected. As an example of this research field, in [83] the case of Interference-aware power allocation in Cognitive Radio Networks is addressed.

According to the authors, the mathematical framework of the proposed model can be of interest for other physical studies. In biology, the activation of ion channel gating is characterized by the correlation dynamic of the channels [84, 85]; furthermore, in wind power generation the spatial correlation among the active wind sites represents a significant aspect in modelling partially dependent wind farms [86].

A.8 Conclusions

In this work the author developed the analysis of the correlation characteristics of random processes subject to an hard-thresholding. This problem has to be tackled because of the need of generating binary sequences with a desired correlation function, starting from random noise sequences.

Referring to the theory of noise clipping, a general expression for the correlation after a clipping process (non-linear transformation) was found. The expression, derived for very general transformations, must be adapted to match the binary transformation of interest. Particularly, the need of a clipping threshold different from zero imposed to find a suitable way to solve the integral of a Gaussian kernel. The problem tackled was to derive the effect of the non linear transformation in such a way

to properly invert it, in order to derive the necessary correlation before the clipping given the desired output correlation function.

The solution to this problem was found in a series expansion of the value of the integral by means of a suitable set of orthogonal polynomials. The accuracy of the result was assessed both for different clipping thresholds and the order of the series expansion. The series expansion allowed to derive the correct correlation of the input random sequences to obtain a desired correlation function after the clipping. Knowing the desired correlation, the input one is derived by a “pre-filtering” operation. Finally, this procedure was tested for an example case related to a model to generate correlated series of rain attenuation with accurate final results.

Curriculum Vitae

Name: Marco Luccini

Education: B.Eng. 2004
Politecnico di Milano
Milano, Italy

M.E.Sc. 2008
Western University
London, Ontario, Canada

Ph.D., Engineering Sc. 2013
Western University
London, Ontario, Canada

Publications

Refereed Journal Papers:

- [1] Riva C., Capsoni C., Luini L., LUCCINI M., Nebuloni R., Martellucci A., “The challenge of using the W band in satellite communication”, *International Journal of Satellite Communications and Networking*, 2013;
- [2] Capsoni C., Castanet L., Gabellini P., Martellucci A., Carrie G., Gallinaro G., Gatti N., Jeannin N., LUCCINI M., Luini L., Nebuloni R., Paraboni A., Resteghini L., Riva C., “Rain Field Generators Implemented in a European Broadcasting Satellite System Using a Reconfigurable Satellite Antenna”, *Space Communications Journal*, 2012;
- [3] Capsoni C., LUCCINI M., Gabellini P., Martellucci A., Nebuloni R., Resteghini L., Riva C., “Presentation of the Analysis Tool for Design of Onboard Reconfigurable Antenna for Broadband Satcom and Broadcast Services”, *Space Communications Journal*, 2012;

Submitted Journal Papers:

- [1] LUCCINI M., Primak S., Capsoni C., “Generating Correlated Time Series of Rain Attenuation for Multiple Satellite Receiving Stations from Real Acquired Data”, *IEEE Transactions on Antennas and Propagation Journal*, 2013.

Refereed Conference Proceedings:

- [1] Riva C., Capsoni C., Luini L., LUCCINI M., Nebuloni R., “W-band Atmospheric Radiowave Propagation A Challenge for Satellite TLC Systems”, *6th Advanced Satellite Multimedia Systems Conference and the 12th Signal Processing for Space Communications Workshop*, Baiona, Spain, 5-7 September 2012;
- [2] Nebuloni R., Resteghini L., LUCCINI M., Capsoni C., Riva C., Martellucci A., Gabellini P., “Presentation of the Analysis Tool for the Design of Onboard Reconfigurable Antenna for Broadband SatCom and Broadcast Services”, pp. 1- 6, *ESA Workshop on Radiowave Propagation 2011*, Noordwijk, The Netherlands, 30 November - 2 December 2011;
- [3] Capsoni C., LUCCINI M., Luini L., Matricciani E., Nebuloni R., Paraboni A., Resteghini L., Riva C., Castanet L., Carrie G., Jeannin N., Gabellini P., Gallinaro G., Gatti N., “Results and Conclusions on the Verification of Propagation Impairments Mitigation Techniques for SatCom Systems”, pp. 1- 17, *ESA Workshop on Radiowave Propagation 2011*, Noordwijk, The Netherlands, 30 November - 2 December 2011;
- [4] Paraboni A., Capsoni C., Resteghini L., Nebuloni R., LUCCINI M., “A Theoretical Approach for the Dynamic Reconfiguration of the On-board Antenna Pattern and its Performance Assessment”, *EUCap Conference*, Rome, Italy, 11-15 April 2011;
- [5] Capsoni C., Pierdicca N., Puiatti A., Corti G., LUCCINI M., Marzano F. S., Matricciani E., Mattioli V., Pulvirenti L., Riva C., Martellucci A., “Assessment of Propagation Effects in the W Frequency Band for Space Exploration: an ESA Study”, pp. 1- 7, *TTC 2010, 5th ESA International Workshop on Tracking, Telemetry and Command Systems for Space Applications*, ESA/ESTEC, Noordwijk, The Netherlands, 21-23 September 2010.

Masters Thesis:

-
- [1] M.Luccini, "Cross-Layer Optimization of Network Performance over MIMO Wireless Mobile Channel", *The University of Western Ontario*, 2008, supervised by Dr. A. Shami and S. Primak.

Awards and Scholarships

- [1] Politecnico di Milano, Double Ph.D. program grant, 2011, 2012
- [2] Western Engineering Graduate Entrance Scholarship, The University of Western Ontario, 2010-2013.
- [3] Award for Outstanding Presentation at the ECE Graduate Symposium, The University of Western Ontario, 2007.
- [4] Western Engineering Scholarship, The University of Western Ontario, 2006-2008.